Thèse de doctorat
Présentée et soutenue le : 08/12/2014
par
Aline Dellicour
pour obtenir le
Doctorat de l'Université de Caen Basse-Normandie
Spécialité : Chimie des Matériaux
et le
Grade de Docteur en Sciences de l'Université de Liège

Physical properties/texture relationship in industrial melt-cast processed Bi-2212 bulk superconductors using quantitative texture analysis

Directeur de thèse : Daniel Chateigner
Co-Directrice de thèse : Bénédicte Vertruyen

Composition du jury :

Luca Lutterotti	Professeur des Universités, Universita di Trento **(Rapporteur)**
Isabel Van Driessche	Professeur des Universités, Gent Universiteit **(Rapporteur)**
Philippe Vanderbemden	Professeur des Universités, Université de Liège
Mark Rikel	Senior scientist, Nexans SuperConductors GmbH
Daniel Chateigner	Professeur des Universités, Université de Caen **(Directeur de thèse)**
Bénédicte Vertruyen	Maître de Conférences, Université de Liège **(Directrice de thèse)**
Alain Pautrat	Chargé de Recherches, CRISMAT, CNRS, Caen (Invité)

Acknowledgements – Remerciements

I would like first to express my gratitude to the jury members who have accepted to judged this thesis. This work results from a partnership between the CRISMAT laboratory in Caen, the LCIS-GREENMAT laboratory in Liège and the Nexans Superconductors industry in Hurth. I would like to thank Antoine Maignan, Rudi Cloots, Bénédicte Vertruyen and Joachim Bock to accept me in their lab and industry and therefore provided me the opportunity to accomplish my thesis.

My greatest acknowledgements go to my two thesis directors, Bénédicte Vertruyen and Daniel Chateigner and our industrial partner Mark Rikel. Mark has contributed a lot in this work and showed a large interest in understanding the relationship between physical properties and texture. He brought in this work a valuable knowledge about superconductors. Thanks Mark for all the discussions we had from which I learned a lot and that helped to move forward in the thesis.

Je remercie Daniel pour tout le temps qu'il a consacré à m'initier au domaine de la texture et à décortiquer les figures de pôles. Son expérience dans le monde de la texture et ses conseils avisés ont été un des moteurs de mon travail de recherche. Quant à Bénédicte, j'ai énormément appris de sa rigueur scientifique, de sa curiosité à vouloir aller au fond des choses et des conseils éclairés qu'elle m'a fournis du début à la fin de la thèse. Merci à tous les deux pour votre disponibilité, votre soutient et votre collaboration durant ces trois ans.

Ce travail n'aurait pas vu le jour sans la participation financière du ministère français de l'enseignement supérieur et de la recherche, et celle de l'Université de Liège.

Cette thèse est également le fruit d'une collaboration avec de nombreux chercheurs et techniciens de différents laboratoires et de différents domaines : Olivier Perez, Alain Pautrat, Sylvie Hebert, Luca Lutterotti, Philippe Vanderbemden, Fabien Veillon, Stéphanie Gascoin, et Jérôme Lecourt.

Je remercie l'Institut Laue-Langevin pour m'avoir permis d'effectuer des me-

sures de diffraction des neutrons et tout particulièrement Bachir Ouladdiaf pour m'avoir supervisée lors des deux sessions de mesure sur les lignes D19 et D1B.

Avant de passer à des remerciements plus personnels, je souhaite adresser mes sincères remerciements à toutes les personnes qui, de près ou de loin, ont contribué à la réalisation de cette thèse et ont permis par leur soutient et leurs conseils, de la mener à terme. I would also like to thank all IDS FunMAT students for the great times spent in Anglet, Annecy, and Spa.

Je remercie tous les membres du laboratoire LCIS-GREENMAT pour les bons moments passés au labo. Et plus particulièrement à mes anciens collègues de bureau Audrey, Claire, Jonathan, et Julien.

Il m'importe de remercier également les chimistes de mon année pour les 5 ans passés ensemble, pour tous les bons moments que nous avons passés en classe, en labo ou à l'extérieur. Je retiens en particulier le paint ball, Durbuy et le souper chimie où grâce à l'équipe soudée que nous formions, tout s'est passé comme sur des roulettes. Bien sur, ces 5 ans n'auraient pas été les mêmes sans la présence de Pierre-Hugues, Benjamin, Paul, Whitney et Jonathan au sein de cette classe. Que de souvenirs construits avec vous durant les études, la thèse et je me réjoui des futurs qui viendront après la thèse.

Ces presque 2 ans en immersion en France furent une belle aventure par le biais de laquelle j'ai rencontré de formidables personnes. J'ai appris beaucoup d'un point de vue scientifique mais encore plus d'un point de vue humain. Comme l'a dit Dany Boon dans Bienvenue chez les Ch'tis, "Quand un étranger déménage dans le nord (quoique, le Sud pour moi), y braille deux fois : une fois quand il arrive et une fois quand il part". Il est sans aucun doute que j'aurai la larme à l'œil en quittant Caen. Et bien que nous soyons voisins, il m'a quand même fallu assimiler pas mal de choses : l'expression "c'est balot", les nombreuses abréviations, ce qu'est un critérium, qu'on risque sa vie à chaque passage pour piétons, qu'en France, on ne connait pas l'orangeade, la farde, le payement par bancontact et j'en passe.

Je garderai un souvenir immuable des nombreux temps de midi, mots fléchés, pauses café, Béabar,... passés avec Hélène, Marion, Flora, Sara, Victor, Adrian, Fabien, Aurélie, les Morgane, Gwladys, Charlène, Mélanie, Nicolas, Olivier C et tout ceux qui s'y greffaient de temps à autre.

Je voudrais remercier en particulier :

- Hélène pour avoir été un modèle de rigueur, de détermination et de persévérance. Pour tous nos moments de complicité dans et hors du labo. Pour m'avoir cuisiné de bon petits plats, avoir été une oreille attentive et avoir toujours été de bon conseil. N'oublions pas non plus toutes les fois où tu as joué le taxi, même à 8h du matin sous la neige.
- Flora pour avoir été non seulement une collègue de bureau mais surtout une super amie. Merci pour toutes nos discussions autour d'un café dans le bureau ou autour d'une table de scrapbooking.
- Hélène, Olivier C, Marine, Romain et Marion pour m'avoir hébergée ponctuellement pendant ces trois ans lorsque j'étais de retour à Caen pour quelques jours ou désespérément à la recherche d'un appartement.

Je n'en serais certainement pas à écrire ces remerciements sans la présence de mes parents tout au long de ma vie d'étudiante puis de doctorante. Je ne vous remercierai jamais assez pour m'avoir soutenue tout au long de ces années et de m'avoir permis d'en arriver à la rédaction de cette thèse. Merci également à ma marraine, Philippe, Fanny et José sans qui je n'aurais pas découvert Bayeux, Arromanches, les plages du débarquement,... et surtout, le délicieux cidre de la ferme de Billy.

J'ai gardé le meilleur pour la fin, il me tient à cœur de remercier tout particulièrement Mike pour son soutien affectif sans faille. Merci de m'avoir encouragée, réconfortée et soutenue pendant ces trois ans et d'avoir écouté mes histoires pendant des heures à mes retours de Caen. Tu n'imagines pas combien ta disponibilité en personne ou par skype ainsi que tes nombreux aller-retours à Caen ont été précieux. Sans oublier que tu mérites une mention spéciale pour avoir été si bon aux Tetris géants qu'étaient chacun de mes déménagements.

Foreword

The research work reported in this PhD thesis dissertation was carried out during a 3-year project in the framework of the International Doctoral School in Functional Materials supported by the ERASMUS MUNDUS Programme of the European Union. All IDS Funmat PhD projects involve an industrial partner and at least two universities from the consortium.

Nexans Superconductors Gmbh, the industrial partner of this thesis, is active in the field of superconductors, i.e. materials that have the unique property of carrying high electric currents with almost no energy dissipation. Amongst the superconducting materials available to date, polycrystalline $Bi_2Sr_2CaCu_2O_8$ (Bi-2212) are routinely manufactured at Nexans Superconductors Gmbh as round wires for magnets and superconducting magnetic energy storage, or as bulk melt-cast processed samples of various shapes for fault current limiter devices that act as key protection components for power grids. The intriguing characteristic of these polycrystalline Bi-2212 materials is that they can carry extremely large currents although there does not seem to be any strong long range texture.

Therefore the objective of this thesis was to investigate in more detail the texture in Bi-2212 tubes and rods. The motivation was twofold : (i) on the one hand, a better understanding of the influence of the synthesis parameters on the microstructure, texture and superconducting properties could lead to a further improvement of the current carrying ability ; (ii) on the other hand, the characterization of texture in these materials is a challenge because of the composition and microstructure gradients that result from the synthesis procedure. Thanks to a combination of experiments by X-ray and neutron diffraction, electron microscopy and physical properties measurements, this thesis aims to be a contribution to both areas.

The dissertation is organized as follows :

The first chapter is a short introduction to the field of superconducting materials, with a focus on the bismuth cuprates and especially $Bi_2Sr_2CaCu_2O_8$. The second chapter introduces the concepts of crystallographic texture (such as pole figures or orientation distribution) and describes how texture can be determined from diffraction experiments.

In Chapter 3, a melt-cast processed Bi-2212 tube is used as a reference sample for the characterization of its texture by different instruments, including a 4-circle X-ray laboratory diffractometer and the two different neutron beam lines at Institut Laue Langevin. These texture results obtained on dedicated instruments are also compared to results obtained from a simpler approach implemented in a standard laboratory X-ray diffractometer.

Chapter 4 investigates whether texture and physical properties vary across the tube wall thickness or between different positions along the tube height and perimeter.

Chapter 5 concerns melt-cast processed rod-shaped samples with different diameters and oxygen contents. The first part of the chapter focuses on microstructure and texture. The second part characterizes the influence of the oxygen content on the electric and magnetic properties of 5mm-diameter rods.

Chapter 6 is a self-contained chapter where the experimental resistivity anisotropy ratio (reported for the tube sample in Chapter 3) is compared to a calculation based on the experimentally determined orientation distribution and literature data for the single crystal resistivity tensor.

The dissertation ends with general conclusions and discussion about possible future work.

The neutron diffraction data presented and discussed in Chapters 3 to 6 were collected at Institut Laue Langevin (Grenoble, France) in November 2011 (2 days on D19 beamline) and November 2012 (7 days on D1B beamline).

Contents

Abbreviations

Used variables

$\mathbf{h}$	h kl Direction perpendicular to the (hk$l$) set of planes
H	Magnetic field
H_c	Critical magnetic field
$H_{c,1}$	First Critical magnetic field
$H_{c,2}$	Second Critical magnetic field
hk$l$	hk$l$ crystallographic plane
J_c	Critical current density
M	Magnetization
ρ	Resistivity
R	Resistance
T	Temperature
T_c	Critical temperature
$\mathbf{y}$	The coordinates of the pole P are given as $\mathbf{y}=(\vartheta_y,\varphi_y)$

Abbreviations

Bi-2201	$Bi_2Sr_2CuO_{6+\delta}$	7
Bi-2212	$Bi_2Sr_2CaCu_2O_{8+\delta}$	7
Bi-2223	$Bi_2Sr_2Ca_2Cu_3O_{10+\delta}$	7
E-WIMV	Extended-Williams-Imhof-Matthies-Vinel	37
FWHM	Full Width at Half Maximum	40
GMA	Geometric Mean Average	123
GoF	Goodness of Fit	42
MAUD	Material Analysis Using Diffraction	52
MD	March Dollase	80
m.r.d.	Multiple of a Random Distribution	29
OD	Orientation Distribution	31
ODF	Orientation Distribution Function	31
PF	Pole Figure	28
PO	Preferred Orientation	77

CHAPTER 1 | *General introduction*

This first chapter gives an outline of the principal notions related to superconductivity and superconductors. The introduction to texture concepts is postponed to the next chapter. This chapter is divided in three sections and will first focus on the concept of superconductivity by giving an overview of the key parameters. The second section is dedicated to the $Bi_2Sr_2Ca_{n-1}Cu_nO_{2n+4}$ superconducting oxides with a focus on the $Bi_2Sr_2CaCu_2O_8$ compound. In this section, the crystallographic structure is described and the influence of synthesis parameters on the structure and the physical properties are detailed. The last section is devoted to the synthesis process and applications of the Nexans melt-cast processed bulk samples.

Chapter content

1.1 Theoretical concepts and definitions of superconductivity

This section aims to briefly review the discovery of superconductivity and superconducting materials. Some concepts of superconductivity are described in more detail for Type-II superconductors. Particularly, the magnetic behavior of Type-I and Type-II superconductors is compared. The last part of this section is dedicated to the definition of conditions for existence of a superconducting state with regard to temperature, magnetic field and current density.

1.1.1 Critical temperature: the quest for higher values

The Dutch physicist H. Kamerling Onnes [1] was the first to measure the electrical resistance of metals at temperatures close to absolute zero. In 1911, he discovered that the electrical resistance of mercury vanishes below a temperature of 4.2K. He thereby discovered superconductivity, i.e., a state of matter in which resistivity drops to an undetectable value below a temperature called the critical temperature (T_c). Many metals exhibit a superconducting state when cooled down to low temperatures. Indium (T_c=3.4K), tin (T_c=3.7K), tantalum (T_c=4.5K), lead (T_c=7.2K) or niobium (T_c=9.3K) are examples of metallic superconductors. Niobium is the pure element with the highest critical temperature, leading to much research on Nb-alloys. Such Nb alloys as NbTi (maximum T_c=9K) and Nb-Zr (maximum T_c=11K) and compound Nb_3Sn (maximum T_c=18.3K) become practical superconductors and are widely used in the fabrication of magnets for the production of large magnetic inductions required for nuclear magnetic resonance, particle accelerators or mass spectrometry. To reach a temperature below T_c these magnets are cooled down with liquid helium. The highest T_c reached in the metallic alloys and compounds is 23K observed in Nb_3Ge thin films. As shown in Figure 1.1 1986 saw a further increase in T_c with the discovery by Bednorz and M*ü*ller [2] of the first high temperature superconductor, the $Sr_{0.2}La_{1.8}CuO_4$ cuprate with a T_c of 36K. Other cuprates have been discovered since then, the best-known of them being $YBa_2Cu_3O_7$ [3], $Bi_2Sr_2CaCu_2O_8$ [4], and $Bi_2Sr_2Ca_2Cu_3O_{10}$ [5] with T_c's of respectively 92K, 85K, and 110K. These compounds have T_c's above the boiling temperature of liquid nitrogen (77K). At present, the highest T_c is 134K for the compound $HgBa_2Ca_2Cu_3O_8$ [6]. Superconductivity has also been discovered in other classes of compounds: iron pnictides such as $La(O_{0.89}F_{0.11})FeAs$ (T_c=26K) [7], MgB_2 (T_c=39K) [8] or organic superconductors such as fullerenes like Rb_3C_{60} (T_c=30.7K) or Cs_2RbC_{60} (T_c=33K) [9].

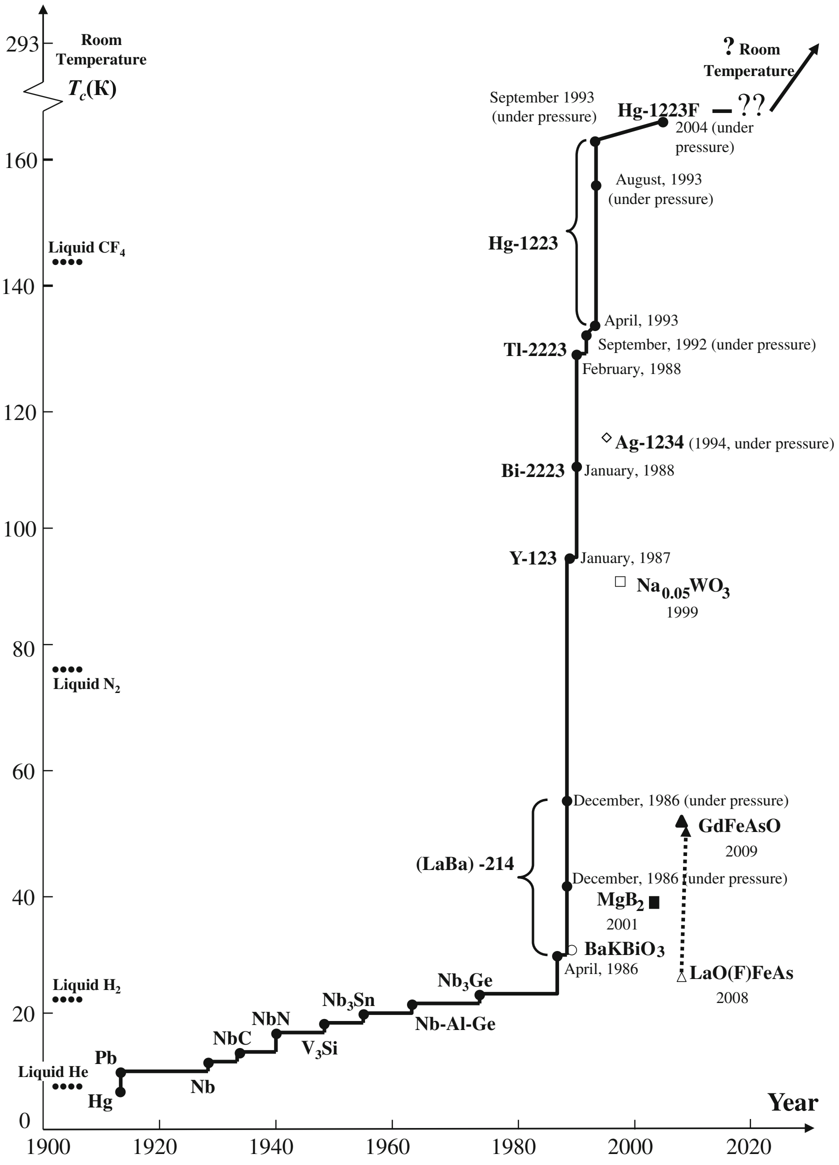

Figure 1.1 – Critical temperature of superconductors versus year of discovery [10].

1.1.2 Critical magnetic field(s)

In 1933 Meissner and Ochsenfeld [11] found that below T_c, a superconductor placed in a weak external magnetic field (H) expels the magnetic field. The superconducting currents at the surface of the superconductor oppose the penetration of the magnetic field, so that the magnetic induction (B) created in the superconductor when it is exposed to an external magnetic field is equal to 0. Above the critical magnetic field H_c, the superconductor transits to the normal state. It was later shown by Shubnikov [12] that superconductivity ceases to exist according to two different scenarios and depending on their magnetic behavior superconductors are classified as type-I or type-II superconductors. Theoretical explanation for such classification was given in 1957 by Abrikosov [13].

The behavior of magnetization versus applied magnetic field is shown in Figure 1.2 for both type-I and type-II superconductors. Below T_c, a type-I superconductor expels entirely the magnetic field until $H=H_c$ where the magnetization suddenly drops to 0. Below H_c, the superconductor is in a perfect diamagnetic state called the Meissner state. More accurately, the magnetic field penetrates only over a short length known as the London penetration depth λ [14], which constitutes the first characteristic length of superconductors. Type-I superconductors are metallic elements like Al, Sn, Pb, or Nb. All other superconductors are classified as type-II superconductors. In type-II superconductors magnetization (in absolute value) is maximum at $H=H_{c,1}$ and then decreases until reaching 0 at a second critical field $H_{c,2}$. Above $H_{c,2}$ the material is in its normal state. $H_{c,1}$ and $H_{c,2}$ are called lower and upper critical magnetic field. The magnetic field-temperature phase diagram of a type-II superconductor, shown in Figure 1.3, can be divided in three regions:

1. Meissner state: perfect diamagnetic state present below $H_{c,1}$.
2. Mixed state (Shubnikov phase): partial diamagnetic state present between $H_{c,1}$ and $H_{c,2}$. Above $H=H_{c,1}$, the magnetic flux starts to penetrate in the superconductor in the form of vortices.
3. Normal state: Non-superconducting state appearing above $H_{c,2}$.

Beyond $H_{c,1}$, the magnetic field penetrates in the superconductor from the surface as magnetic flux lines called vortices characterized by a normal core. Each vortex carries a quantum of magnetic flux Φ_0=2.07 10^{-15}Wb. Vortices can been described as normal cores of diameter 2ξ surrounded by superconducting currents decaying exponentially over the characteristic length λ, the London penetration depth. ξ is called the coherence length and constitutes the second characteristic length of superconductors. [15] When the vortices enter in the superconductor, they interact with microscopic defects (impurities, crystal defects, second phases), which act as pinning centers so that vortices cannot move freely in the superconductor. Ideally pinning centers should be approximately of the size of the coherence length. Vortices are pinned until the irreversibility field H_{irr} is reached. Above H_{irr}, pinning becomes ineffective, vortices are free to move and this vortex motion produces energy dissipation. The irreversibility line is shown in the H-T phase diagram in Figure 1.3. The number of vortices increases with the applied magnetic field while the distance between the normal cores decreases. $H_{c,2}$ is reached when the normal cores start to overlap.

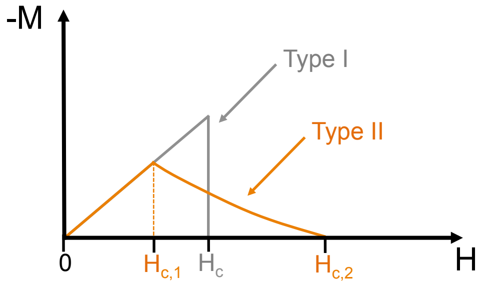

Figure 1.2 – Evolution of magnetization (M) with applied magnetic field (H) for a type-I and a type-II superconductor.

Ginzburg and Landau defined a constant $\kappa = \lambda/\xi$ named the Ginzburg and Landau parameter. Type-I superconductors are characterized by $\kappa < 1/\sqrt{2}$ while type-II superconductors have $\kappa > 1/\sqrt{2}$. [16] Some values of λ, ξ, and κ are listed in Table 1 for both type-I and type-II superconductors. In some highly anisotropic type-II superconductors, λ and ξ take different values for the different crystallographic axes. The influence of the anisotropy of the crystalline structure on the physical properties will be discussed in Section 1.2.1.2.

Superconductor Type	**Compound**	λ **(nm)**	ξ **(nm)**	$\kappa = \lambda/\xi$
I	Sn	34	230	0.15
	Pb	37	83	0.44
	N b	39	38	1.1
II	Nb3Sn	65	3.6	18
	PbBi	200	10	20
	$(Ba_{0.1}La_{0.9})_2CuO_{4-\delta}$	77	6.7	11.5

Table 1.1 – Penetration depth (λ), coherence length (ξ), and Ginzburg-Landau parameters (κ) for different type-I and type-II superconductors [17].

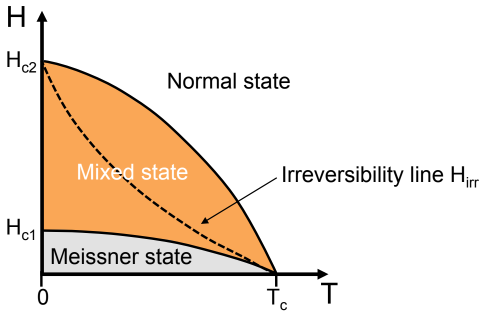

Figure 1.3 – Field-Temperature phase diagram of a type-II superconductor.

1.1.3 Critical current density

In addition to the critical temperature T_c and the critical magnetic fields H_c, H_c1, H_c2, and H_{irr}, the existence of the superconducting state depends also on the critical current density (J_c). The critical current density J_c is defined as the value of current density at which vortices start to move freely in the superconductor. The surface in the (T, H, J) space as represented in Figure 1.4 depicts the region useful for power applications. For current densities higher than the critical one J_c, the superconductor enters in a dissipative state but superconductivity is not lost. The suppression of J_c at H_{irr} means that H_{irr} and not $H_{c,2}$ is the limiting field for applications. The shape of the critical surface can be affected by mechanical strains or deformations. Moreover, in case of highly anisotropic superconductors, the critical surface depends on the crystallographic axes of the superconductor as well for the critical current density as for the critical magnetic field. The effect of anisotropy will be discussed in particular for $Bi_2Sr_2CaCu_2O_8$ in Section 1.2.1.2.

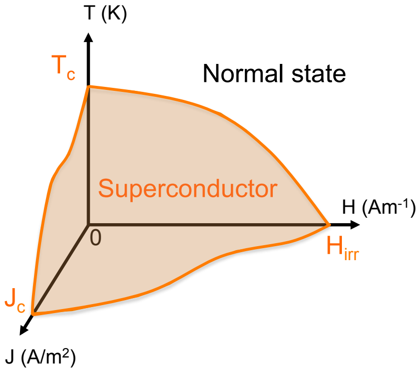

Figure 1.4 – Critical surface of a superconductor that separates superconducting state from normal state as a function of temperature (T), magnetic field (H), and current density (J) with their critical values T_c, H_c, J_c.

1.2 $Bi_2Sr_2Ca_{n-1}Cu_nO_{2n+4}$ superconducting oxides

Bismuth-based superconducting cuprates adopt the generic formula $Bi_2Sr_2Ca_{n-1}Cu_n O_{2n+4+\delta}$ or BSCCO [18,19]. The three main superconducting compounds of the series (n=1, 2, 3) are $Bi_2Sr_2CuO_6$ (abbreviated using the stoichiometric coefficients as Bi-2201; $T_c < 20K$) [20], $Bi_2Sr_2CaCu_2O_8$ (Bi-2212; $T_c = 85K$) [4], and $Bi_2Sr_2Ca_2Cu_3O_{10}$ (Bi-2223; T_c = 110 K) [5]. Bi-2212 and Bi-2223 have attracted most attention because they have T_c's above liquid nitrogen temperature (77K).

This section stars by a description of the crystallographic structure of the BSCCO superconducting cuprates. Some particular phenomena (modulations, anisotropy, intergrowths) taking place in the Bi-2212 compound are then presented briefly. This section ends with a description of the effect of the synthesis parameters on the crystallographic structure and physical properties.

1.2.1 Crystallographic structure

The crystallographic structures of the n=1, n=2 and n=3 compounds are represented in Figure 1.5. The three phases have a layered structure that differs in the stacking sequence along the crystallographic axis *c*. [BiO] bilayers of rock-salt type alternate with [Sr-Ca-Cu-O] blocks of perovskite type [18,21–23]. The n=1,2,3 compounds differ by the structure of the perovskite [Sr-Ca-Cu-O] block : n CuO_2 planes are separated by layers of Ca and sandwiched between SrO layers. The sequence along the c axis parameter can be summarized as follows:
Bi-2201: -[BiO]-[SrO]-[CuO_2]-[SrO]-[BiO]-
Bi-2212: -[BiO]-[SrO]-[CuO_2]-[Ca]-[CuO_2]-[SrO]-[BiO]-
Bi-2223: -[BiO]-[SrO]-[CuO_2]-[Ca]-[CuO_2]-[Ca]-[CuO_2]-[SrO]-[BiO]-
CuO_2 planes play an important role in the structure because they contain the strongest bonds of the structure (i.e. Cu-O bonds) fixing the lattice constants in the *ab*-plane. Other planes are forced to match with the fixed lattice constants. [19] For the three structures, the a- and b- cell parameters are approximately 5.4Å. The increasing number of planes along the c direction from Bi-2201 to Bi-2223 has the effect to increase the cell parameter c. The average c crystallographic axes are 24.6Å, 30.7Åand 37.1Åfor Bi-2201, Bi-2212, and Bi-2223 respectively. The principal characteristics of the three phases are summarized in Table 1.2.

Compound	**Abbreviation**	**First synthesis**	**a [Å]**	**b [Å]**	**c [Å]**	**CuO_2 planes**	**T_c [1]**
$Bi_2Sr_2CuO_6$	Bi-2201	1987 [20]	5.4	5.4	24.6 [24]	1	20K
$Bi_2Sr_2CaCu_2O_8$	Bi-2212	1988 [4]	5.4	5.4	30.7 [21]	2	85K
$Bi_2Sr_2Ca_2Cu_3O_{10}$	Bi-2223	1988 [5]	5.4	5.4	37.1 [25]	3	110K

Table 1.2 – Comparison of the three main compounds of the BSCCO family.

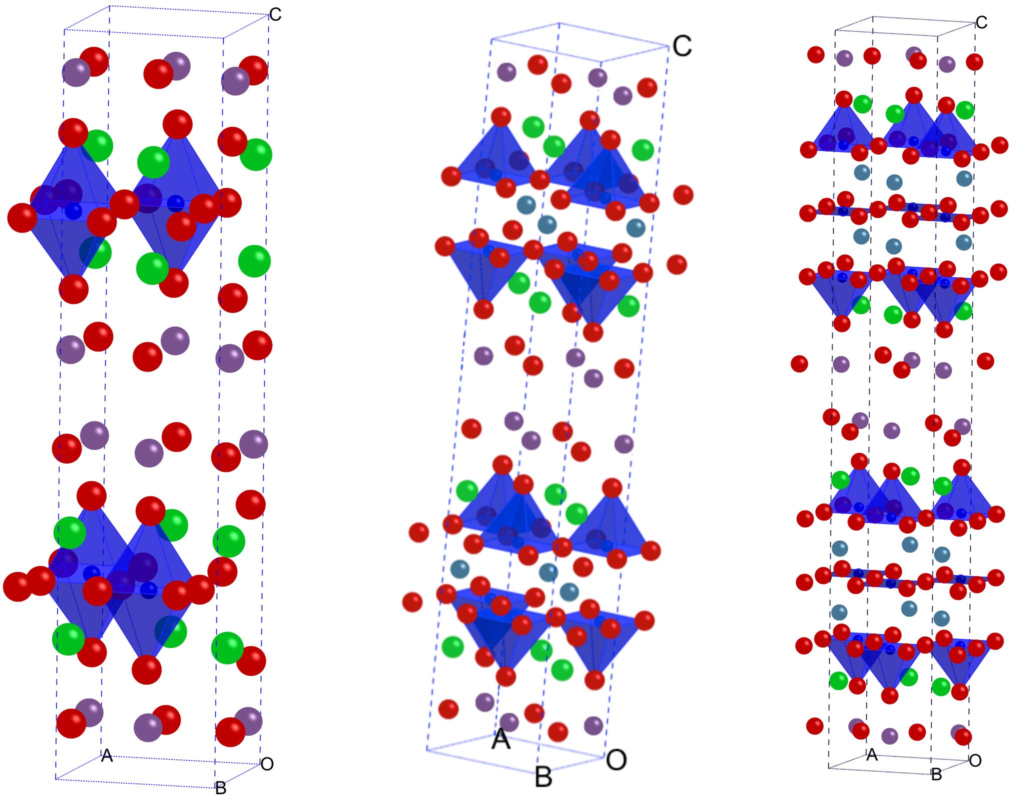

(a) $Bi_2Sr_2CuO_6$ (Bi-2201)

(b) $Bi_2Sr_2CaCu_2O_8$ (Bi-2212)

(c) $Bi_2Sr_2Ca_2Cu_3O_{10}$ (Bi2223)

Figure 1.5 – Representation of crystallographic structures of Bi-2201, Bi-2212 and Bi-2223

---

[1] Characteristic values measured in single crystals

1.2.1.1 Modulations

In the context of this thesis, Bi-2212 is the phase of main interest and is discussed in more detail. In some papers (See Table 1.3), the average structure of Bi-2212 is given in a pseudo-tetragonal symmetry with lattice parameters a=b=5.4 Å and c=30.7 Å [5, 21, 26–28]. Real structures are more complex to establish due to displacive and substitutional modulations. [29] Since the discovery of Bi-2212 compounds much research has been devoted to the study of modulated Bi-2212 structures using electron, x-ray, and neutron diffraction techniques. [4, 30–37] Early models for the origin of modulation in Bi-2212 have been proposed based on displacive or substitutional modulations. In other words, modulation may be due to site exchange of cations or mismatch between the Bi-O layer and the perovskite layer [34–38]. Another model suggested the insertion of an additional oxygen atom in the structure [22, 29, 30, 33, 39, 40]. Modulation is observed in electron diffraction patterns by satellite reflections displaced from the main reflections by $\vec{q}$. If the reference frame of the reciprocal lattice is defined by the vectors $\vec{a}^*$, $\vec{b}^*$, and $\vec{c}^*$, the reciprocal lattice vector in a modulated structure is written as: $\vec{H} = h\vec{a}^* + k\vec{b}^* + l\vec{c}^* + m\vec{q}$ where $\vec{q}$ is the wave vector characterizing the modulation. A commensurate modulation corresponds to a vector $\vec{q}$ having only rational components. An incommensurate modulation corresponds to a vector $\vec{q}$ having at least one irrational component. In case of an incommensurate modulation, the structure cannot be described by a unit cell composed of a multiple number of basic unit cell.

In Bi-2212 structures, several authors reported a one-dimensional incommensurate modulation with the vector $\vec{q} = 0.21\vec{b}^* + \vec{c}^*$. Substitutions can cause a variation of the modulation vector [41]. For example, modulations can disappear in the Bi-2212 structure by atomic substitution of Bi^{3+} by Pb^{2+} [42]. The substitution of trivalent Bi(III) by divalent Pb(II) causes a decrease in oxygen content in the Bi-O layer. This decrease of oxygen content yields a longer periodicity of modulation and a shorter *b*-axis. If the Pb content is large enough, there are no longer additional oxygen atoms in the structure, leading to the disappearance of the modulation.

Author (year) and reference	System	Space group	Lattice parameters		
			a [Å]	b [Å]	c [Å]
Bordet (1988) [43]	Pseudo-tetragonal	Fmmm	5.401	5.401	30.83
Bordet (1988) [44]	Orthorhombic	A2aa	5.4095	5.4202	30.9297
Subramanian (1988) [45]	Orthorhombic	Amaa	5.399	5.414	30.904
Hervieu (1988) [46]	Orthorhombic	Amaa	5.4054	5.4016	30.7152
Tarascon (1988) [5]	Tetragonal	I4/mmm	3.814	3.814	30.52
Sunshine (1988) [47]	Orthorhombic	Fmmm	5.414	5.418	30.89
Gao (1988) [32]	Orthorhombic	Amaa	5.408	5.413	30.871
Petricek (1990) [33]	Orthorhombic	A2aa	5.408	5.413	30.871
Yamamoto (1990) [30]	Orthorhombic	Bbmb	5.3957	5.3971	30.649
Beskrovnyi (1990) [48]	Orthorhombic	Amaa	5.397	5.401	30.716
Kan (1992) [35]	Orthorhombic	Bb2b	5.415	5.421	30.88
Bhargava (1992) [49]	Orthorhombic	Amaa	5.365	5.424	30.74
Novomlinsky (1993) [50]	Orthorhombic	Bbmb	5.407	5.410	30.762

Table 1.3 – List of system, space group and lattice parameters for $Bi_2Sr_2CaCu_2O_8$.

1.2.1.2 Anisotropy

Due to the layered structure of Bi-2212 with CuO_2 planes in the *ab* planes, Bi-2212 exhibits a large anisotropy of physical properties between directions in the ab plane ("in-plane") and the c direction ("out-of-plane"). For example, Figure 1.6 shows the temperature dependence of in-plane and out-of-plane resistivities measured in Bi-2212 single crystals by Watanabe et al. [51]. This study reveals a difference of several orders of magnitude between the in-plane and out-of-plane resistivities in the normal state. Figure 1.7 shows that J_c in single crystals is also anisotropic. At low temperature and low field values, J_c(ab) and J_c(c) are of the same magnitude. J_c(c) tends to decrease rapidly with temperature and field increase while J_c(ab) is weakly influenced by the magnetic field (in the range of field represented in the figure) under a temperature of 40K. Above this temperature, J_c(ab) also tends to decrease with field and temperature increase. Table 1.1 shows that the London penetration depth and coherence length also depend on orientation in the crystal.

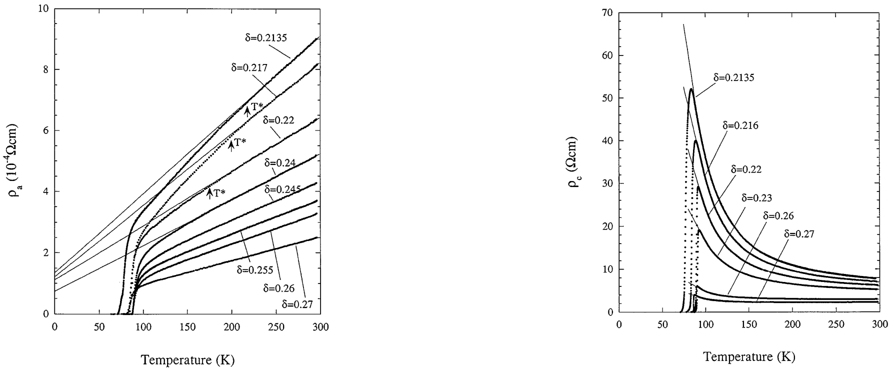

(a) ρ_{ab} vs. T

(b) ρ_c vs. T

Figure 1.6 – Temperature dependence of resistivities for Bi-2212 single crystals at different oxygen stoichiometry (8+δ) for (a) in-plane resistivity (ρ_{ab}) and (b) out-of-plane resistivity (ρ_c) [51].

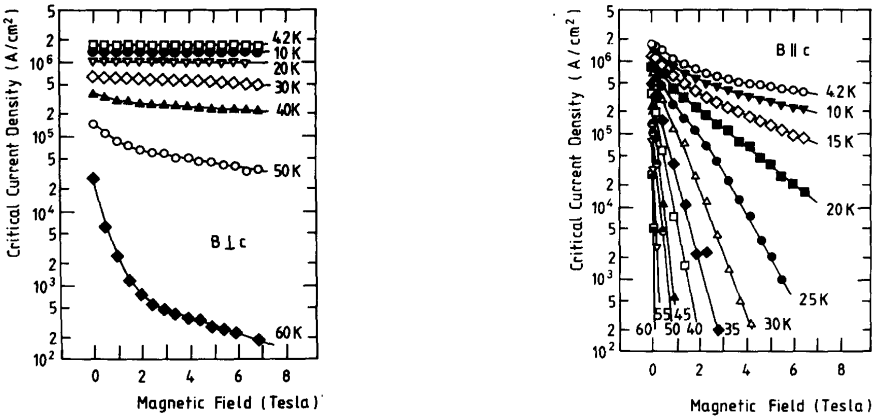

(a)J_c(ab) vs. B

(b)J_c(c) vs. B

Figure 1.7 – Magnetic field dependence of the critical current density for a Bi-2212 thin film with the field applied (a) ⊥ c and (b) // c at different temperatures [52].

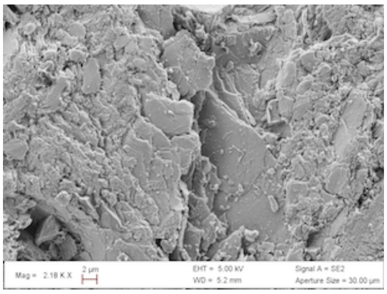

Figure 1.8 – SEM micrograph of a Bi-2212 bulk sample showing the Bi-2212 platelet grains

1.2.1.3 Intergrowths

Rikel et al. [53] studied the development of Bi-2201 intergrowths in the Bi-2212 phase during the melt-process of Ag-sheated Bi-2212 tapes. They evidenced using EDX a phase with a composition of Bi:Sr:Ca:Cu=4:4-x:1+x:3 corresponding to Bi-2212+Bi-2201. These intergrowths arise from an incomplete consumption of second phase particles during the cooling of the samples and are very stable. An X-ray diffraction study of these tapes showed a change in peak shape or the appearance of new diffraction peaks caused by the presence of Bi-2201 intergrowths in the Bi-2212 structure.

1.2.2 Influence of the oxygen stoichiometry on crystalline structure and properties

Schweizer et al. [54] studied the oxygen stoichiometry (δ) in Bi-2212 pellets as a function of temperature and oxygen partial pressure during the heat treatment. Their diagram, presented in Figure 1.15, shows that the oxygen content in the Bi-2212 phase tends to decrease when the oxygen partial pressure is decreased and/or the temperature is increased. The oxygen stoichiometry affects both the crystalline structure and the physical properties of Bi-2212 materials.

Figure 1.9 shows the results of a study of Sun et al. [55] on the variation of cell parameters with oxygen pressure during annealing of Bi-2212 samples. a and b are only slightly influenced by oxygenation [55–57], with a decrease of about 0.01Å when going from a pressure of 10^{-8} to 10^4 Torr. The c parameter is much more influenced by oxygenation and decreases by 0.1Å when going from a pressure of 10^{-8} to 10^4 Torr [55–57]. It has been proposed that the oxygen stoichiometry affects the Bi_2O_2 bilayers, constituted of a stacking of two BiO planes. [58] Bi^{3+} cations of electronic configuration $[Xe]5d^{10}6s^2$ have an electronic lone pair [22] located between the two BiO layers. Oxygen diffusion between these two BiO layers is supposed to induce a variation of orientation of this lone pair, resulting in a contraction of the two layers and a decrease of cell parameter c.

Bi-2212 samples have a critical temperature around 85K. Several studies [55, 59, 60] showed that the value of T_c is directly linked to the oxygen stoichiometry in the Bi-2212 phase. Figure 1.10 shows the oxygen stoichiometry dependence of critical temperature for Bi-2212 samples. The curve has a bell shape with a maximum T_c observed for an oxygen stoichiometry of 8.2. This confirms that controlling the synthesis parameters is necessary to reach maximum T_c.

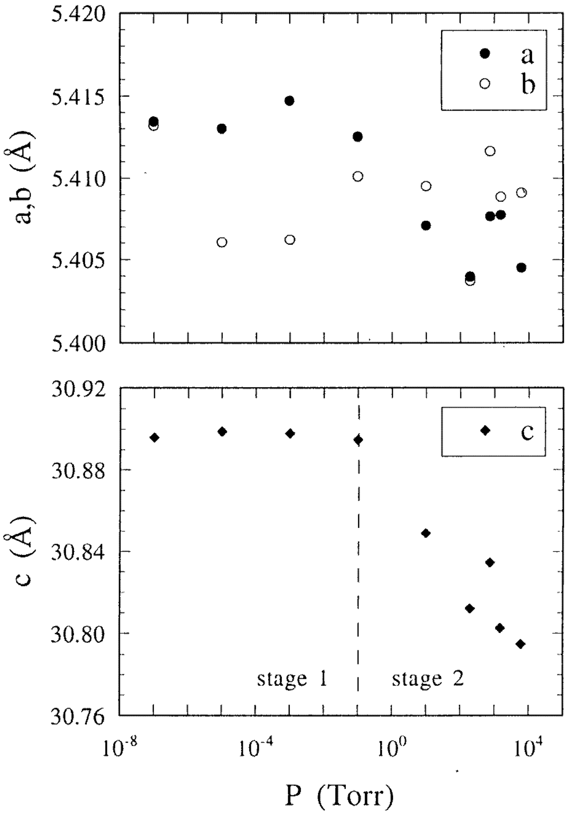

Figure 1.9 – The dependence of lattice parameters on the oxygen pressure P of annealing at 600°C for $Bi_2Sr_2CaCu_2O_y$ single crystals [55].

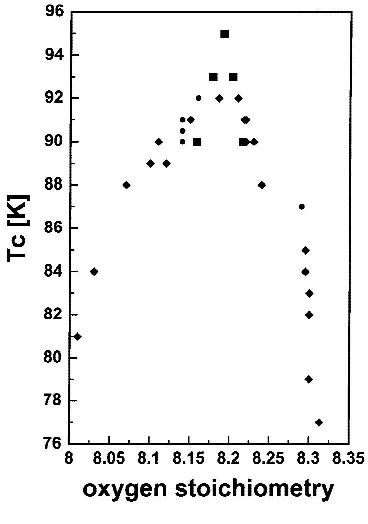

Figure 1.10 – Oxygen stoichiometry dependence of critical temperature for Bi-2212 samples diamonds [59], points [60], squares [37]) from [18].

1.2.3 Influence of cationic stoichiometry on physical properties

It is commonly admitted that the CuO_2 planes are responsible for superconducting conduction in Bi-2212 while other planes act as charge reservoirs. [21, 61–63] The quantity of charge carriers depends among others on the extent of charge transfer from charge reservoir layers to conduction layers. Charge transfer is affected by cation substitution such as Sr^{2+} for La^{3+} or Y^{3+} for Ca^{2+} and results in electron removal (hole doping) or electron addition (electron doping) into the CuO_2 layers.

For example, Yamashita et al. [64] reported that the Bi/Sr ratio in $Bi_{2+x}Sr_{2-x}CaCu_2O_{8+\delta}$ single crystals influences the relation between the critical temperature and the oxygen stoichiometry. Figure 1.11 displays T_c versus O content $(8+\delta)$ plots for different values of x. It turns out that T_c depends both on oxygen stoichiometry and cation composition. For each cation composition, there is an optimal value of δ for which T_c reaches a maximum. To reach the same value of T_c when the bismuth concentration is increased, one has to increase oxygen content: substitution of divalent Sr^{2+} and Ca^{2+} ions by Bi^{3+} trivalent ions has the effect of decreasing the hole density in CuO_2 planes [62] and a higher content of oxygen is needed to counterbalance this supply of positive charges. [65] If Sr^{2+} substitution was only affected by ionic charge, substituting Sr^{2+} by Ca^{2+} should not modify T_c. However, a decrease in T_c is observed, as shown in Figure 1.12. Actually, substitutions (by Bi^{3+} or Ca^{2+} ions) on Sr^{2+} sites cause disorder in the SrO block. Hobou et al. [62] showed that T_c is mainly reduced by disorder in the SrO block and not much by disorder in the other structural blocks. They examined the T_c behavior of $Bi_{2-y}Pb_ySr_2Ca_{1-x}Y_xCu_2O_{8+\delta}$ compounds when varying Pb and Y contents. The Ca^{2+} ions can easily be replaced by rare-earth Y^{3+} ions. [62, 66] The substitution of Ca^{2+} in $Bi_2Sr_2Ca_{1-x}Y_xCu_2O_{8+d}$ by Y^{3+} induces a decrease of the hole carrier concentration. Up to x ~0.5, T_c is improved by the addition of Y^{3+}. But above a value of x=0.5, the system does not behave like a superconductor anymore but becomes a semiconductor and superconductivity is lost. Contrary to Ca^{2+} substitution by Y^{3+}, Bi^{3+} substitution by Pb^{2+} has the effect of increasing hole density in CuO_2 planes. Hobou et al. [62] succeeded to achieve T_c of 98K by controlling the hole concentration in CuO_2 planes through Pb/Y ratio adjustement and reduction of the disorder in the SrO block. They estimate that 98K is the highest T_c that can be reached in optimally doped Bi-2212 compounds.

All these studies on cation substitution in Bi-2212 compounds tend to the same conclusion: cation composition of Bi-2212 compounds has a critical effect on T_c. To achieve the best T_c values, both cation composition and oxygen content have to be optimized.

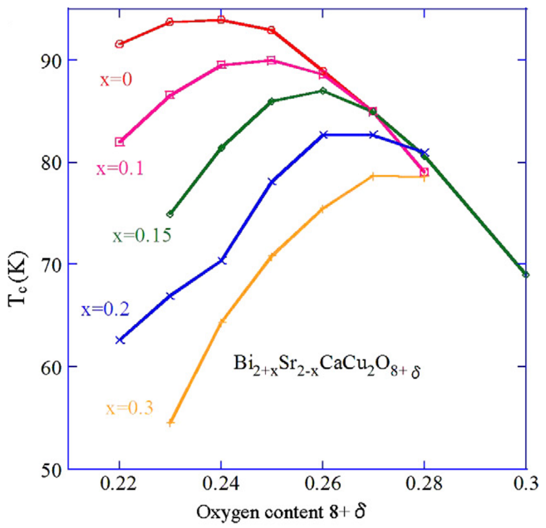

Figure 1.11 – Oxygen stoichiometry ($O_{8+\delta}$) dependence of critical temperature for different x values in $Bi_{2+x}Sr_{2-x}CaCu_2O_{8+\delta}$ single crystals [64].

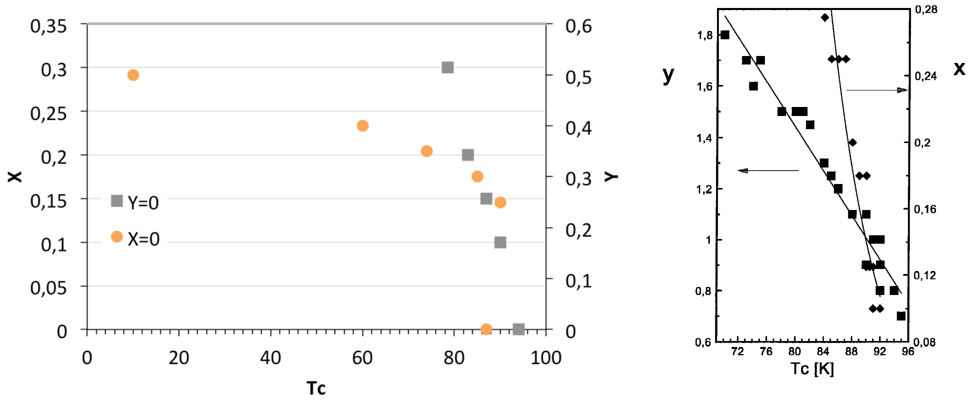

Figure 1.12 – Variation of critical temperature with the concentration of Ca (x,■) and Bi (y,□) for the compound $Bi_{2+x}Sr_{2-y}Ca_{1+y}Cu_2O_{8+d}$ [18].

1.3 Bi-2212 bulk samples from Nexans: processing and applications

In the present section, the processing of bulk samples (i.e. Melt-cast process) is described and some applications of these materials are presented.

1.3.1 Melt-cast process

Bi-2212 synthesis is easier than Bi-2223 synthesis because Bi-2212 is stable over a wide range of temperatures and atomic compositions. [18, 67] On the contrary, single phase Bi-2223 exists only in a narrow region of the Bi_2O_3-SrO-CaO-CuO quaternary phase diagram (see Figure 1.13) and a narrow temperature range. It has to be stabilized with Pb. In addition, Bi-2212 is rather stable when exposed to ambient conditions. [68]

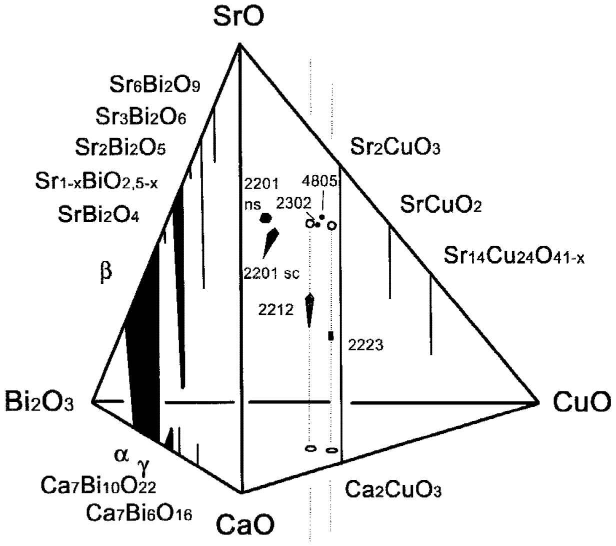

Figure 1.13 – Quaternary diagram of the system Bi_2O_3-SrO-CaO-CuO at 850° in air.

Melt-cast process consists in melting a powder or a mix of powders and pouring the melt into a mold with the desired shape. Tubes, rods or plates can be manufactured. The first stage in the synthesis of melt-cast bulk samples at Nexans [59] is the preparation of a mixture of Bi_2O_3, SrO, CaO, CuO, and BaO with some $SrSO_4$ (whose role is discussed later in this section), in stoichiometric ratios adequately chosen to reach the composition Bi:Sr:Ca:Cu 2:2:1:2. The mixture of powders is then put in a Pt crucible and heated above 1000°C to reach melt state. For the synthesis of rod samples (Figure 1.14b), the melt is then cast into preheated quartz ampoules. In the case of tubular samples (Figure 1.14a), the melt is poured into a preheated rotating mould made of refractory alloy (centrifugal casting). Samples slowly cool down to room temperature and solidify into the moulds. Samples are then annealed to convert the solidified material into Bi-2212. The oxygen content (8+δ) in samples is adjusted by annealing along T-pO_2 trajectories calculated from the diagram given by Schweizer et al. (Figure 1.15) [54]. In summary, melt-cast process is a complex process with many synthesis parameters, such as mold preheating temperature, composition of the powder mixture, parameters of the annealing and oxygenation treatment, etc. For confidentiality reasons, no more details will be given about the industrial process.

The influence of $SrSO_4$ addition during the melt-cast process of Bi-2212 bulk samples has been studied by Kim et al. [69] on Bi-2212 rods and in particular, J. Bock and S. Elschner [70] studied this influence on Nexans bulk tubes. These authors showed that $SrSO_4$ addition affects grain growth during the cooling of the melt in the mold and decreases the risk of micro cracks in the solidified sample. Kim et al. also determined the critical current as a function of $SrSO_4$ weight fraction in rods (Figure 1.16): the critical current is enhanced up to a weight fraction of 6% in $SrSO_4$ and decreases for values of $SrSO_4$ weight fraction higher than 6%. Figure 1.17 compares cross-section SEM micrographs of bulk Bi-2212 rods with (a) 0 wt%, (b) 6 wt%, and (c) 15 wt% $SrSO_4$. At 0 wt% of $SrSO_4$, grains are aligned arbitrarily in the sample (Figure 1.17 (a)). Addition of 6 wt% $SrSO_4$ induces grain alignment in the sample as visible in Figure 1.17 (b). For higher weight fraction additions, inclusions of non-superconducting dendrites of $SrSO_4$ appear in the bulk (Figure 1.17 (c)).

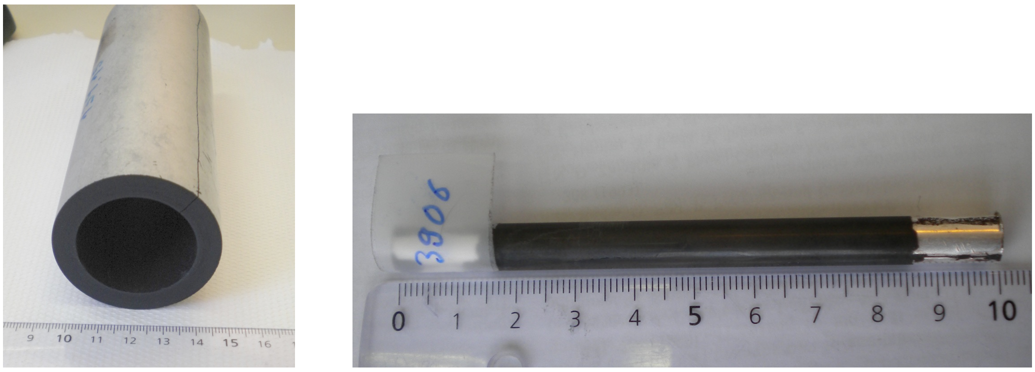

(a) Tube **(b)** Rod

Figure 1.14 – (a) Tube and (b) rod bulk samples synthesized by Nexans.

The microstructure of the melt-cast samples is also influenced by the temperature gradients appearing during the cooling. When the melt is cooling down, the temperature of the region close to the outer surface decreases faster than that of the center of the sample. At the outer surface, faster melt solidification leads to small grain size At the center of the sample, solidification occurs more slowly and grains have much more time to grow. The center region of the samples is also characterized by a significant porosity coming from shrinkage on cooling and/or gas trapping. [71,72]

Figure 1.18 shows half of a 8mm diameter rod where the porosity is visible on the right of the image.

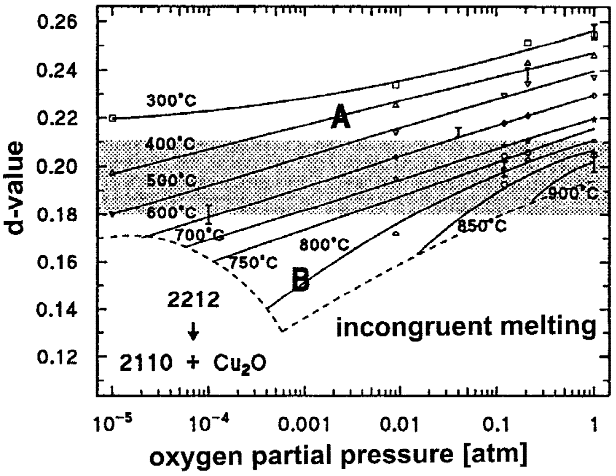

Figure 1.15 – The d value (d = oxygen stoichiometry - 8) of the 2212 phase versus the oxygen partial pressure during heat treatment at different temperatures of 20 mm diameter pellets [54].

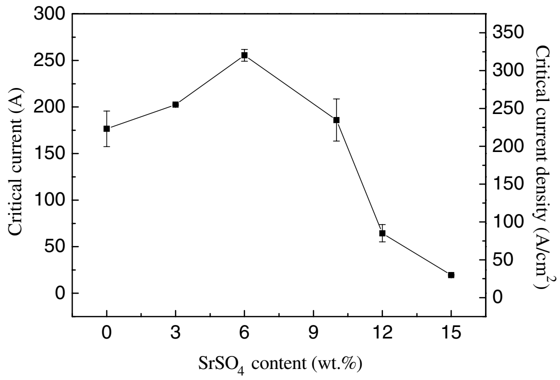

Figure 1.16 – Variation of the critical current of a Bi-2212 rod with weight fraction of $SrSO_4$ [69].

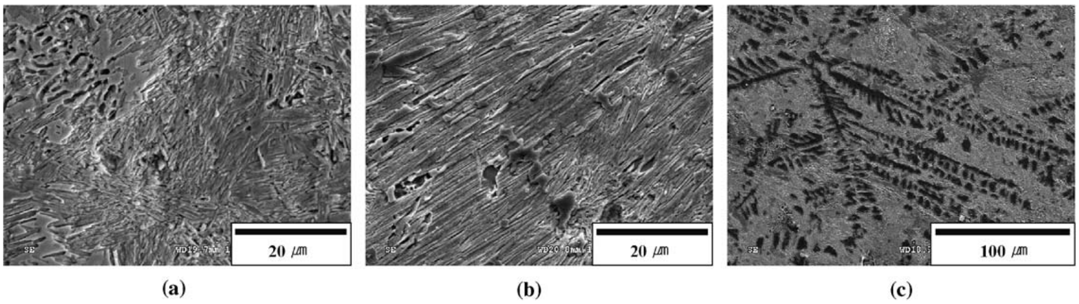

Figure 1.17 – SEM micrographs of cross-section of bulk Bi-2212 rods with (a) no $SrSO_4$ addition, (b) 6%, and (c) 15% of $SrSO_4$ weight fraction [69].

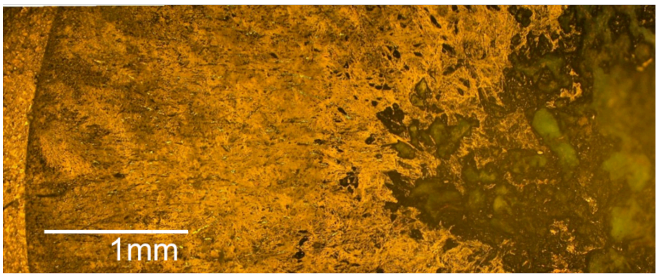

Figure 1.18 – Cross-section optical micrograph of half of a 8mm diameter rod from outer surface (left) to center of the sample (right).

1.3.2 Applications of Nexans Bi-2212 bulks

Since Bi-2212 has a critical temperature around 85K, liquid nitrogen cooling can be used for applications at 77 K, which are attractive for economic reasons. However, the best performances of superconductors are observed at low temperatures and cooling with liquid hydrogen or helium may be required. Compared to Bi-2223, Bi-2212 has several advantages in terms of ease of processing, possibility to shape round wires and higher critical current density at 4.2K. The next two sub-sections focus on the two main applications of the Bi-2212 bulk samples manufactured at Nexans, i.e. as current leads and as fault current limiters.

1.3.2.1 Current leads

When injecting current from a room temperature generator to a system at low temperature, such as the superconducting coil of a magnet, the thermal conductivity of the connecting wires is a major concern. Standard current leads are made of metals such as copper or stainless steel. Due to the high thermal conductivity of these metals, metallic current leads induce high costs linked to a huge electrical consumption of the cooling system to maintain the coil at low temperature. Current leads made of a high temperature superconductor have much lower thermal conductivity combined to low current losses and high electrical conductivity. They are therefore good candidates for current lead applications. The most studied superconductors for current lead applications are bulk Bi-2212 (Figure 1.19), bulk YBCO, or Bi2223 tapes. Such current leads have already shown their efficiency when associated to superconducting magnets in magnetic resonance imagery devices, nuclear magnetic resonance devices, or in particle accelerators. As an example, compared to metallic current leads, the use of superconducting current leads at the Large Hadron Collider in CERN has reduced by 30% the power needed for the cooling system.

Figure 1.19 – Current leads manufactured by Nexans.

1.3.2.2 Fault current limiters [73–76]

In power grids, a fault current can damage line equipment (generator, transformer, fuse) or cause a breakdown of a large part of the electrical network. Fault current limiters (Illustrated in Figure 1.20) in electrical networks are used to limit the huge and fast increase of the current during a fault. An efficient fault current limiter should have a negligible resistance in normal conditions; a rapid and effective response to fault; and an automatic, autonomous, and rapid recovery time. Superconducting fault current limiters (SFCL) work on the basis of the transition from the superconducting state to the normal state. There exist several types of SFCL among which the resistive type has showed the highest performances. When a fault occurs (illustrated in Figure 1.21), the current exceeds the threshold I_c value of the superconductor and within milliseconds, the resistive SFCL transits to normal state. The current flow is thus limited by the resistivity of the SFCL in its normal state. Current limitation is followed by a recovery process during which the SFCL returns to the superconducting state. This process is conditioned by the heat increase produced during the fault. Recovery times are typically a few seconds for thin film superconductors and close to a minute for bulk superconductor SFCLs.

Figure 1.20 – Superconducting Fault Current Limiter from Nexans installed in Germany.

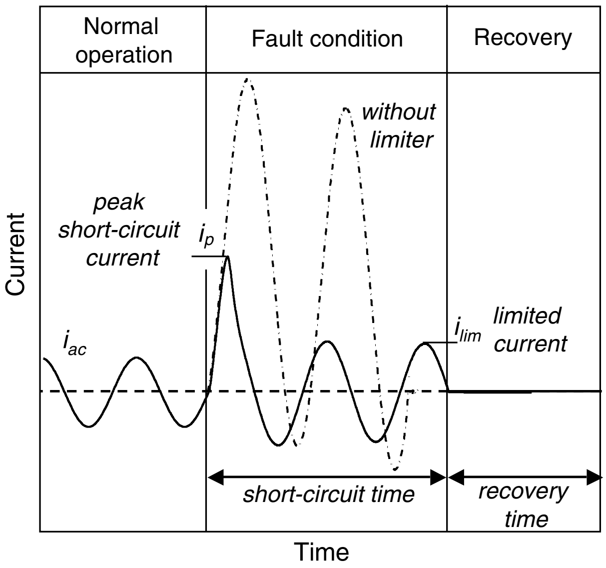

Figure 1.21 – Superconducting Fault Current Limiter operation mode, from [77].

CHAPTER 2 | *Introduction to texture*

Chapter content

2.1 Orientation and texture in crystallography

2.1.1 Notation system for planes and directions

Understanding the discussion of orientations and textures in the following sections requires some familiarity with the notation systems for planes and directions in crystals. In the following, the definitions of planes and directions will be illustrated by figures drawn for an orthorhombic cell, such as will be used to describe the Bi-2212 phase in the next chapters. Figure 2.1(a) shows a typical orthorhombic cell, with $a \neq b \neq c$ and $\alpha = \beta = \gamma = 90°$, where a, b, c are the lengths of the orthogonal base vectors **a**, **b**, and **c** of the unit cell and α, β, γ are the angles between the base vectors (respectively the angles between **b** and **c**, **a** and **c**, and **a** and **b**).

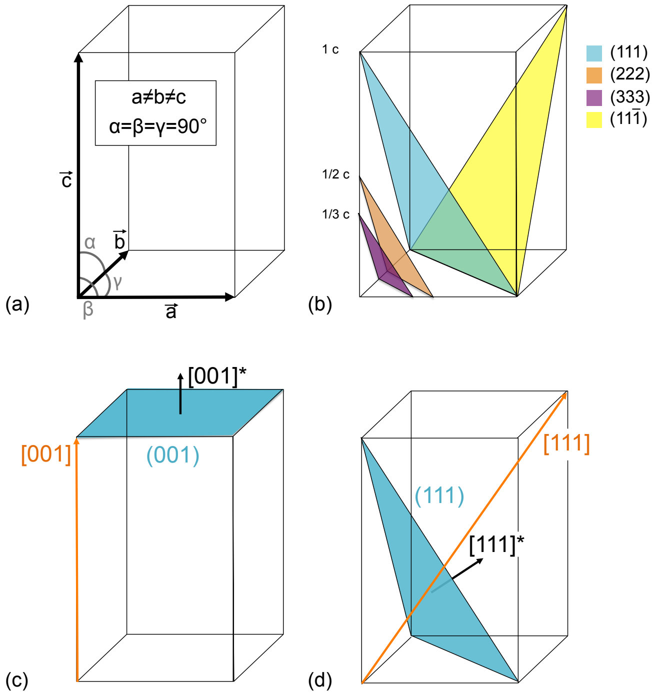

Figure 2.1 – (a) Representation of an orthorhombic cell; (b), (c) and (d) examples of (hk$l$) planes, [hk$l$]* directions perpendicular to (hk$l$) planes and [hk$l$] directions.

By definition, a plane that intercepts **a**, **b**, and **c** at $\frac{1}{h}$, $\frac{1}{k}$, $\frac{1}{l}$ respectively is one of the set of **(hk$l$) planes**, where the three indices (hk$l$) (in parentheses) are called Miller indices. The set of (hk$l$) planes consists of this plane and all planes that are parallel to it and are separated from adjacent planes by a distance d_{hkl}, given for orthorhombic cells by the equation $\frac{1}{d_{hkl}^2} = \frac{h^2}{a^2} + \frac{k^2}{b^2} + \frac{l^2}{c^2}$. One of the examples shown in Figure 2.1(b) corresponds to the (222) plane, which intercepts **a** at $\frac{1}{2}$, **b** at $\frac{1}{2}$, and **c** at $\frac{1}{2}$. Another example (Figure 2.1(c)) shows the (001) plane, which intercepts **a** at infinity, **b** at infinity, and **c** at 1 and is therefore parallel to **a** and **b**. Depending on the symmetry elements of the space group, several sets of (hk$l$) planes may be equivalent by symmetry [1] and are collectively denoted as {hkl} (in curly brackets).

A **direction**, described by the vector **r**=u**a**+v**b**+w**c** is called the [uvw] direction, with the three indices in square brakets. Directions equivalent by symmetry are written $\langle uvw \rangle$ in angle brackets. Figure 2.1(c) and (d) show the [001] direction and the [111] direction as examples. It can be seen that the [111] direction is *not* perpendicular to the (111) plane. This is the general case and the fact that the [001] direction is perpendicular to the (001) plane is a particular case. It is possible to find the u,v,w indices of the direction perpendicular to a set of (hk$l$) planes, but for convenience another notation is introduced and the **direction perpendicular to a set of (hk$l$) planes** will be labeled [hk$l$]*, or <hk$l$>* for all symmetry-equivalent [hkl]* [2]. [001]* and [111]* are shown in Figure 2.1(c) and (d).

In summary:

(hk$l$):	hk$l$ Crystallographic plane of the direct lattice
{hk$l$}:	All sets of hk$l$ planes equivalent by symmetry
[hk$l$]:	hk$l$ Crystallographic direction of the direct lattice
<hk$l$>:	hk$l$ directions equivalent by symmetry
[hk$l$]*:	hk$l$ Direction perpendicular to the (hk$l$) set of planes ≡ reciprocal direction
<hk$l$>*:	Family of directions perpendicular to the {hk$l$} sets of planes ≡ reciprocal familly, also noted **h** or $\overrightarrow{h}$

2.1.2 Orientation in polycrystalline samples - Euler angles

In a perfect single crystal, (hk$l$) planes extend throughout the sample to the surfaces of the crystal. On the contrary, a polycrystalline sample is divided into smaller volumes called **crystallites**: each crystallite can be considered as a small single crystal but there is no continuity between (hk$l$) planes of neighboring crystallites, as illustrated in Figure 2.2a.

---

[1] In an orthorhombic cell : hkl ≡ h-k-l ≡ -hk-l ≡ -h-kl ≡ -h-k-l ≡ -hkl ≡ h-kl ≡ hk-l

[2] It actually corresponds to the direction of the h**a***+k**b***+l**c*** vector in the reciprocal space

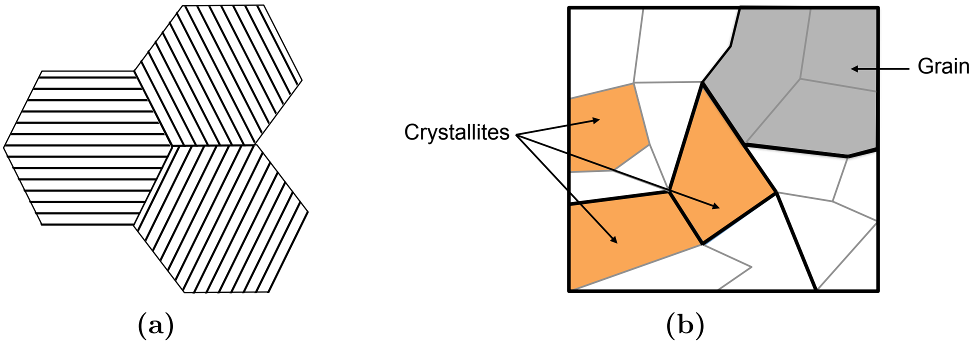

Figure 2.2 – (a) Schematic drawing of a cross-section through 3 crystallites, with the same set of (hk$l$) planes represented in each crystallite. (b) Schematic drawing of a sample where grains are delimited by bold lines (an example of a grain is colored in gray), crystallites are delimited by gray lines (examples of crystallites are colored in orange).

Crystallites do not necessarily correspond to the grains seen in a microscope. Very often, grains are made up of several crystallites, as schematized in Figure 2.2b. Both grains and crystallites have their own shape and size in the sample, depending on the synthesis process. Each crystallite has its own orientation, which can be described by attaching a coordinate system K_C={X_C, Y_C, Z_C} to the crystallite and comparing it to the coordinate system of the sample K_S={X_S, Y_S, Z_S}, as shown in Figure 2.3. The orientation of a crystallite can be defined using three angles called the **Euler angles**. In this thesis, the Euler angles will be defined according to the Roe-Matthies convention described hereafter. The correspondence with other conventions can be found in Table 2.1.

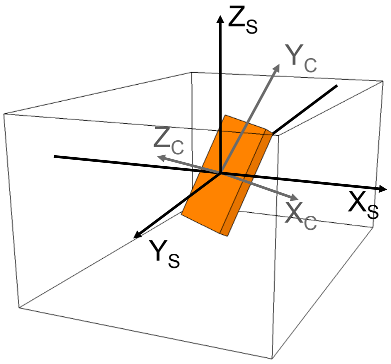

Figure 2.3 – Coordinate system of a crystallite K_C={X_C, Y_C, Z_C} contained in a sample having the coordinate system K_S={X_S, Y_S, Z_S}.

In the Roe-Matthies convention:
$K_C = g \times K_S$ with $g = g_1\ g_2\ g_3 = \{\alpha,0,0\}\{0,\beta,0\}\{0,0,\gamma\}=\{\alpha,\beta,\gamma\}$
where α, β, and γ are three successive angles of rotation that bring the sample coordinate system collinear to the crystallite coordinate system. The successive rotations are depicted in the graphs of Figure 2.4.

1. α corresponds to a rotation of K_S around Z_S that leads to the coordinate system $K'_S=\{X'_S, Y'_S, Z'_S=Z_S\}$. α is defined as the angle that brings X_S onto X'_S (See Figure 2.4(a)).
2. β corresponds to a rotation of K'_S around Y'_S that leads to the coordinate system $K''_S=\{X''_S, Y''_S=Y'_S, Z''_S\}$. β is defined as the angle that brings Z'_S onto Z''_S (See Figure 2.4(b)).
3. γ corresponds to a rotation of K''_S around $Z''_S= Z_C$. X''_S and Y''_S rotate in a plane normal to Z_C, shown in blue in Figure 2.4(c). γ is defined as the angle that brings Y''_S onto Y_C along the circumference of the plane normal to Z''_S. It is the last rotation that brings the sample coordinate collinear with the crystallite coordinate system $K_C=\{X_C, Y_C, Z_C\}$.

As an alternative representation, Figure 2.4(d) shows a projection of the rotations on the circle containing X_S and Y_S (i.e., the grey circle in Figures 2.4(a) to (c)).

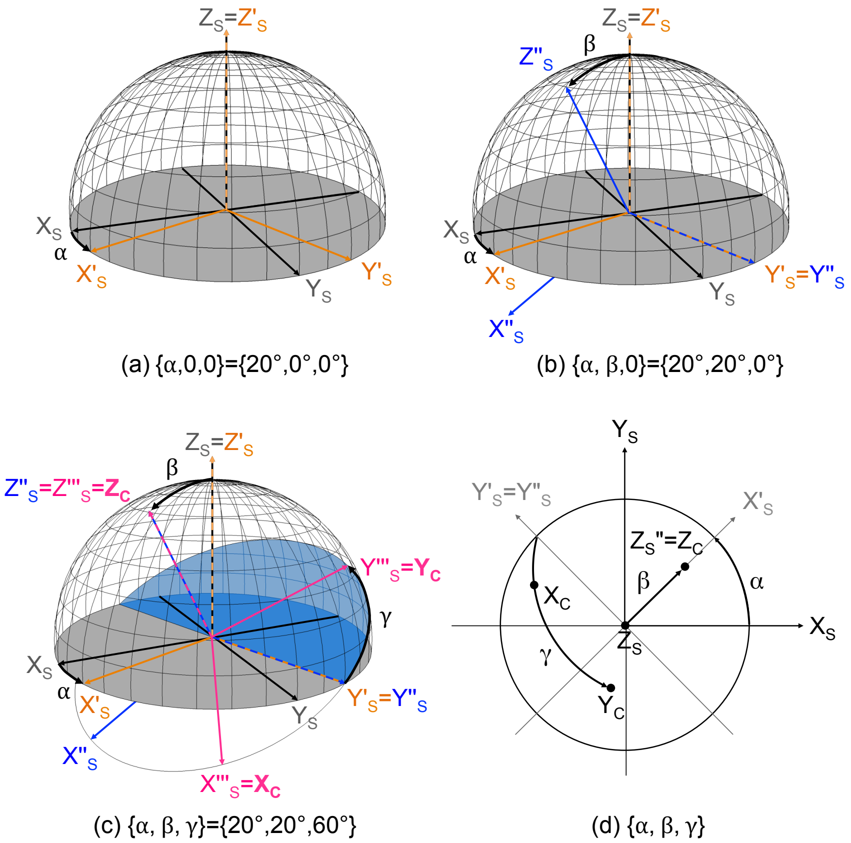

(a) {α,0,0}={20°,0°,0°}

(b) {α, β,0}={20°,20°,0°}

(c) {α, β, γ}={20°,20°,60°}

(d) {α, β, γ}

Figure 2.4 – Euler angles in the Roe-Matthies convention. See text for a description of the sequence of rotations.

Matthies	Roe	Bunge	Canova	Kocks
α	Ψ	$\varphi_1 = \alpha + \pi/2$	$\omega = \pi/2 - \alpha$	Ψ
β	Θ	Φ	Θ	Θ
γ	Φ	$\varphi_2 = \gamma + 3\pi/2$	$\phi = 3\pi/2 - \gamma$	$\Phi = \pi - \gamma$

Table 2.1 – Correspondence of Roe-Matthies Euler angles with other conventions.

2.1.3 Representation of textures [78–83]

Samples with different distributions of crystallite orientations are said to have different crystallographic **textures**. The texture of a sample can be represented by pole figures (see subsection 2.1.3.1) or graphs of the orientation distribution function (ODF - see subsection 2.1.3.2).

2.1.3.1 Pole spheres and pole figures

Pole spheres are centered on the sample reference frame K_S={X_S,Y_S,Z_S} (Figure 2.3). The {hkl} pole sphere of a sample is constructed by drawing the <hk*l*>* directions of all crystallites of the sample intercepted by a sphere of unit radius. Figure 2.5a illustrates the procedure for one crystallite: the [hkl]* direction, normal to the (hk*l*) planes, intercepts the surface of the sphere at a point P called a pole. P is located on the pole sphere by the tilt ϑ_y and azimuth φ_y angles. For easier visualization, the {hkl} pole sphere is usually projected in two dimensions to obtain the {hkl} **pole figure** [84–89]. In this work, the pole figures are drawn using the equal area projection (Lambert or Schmidt projection). Figure 2.5b shows that a pole P is projected on a plane tangent to the north pole of the pole sphere by rotation of the $\overrightarrow{OP}$ vector to $\overrightarrow{Op}$. The pole figure is shown in Figure 2.5c where the coordinates of the pole P are given as $\mathbf{y}=(\vartheta_y,\varphi_y)$.

The complete {hkl} pole figure is constructed by repeating this procedure for all crystallites in the sample. The intensity at each point $\mathbf{y}=(\vartheta_y,\varphi_y)$ of the {hkl} pole figure will be noted $I_h(\mathbf{y})$ and depends on the total volume of the crystallites that have the same orientation of the <hk*l*>* directions. As described in the second part of the chapter, pole figures can be measured from diffraction experiments by rotating the sample at instrumental angles (χ,φ) and measuring the diffracted intensity of the corresponding {hk*l*} reflection, $I_h(\chi,\varphi)$, later transformed into $I_h(\vartheta_y,\varphi_y)=I_h(\mathbf{y})$ in the coordinate system of the pole figure. A pole figure showing diffracted intensities $I_h(\mathbf{y})$ is called a **direct pole figure**. In order to compare different samples and get rid of sample influence (porosity, crystallinity, etc.), diffracted intensities are normalized into pole densities, $P_h(\mathbf{y})$, which depend only on orientation.

$$\int_{\varphi_y=0}^{2\pi}\int_{\vartheta_y=0}^{\pi/2} P_h(\vartheta_y,\varphi_y) sin\vartheta_y d\vartheta_y d\varphi_y = 4\pi \tag{2.1}$$

These pole figures are called **normalized pole figures**. Normalized pole figures are expressed in multiple of random distribution, m.r.d., and a pole figure with 1 m.r.d. for all **y** corresponds to a randomly oriented sample (see Figure 2.6(a)). If no crystallites are oriented in a direction **y**, the corresponding point in the pole figure will have a density of 0 m.r.d.. A single crystal will exhibit an infinite orientation density at some **y** directions, and 0 m.r.d. for all other **y**.

Some other examples of pole figures are shown in Figure 2.6. The pole figures in Fig. 2.6(b) and (d) have higher densities near the equator of the pole figure ($\vartheta_y \simeq 90°$), with a sharper distribution in the case of (b). The pole figures in Fig. 2.6(c) and (d) have higher densities near the center of the pole figure ($\vartheta_y \simeq 0°$), with a sharper distribution in the case of (c). In the case of Fig. 2.6(e), all crystallites have <hk*l*>* directions oriented close to $\vartheta_y = 45°$, $\varphi_y = 45°$.

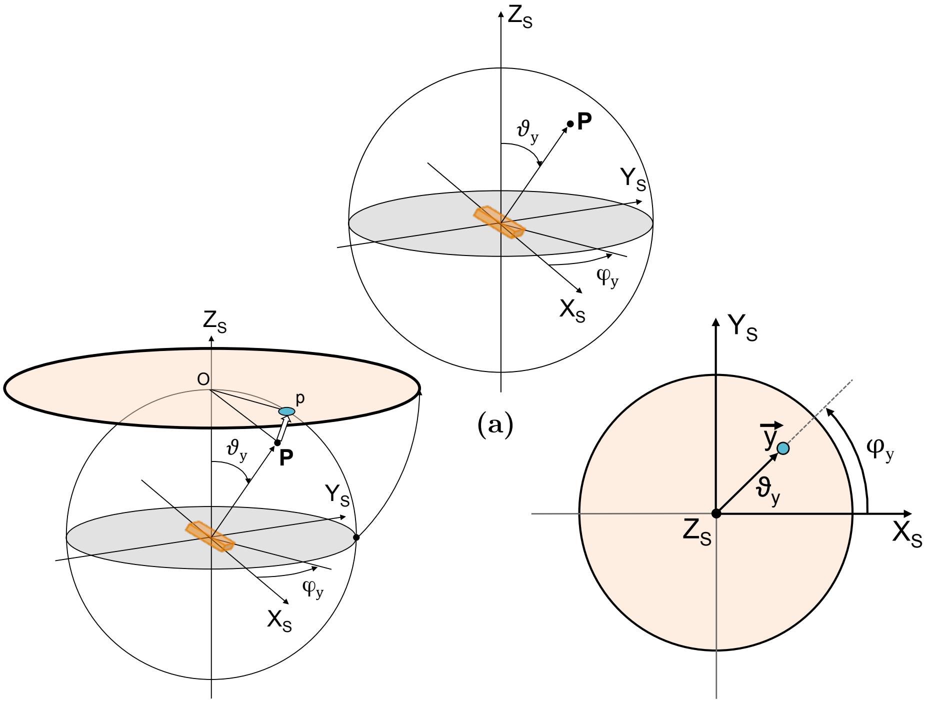

(a)

(b)

(c)

Figure 2.5 – (a) Pole sphere centered on the sample reference frame: the pole P corresponding to one crystallite is the intersection of the sphere with the <hk*l*>* direction normal to the (hk*l*) planes in the crystallite, (b) Projection of the pole P on the pole figure (orange circle) by an equal area projection, and (c) Pole figure with **h** located at $\mathbf{y}=(\vartheta_y = 45°, \varphi_y = 45°)$.

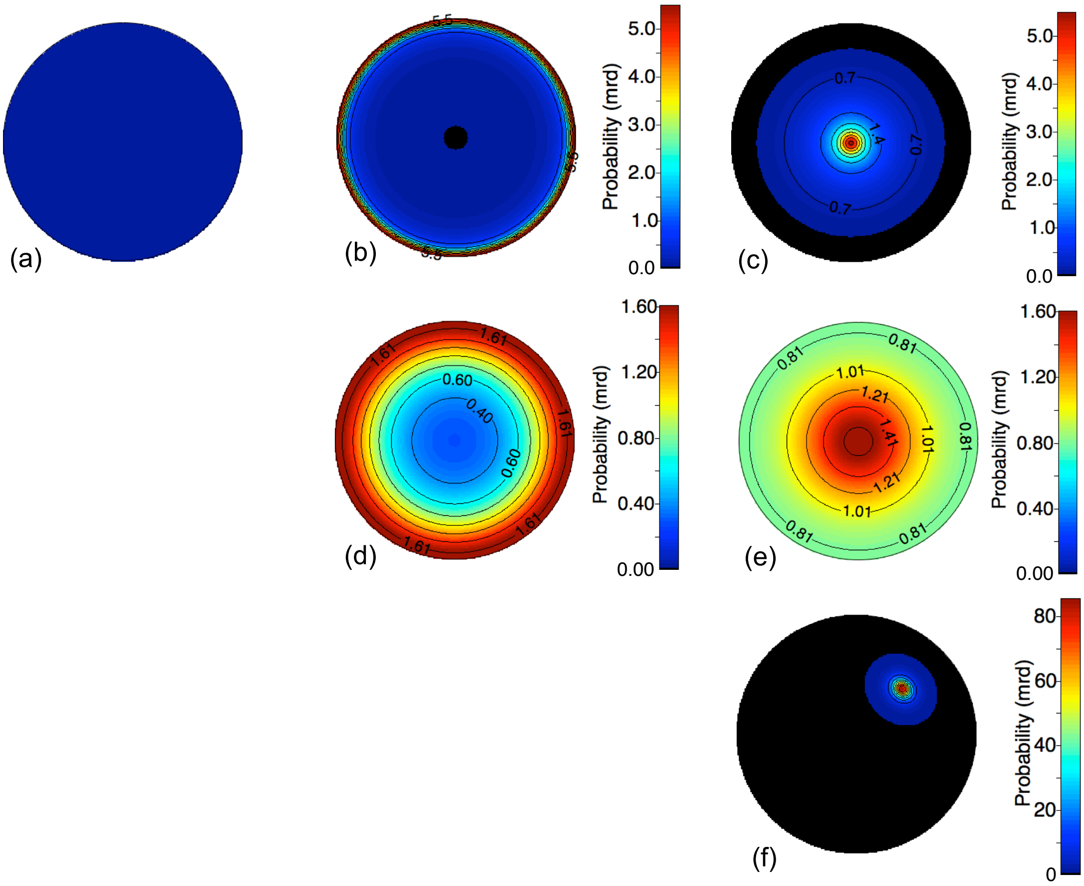

Figure 2.6 – Examples of pole figures:
(a) Pole figure of a texture with a random distribution (1 m.r.d)
(b) Pole figure with **h** located on the equator of the pole sphere, $\vartheta_y \simeq 90°$ and FWHM=10°
(c) Pole figure with **h** located at the center of the pole figure (i.e. around the north pole of the pole sphere) with a sharp distribution (FWHM=10°)
(d) Pole figure with **h** located on the equator of the pole sphere with a large distribution (FWHM=60°)
(e) Pole figure with **h** located at the center of the pole figure (i.e. around the north pole of the pole sphere) with a large distribution (FWHM=60°)
(f) Pole figure with $\mathbf{h}//\mathbf{y}$, with the center of the distribution located at $\mathbf{y}=(\vartheta_y = 45°, \varphi_y = 45°)$ with a FWHM=10°

2.1.3.2 The orientation distribution function

A single pole figure does not constitute a complete description of the texture of a sample. On the contrary, the Orientation Distribution Function, ODF or f(g), reflects the probability of finding a crystallite orientation between g and $g+dg$, where $dg = sin\beta d\beta d\alpha d\gamma$ is the orientation element, defined by the three Euler angles α, β, and γ defined in section 2.1.2. [84–88] The ODF is given by:

$$\int_{\alpha=0}^{2\pi}\int_{\beta=0}^{\pi/2}\int_{\gamma=0}^{2\pi} f(g)dg = 8\pi^2 \tag{2.2}$$

The orientation distribution is often represented as 2D-sections plotted for different values of one of the Euler angles, as shown in Figure 2.7.

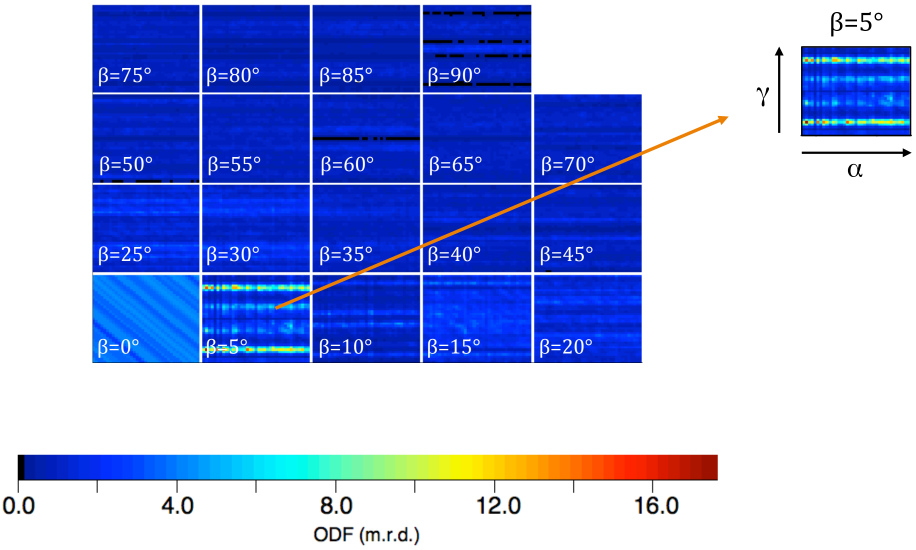

Figure 2.7 – 2D 5° β-sections representing the orientation distribution of a sample. Each cell of the OD is a 180°x180° grid in (α, γ).

The texture strength of samples exhibiting similar orientation distributions may be compared by means of the **texture index (F^2)**, calculated from the ODF through:

$$F^2 = \frac{1}{8\pi^2}\sum_i [f(g_i)]^2 \Delta g_i \tag{2.3}$$

where g_i is the i orientation cell and $\Delta g_i = sin\beta_i \Delta\beta_i \Delta\alpha_i \Delta\gamma_i$ is each discretized OD-cell volume. F^2 is expressed in m.r.d.^{2} and takes values ranging from 1 m.r.d.^{2} for a random powder to infinity for a perfect texture (single crystal).

2.2 Determination of texture from X-ray or neutron diffraction experiments

Experimentally, information about the orientation distribution in a sample can be obtained from diffraction experiments. This is due to the fact that the (hk$l$) planes of a crystallite diffract with constructive interference only for a specific incidence angle of the beam with respect to the planes, as given by Bragg's law :

$$\lambda = 2d\sin\theta_{hkl} \tag{2.4}$$

where λ corresponds to the wavelength of the diffraction source (x-rays, neutrons, etc.), d is the spacing between atomic planes and θ_{hkl} is the Bragg angle measured between the incident beam and the diffracting planes hk$l$.

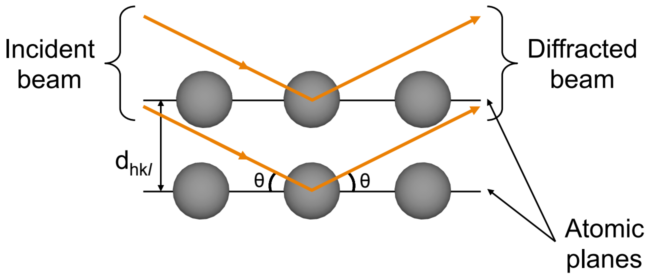

Figure 2.8

The following sections describe the differences between X-ray and neutron experiments (section 2.2.1), the strategy for data collection (section 2.2.2), and how the diffraction data are processed to compute texture (section 2.2.3).

2.2.1 X-Ray diffraction vs. neutron diffraction [78]

The following section describes how the advantages and disadvantages of X-ray and neutron diffraction make them complementary in the field of texture characterization.

X-rays and neutrons are both scattered or absorbed by the matter but they interact differently. X-rays are scattered by the electronic cloud of atoms. For a constant X-ray wavelength, both the scattering factors and absorption increase with the number of electrons of the atom and decrease with $\sin\theta/\lambda$. These trends are represented in Figure 2.9 for different atoms (mainly those contained in the Bi-2212 phase). This phenomenon has two main consequences: first, light atoms, such as hydrogen, scatter much less than heavier atoms. Second, it is difficult to differentiate two atoms having a close number of electrons. In comparison, the neutral charge of neutrons makes them non-interacting with the electronic cloud of the atoms. As the size of atomic nucleus is smaller than the neutron wavelength, the scattering factors vary irregularly across the periodic table. The intensity diffused by an atomic nucleus is isotropic and does not depend on the diffraction angle 2θ allowing high resolution at high angles compared to X-rays. Moreover, neutrons are absorbed only by a few nuclei. Consequences of using neutrons compared to X-rays are that light atoms may have a large contribution to the diffracted intensity, neutrons permit to distinguish between two isotopes, and absorption effects are usually weak.

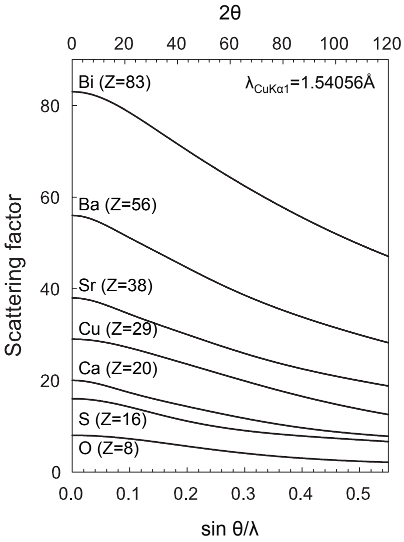

Figure 2.9 – X-ray scattering factors for Bi, Sr, Ca, Cu, O, Ba, and S atoms as a function of 2θ or $\sin(\theta)/\lambda$ for λ=1.54056Å. Raw data from SCATFAC [90].

Concerning instrumentation, an X-ray diffractometer is easy to implement in a laboratory and easily accessible. X-rays are generated by an X-ray tube in a wavelength range of 0.01 to 10 nm. An X-ray tube is composed of two electrodes: a cathode and an anode. When a high voltage is applied between the electrodes, electrons are extracted from the cathode and accelerated to the anode. Electrons collide with the anode and excite the atoms of the anode that emit X-rays by deexcitation. In classical X-ray diffraction, metallic anodes of copper or molybdenum are most frequently used. More intense X-ray beams and a broader choice of wavelengths are found in synchrotrons. Neutrons can be produced using two processes: nuclear fission or spallation. Fission is the most widespread and is used as neutron source in neutron facilities such as ILL (Grenoble, France) [91] or FRM II (Garching, Germany) [92]. Such a neutron source is based on uranium 235 fission in two lighter atoms and some neutrons. The production of neutron causes a chain reaction (see Figure 2.10) of fissions leading to the formation of neutron beams. Spallation is based on a different principle. Protons are accelerated towards a neutron-rich nucleus. After the impact, the nucleus decomposes and expels some neutrons. This process is better controlled than fission because it can be stopped by stopping the proton bombardment. This type of source is used at SNS (Oak Ridge, USA) [93] or at SINQ (Villigen, Switzerland) [94].

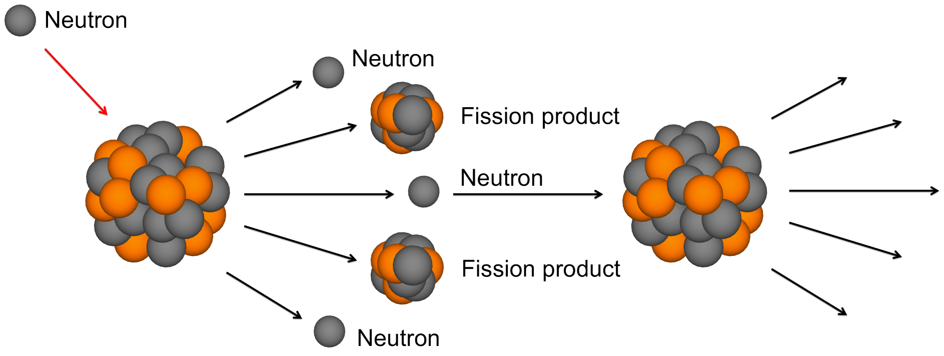

Figure 2.10 – Illustration of the nuclear fission.

Measurement time for texture experiments can be considerably longer with a laboratory X-ray diffractometer than with neutrons. Neutron experiments are typically carried out in few hours (on the beam lines having highest intensities, such as the one used for this thesis) while X-ray experiments in the lab may last from a few days to 1 week.

X-rays probe typically the 10 μm-thick surface layer in our samples and results in data affected by surface effects and sensitive to local variations. The weak interaction of neutrons with matter induces a larger penetration depth. Neutrons penetrate in the bulk so that a larger sample volume is probed and surface effects can be neglected. To achieve a good statistics, the number of grains probed should be around 10^4 grains, to correctly represent the orientations. This is easily accessible using neutron diffraction. Another advantage of neutrons compared to X-rays is that there is no defocusing with neutrons. Complete sets of data can be measured while with X-rays, defocusing causes a limitation of measurement range in χ. As neutrons probe the bulk of the sample, a global view of the sample is obtained and the presence of minor phases can be evidenced. The main disadvantage of neutron experiments is the restricted access to neutron facilities, with beam time allocation depending on successful proposals.

2.2.2 Measurement strategy

As explained in section 2.1.3.2, the determination of the orientation distribution requires the measurement of several pole figures. In order to achieve good statistics, resolution and reliability for the OD calculation, as many pole figures as possible should be measured. This is achieved by adopting a whole pattern analysis approach. In practice, the sample is mounted at the center of a Eulerian cradle. The three rotation axes are represented in Figure 2.11 where ω is the rotation angle of the Eulerian cradle around the vertical axis, χ is the rotation angle of the sample around the normal to the cradle plane, and φ is the rotation angle of the sample around the normal to the sample surface. The ω angle is kept constant. The choice of the ω angle depends on the fact that only the pole figure of the {hkl} reflection whose corresponding 2θ is equal to 2ω is measured completely (Cf. Figure 2.12a). All the other pole figures exhibit a blind area in their centers due to localization corrections [95] (Cf. Figure 2.12b). Therefore the ω value should be chosen so that 2ω is in the range of 2θ where the reflections of most interest are located. Intensity vs. 2θ data are then collected with a 2D detector for different sets of instrumental angles (χ, φ), which can be later transformed into (ϑ_y, φ_y) in the coordinate system of the pole figure. Exact details of measurement conditions and selected angle ranges for the experiments carried out in this thesis work will be given in the relevant chapters.

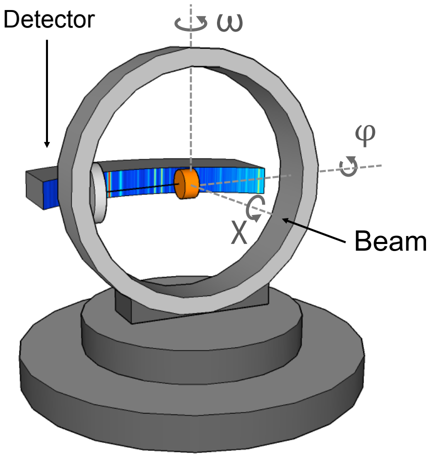

Figure 2.11 – Illustration of a Eulerian cradle, refer to the text for a description of the rotation angles.

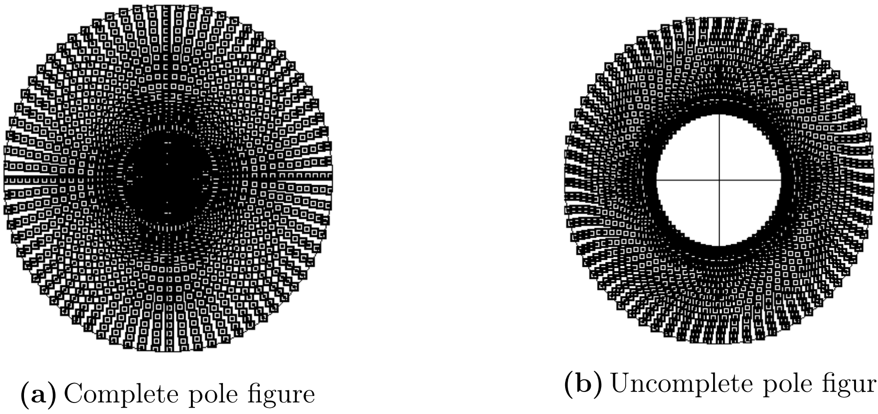
(a) Complete pole figure **(b)** Uncomplete pole figure

Figure 2.12 – Pole figure coverage of (a) fully covered pole figure measured at 2ω=2θ and (b) non fully covered pole figure measured at $2\omega \neq 2\theta$.

2.2.3 Modeling diffraction patterns by using the Rietveld method [79, 87, 89, 96–103]

Data collection results in a series of I vs. 2θ patterns, each of these patterns being obtained for a different (χ, φ). Each pattern is then fitted by Rietveld refinement [96], a method based on a least squares refinement procedure where a calculated pattern is fitted to an observed powder diffraction pattern by minimizing the function:

$$M = \sum_i w_{io}(y_{io} - y_{ic})^2 \tag{2.5}$$

where $w_{io} = \frac{1}{y_{io}}$ is the weight of each observation point, y_{io} is the intensity measured at the ith step and y_{ic} is the intensity calculated at the ith step using the following equation [89]:

$$y_{ic} = y_{ib} + \sum_{\Phi=1}^{N_\Phi} S_\Phi \sum_{k=K_1}^{K} j_{\Phi k} Lp_{\Phi k} P_{\Phi k} |F_{\Phi k}|^2 \Omega_{i\Phi k} A_i \tag{2.6}$$

where

- y_{ib} is the background associated to measured intensity y$_{io}$
- S_Φ is a scale factor, proportional to the volumic fraction of each refined phase Φ
- $j_{\Phi k}$ is the multiplicity factor of the reflection k for phase Φ
- $Lp_{\Phi k}$ is the Lorentz-polarisation factor
- $P_{\Phi k}$ is a correction factor describing non-random texture of phase Φ
- $|F_{\Phi k}|$ is the modulus of the structure factor of phase Φ
- $\Omega_{i\Phi k}$ describes the profile function of the peaks of phase Φ, which represents instrumental and sample broadenings

- A_i is an absorption factor which takes into account the experimental and sample geometries

The Rietveld method calls for the use of a known structural model of the crystallographic phases (space group and approximate values of cell parameters and atomic positions). The factors in Equation 2.6 are computed by a software from a set of parameters which the user can choose to fix or refine in order to reach a good match between the calculated and the experimental pattern. In the case of the pattern of a sample with random texture, the most commonly refined parameters are:

- the Instrumental function
- Background function
- 2θ shift
- Scale factors
- Lattice parameters $(a, b, c, \alpha, \beta, \gamma)$
- Atomic positions (x, y, z)
- Atomic site occupancies
- Temperature factors B

In the case of a textured sample, the intensities are modified by comparison with the case of a non-textured sample, as shown by the factor $P_{\Phi k}$ in Equation 2.6. There are several models for texture calculation, as discussed in detail in [89]. The present work relies on the Extended-Williams-Imhof-Matthies-Vinel (**E-WIMV**) model that has the advantage of allowing the use of irregular pole figure coverage. This E-WIMV model is presented in the next section while the last two sections of the chapter come back to a description of the other factors in Equation 2.6 and the reliability factors of the refinement.

2.2.3.1 E-WIMV model for texture calculation [84, 89, 97, 104]

The Extended-Williams-Imhof-Matthies-Vinel (**E-WIMV**) model[1] for OD refinement is based on an entropy iteration algorithm. Compared to the WIMV model, E-WIMV involves the reflection weight w_h in the calculation algorithm. The E-WIMV model has already been used in many studies and proved its effectiveness [104–109]. At the first step of the texture calculation, measured pole figures ($P^{exp}_{\mathbf{h}}(\mathbf{y})$) are extracted from the experimental dataset acquired in $(2\theta,\ \omega,\ \chi, \varphi)$. An initial OD ($f^0(g)$) is calculated using these experimental pole figures:

$$f^0(g) = N_0 \left(\prod_{h=1}^{I} \prod_{m=1}^{M_h} P^{exp}_{\mathbf{h}}(\mathbf{y}) \right)^{\frac{1}{IM_h}} \tag{2.7}$$

---

[1] The March-Dollase approach and a comparison between E-WIMV and March-Dollase will be discussed in the next chapter

The variables used in this equation are:

$f^0(g)$: Initial OD calculated using experimental pole figures
N_0: Normalization factor
$P^{exp}_{\mathbf{h}}(\mathbf{y})$: Experimental pole figures
I: Number of experimentally measured pole figures
M_h: Pole multiplicity

$f^0(g)$ and $P^{exp}_{\mathbf{h}}(\mathbf{y})$ are introduced in the algorithm to calculate $f^{n+1}(g)$, the OD calculated at the n+1 step:

$$f^{n+1}(g) = f^n(g) \prod_{h=1}^{I} \prod_{m=1}^{M_h} \left(\frac{P^{exp}_{\mathbf{h}}(\mathbf{y})}{P^n_{\mathbf{h}}(\mathbf{y})} \right)^{r_n \frac{w_h}{IM_h}} \tag{2.8}$$

The variables used in the iteration are:
$f^n(g)$: OD calculated at the nth step
$f^{n+1}(g)$: OD calculated at the n+1 step
$P^n_{\mathbf{h}}(\mathbf{y})$: Pole figures calculated at the nth step
r_n is a relaxation parameter such that 0<r$_n$<1, defining the convergence speed of the algorithm
w_h: The reflection weight
n: The number of iterations, defined by the user

The iteration procedure is schematized in Figure 2.13. At each iteration cycle (n), pole figures, $P^n_{\mathbf{h}}(\mathbf{y})$ are calculated using the fundamental equation of quantitative texture analysis (equation 2.9):

$$P_{\mathbf{h}}(\mathbf{y}) = \frac{1}{2\pi} \int_{h//y} f^n(g) d\tilde{\varphi} \tag{2.9}$$

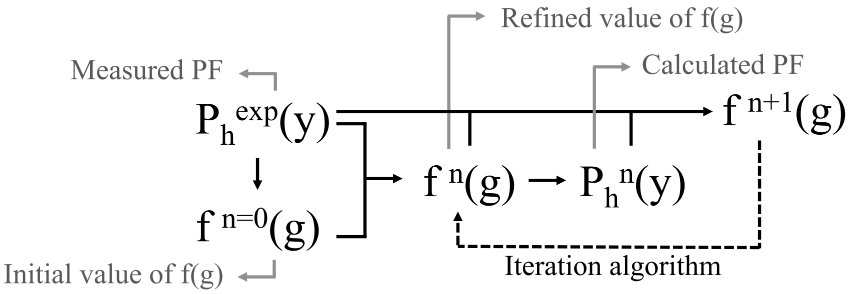

Figure 2.13 – E-WIMV iteration procedure, see text for a description of the procedure.

Figure 2.14 shows that calculated pole figures can be obtained from the OD even if the experimental pole figure was not complete, thanks to the fact that each cell of a pole figure is built using different cells of the ODF and inversely. Figure 2.14(a) represents the pole figure coverage of a 5°x5° experiment in (χ, φ) made on an Inel X-ray four circle diffractometer. Figure 2.14(b) and (c) are respectively the {200} experimental and calculated pole figures.

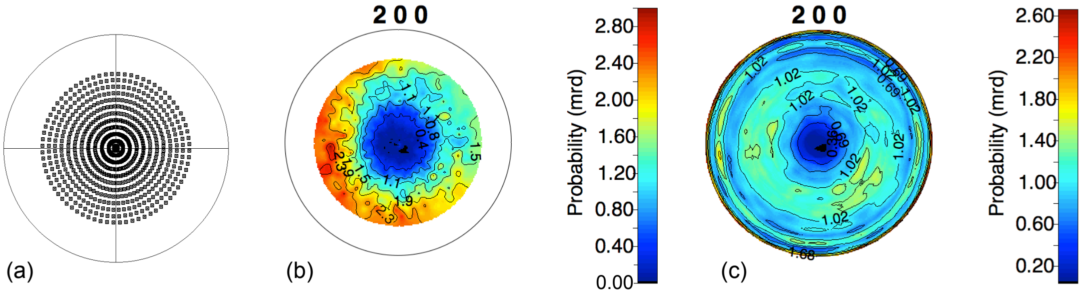

Figure 2.14 – Example of (a) a pole figure coverage, (b) Experimental pole figure and (c) calculated pole figure using E-WIMV model on a dataset acquired on an Inel instrument.

2.2.3.2 Description of parameters in the Rietveld refinement [78, 87]

The background [87]

The most used background in Rietveld refinements is a polynomial function in 2θ

$$bkg(2\theta_i) = \sum_{n=0}^{N_b} a_n (2\theta_i)^n \tag{2.10}$$

with N_b the polynomial degree and a_n the polynomial coefficients

The Lorentz-polarisation factor

The Lorentz-Polarization factor (**Lp**) results from two contributions: the Lorentz factor and the polarization factor. The Lorentz factor depends on the Bragg angle (θ) and on the instrument geometry. The polarization factor takes into account the polarization of the incident beam by a monochromator. The Lp factor is independent of the structural model. As an example, for a Bragg-Brentano geometry instrument, the Lorentz-Polarization factor is expressed as:

$$Lp = \frac{1 + \cos^2(2\theta_m)\cos^2(2\theta)}{2\sin^2\theta\cos\theta} \tag{2.11}$$

with θ_m being the Bragg angle of the monochromator crystal.

The structure factor

The structure factor is of great importance in the solution and refinement of crystal structures because it depends on the atomic positions of the atoms in the unit cell. More specifically, $F_{\Phi k}$ for reflection k of a phase Φ containing N atoms in the cell may be expressed as:

$$|F_{\Phi k}|^2 = m_k \left| \sum_{n=1}^{N} f_n e^{-B_n\left(\frac{\sin\theta}{\lambda}\right)^2} e^{2\pi i(hx_n+ky_n+lz_n)} \right|^2 \tag{2.12}$$

where

m_k is the multiplicity of the k reflection

f_n is the atomic scattering factor of the nth atom

B_n is the temperature factor of the nth atom

x_n, y_n, z_n are the coordinates of the nth atom in the unit cell

The first exponential term is angle-dependent: when θ increases, the intensity of the reflections decrease. The exponential term also contains the temperature factor B, also called Debye-Waller factor. The temperature factor is proportional to the mean square atomic displacement, $\langle u\rangle^2$, through the Debye-Waller equation: $B = 8\pi^2 \langle U\rangle^2$.

The profile function

The profile of a Bragg peak is described by an experimental function *h(x).* This function results from the convolution of an instrumental function *g(x)* and a sample function *f(x)* as:

$$h(x) = b(x) + \int_{-\infty}^{+\infty} f(y)g(x-y)dy = b(x) + f(x)\otimes g(x) \tag{2.13}$$

b(x) is the background contribution (see above). Various models exist to describe the peak profile: Gaussian, Lorentzian, Voigt, Pseudo-Voigt, Pearson VII. **P**seudo-**V**oigt (**PV**) is the most frequently used function. The Pseudo-Voigt function is a linear combination of a Gaussian and a Lorentzian function:

$$PV(2\theta_i) = \eta L(2\theta_i) + (1-\eta)G(2\theta_i) \tag{2.14}$$

The instrumental function, *g(x)*, is defined for each experimental setup. Various aberration profile contributions are at the origin of the instrumental function. These contributions can be regrouped in two categories: geometrical aberrations (beam divergence, optics misalignments, collimator slits width, etc.) or physical aberrations (emitted spectral width and distribution of the incident radiation). *g(x)* is most of the time determined with a standard reference sample (LaB$_6$, Corundum).

The peak width, characterized by the full width at half maximum, FWHM , varies with the diffraction angle 2θ according the **Caglioti formula** [110]:

$$FWHM^2 = H_k^2 = Utan^2\theta + Vtan\theta + W \tag{2.15}$$

The parameters U, V, and W provide information about the resolution of the diffraction instrument. In a Rietveld refinement, the U,V and W parameters are usually defined for a given experimental setup and kept unchanged for unchanged experimental setup. Sample contribution [79, 111–114]

The sample function, *f(x)*, depends mainly on the sample microstructure. Peak broadening occurs when there are local distortions (crystallite size and/or microdistortions) that do not affect the mean value of the lattice constants. There are several ways to describe the broadening due to crystallite size. In the case of an isotropic crystallite size (Figure 2.15a), the easiest way to estimate the mean crystallite apparent size, $\langle R \rangle$ is to use the Scherrer formula:

$$\langle R \rangle = \frac{\lambda K}{H_L \cos\theta} \tag{2.16}$$

The Scherrer formula relates the mean crystallite apparent size to H_L, the full width at half maximum of the peak at an angle 2θ. K is the Scherrer constant usually taken as 0.9 or 1.0.

In the case of crystallites having anisotropic sizes, more elaborate models are needed, such as the Popa approach used in the present work. This model consists in developping the crystallite radius in a convergent series of symmetrized spherical harmonics. The coefficients of the harmonics are refinable parameters. Figure 2.15b provides an example of an anisotropic crystallite with a platelet shape model for an orthorhombic space group using three terms of the series.

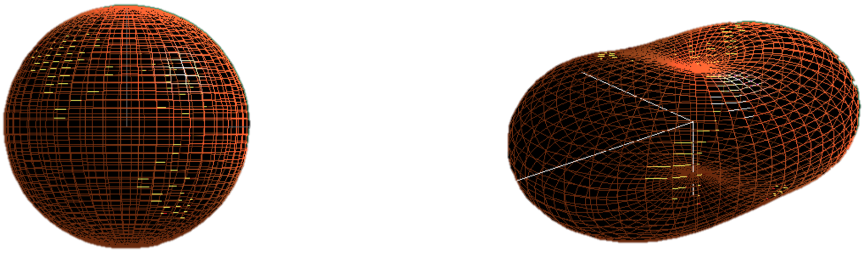

(a) Isotropic size **(b)** Anisotropic size

Figure 2.15 – Crystallite shape obtained using (a) first term of the series and (b) three terms of the series in the orthorhombic crystal system.

2.2.3.3 Reliability factors [89]

Reliability factors are values that express the agreement between calculated data and experimental data. One should keep in mind that comparison of experimental and calculated profiles is also a good criterion for judging of the refinements quality.

Reliability factor of the weighted profile R_{wp}

The Rwp value is dominated by the profile function and is not very sensitive to structural parameters; it mainly reflects the profile comparison.

$$R_{wp} = \sqrt{\frac{\sum_i w_{io}(y_{io} - y_{ic})^2}{\sum_i w_{io} y_{io}^2}} \tag{2.17}$$

w_{io} are generally assigned the value $1/y_{io}$. Ideally, this R_{wp} factor should approximate the expected R value, R_{exp}.

Expected reliability factor R_{exp}

The R_{exp} reflects the quality of the experimental data and can be used as an indication of what is the best result that could be achieved from a set of experimental data.

$$R_{exp} = \sqrt{\frac{(N - P)}{\sum_i w_{io} y_{io}^2}} \tag{2.18}$$

where N is the number of points and P is the number of parameters.

Goodness of fit

The goodness of fit is the ratio between R_{wp} and R_{exp}. It should ideally approach 1.

$$\chi^2 = \frac{R_{wp}}{R_{exp}} \tag{2.19}$$

Bragg *R*-factor

The Bragg factor is used to calculate the agreement between measured and calculated intensities. Contrarily to R_{wp}, this reliability factor is sensitive to structural parameters and not to profile parameters.

$$R_B = \frac{\sum |I_{obs} - I_{calcl}|}{\sum |I_{obs}|} \tag{2.20}$$

CHAPTER 3 | *Diffraction methodology/Case study of a Bi-2212 tube*

The previous chapters described some theoretical principles about superconductivity and texture calculation. This chapter reports the quantitative characterization of the texture of a Bi-2212 tube by different techniques. The chapter starts with a macroscopic and microscopic presentation of the tube sample. Then section 3.2 reports the phase identification and crystallographic parameters determination from a θ-2θ X-ray pattern profile analysis of the tube. The chapter continues with quantitative texture analysis (QTA) using the ILL neutron facilities and a X-ray 4-circle diffractometer. The instrument components, sample preparation, and sample mounting are described in details in Sections 3.3 and 3.4, respectively, while the analysis of neutron and X-ray data is discussed in Section 3.5. The last section (Section 3.6) discusses the limitations and application of preferred orientation determination using the March-Dollase function, i.e., the approach currently used at Nexans Superconductors R&D center.

Chapter content

3.1 Sample description

This section is devoted to the description of the bulk tube studied in this chapter. First the tube is described macroscopically in terms of morphology. Then a microscopic study is presented with the observation of the microstructure and phase identification by EDX.

3.1.1 Description of the tube

The sample studied all along this chapter is a bulk melt-cast processed tube dedicated to Fault Current Limiter (FCL) applications [115]. The tube has an outer diameter of 50mm and an inner diameter of 35mm. It was prepared by a melt-cast process as described in the first chapter (see Section 1.3.1). Figure 3.1 shows two images of the tube with the outer surface coated with silver to be further connected to the shunt via soldering [115]. For all measurements, this silver coating is removed by polishing or by cutting.

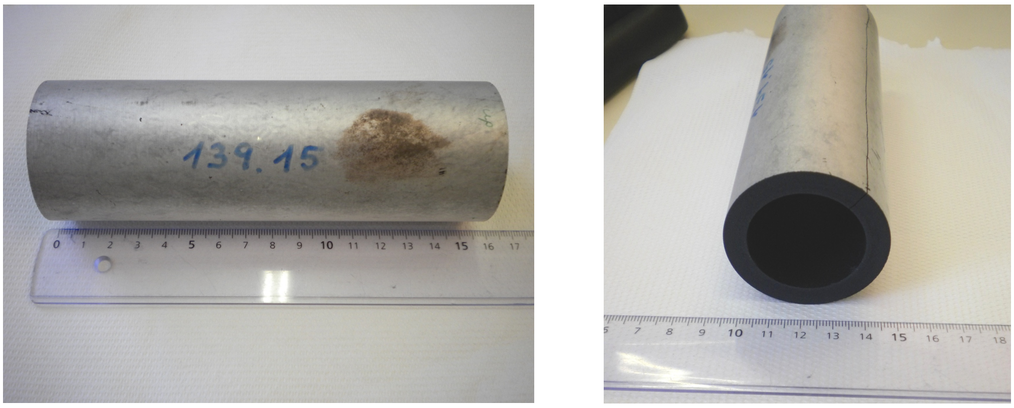

(a) **(b)**

Figure 3.1 – Tube studied in this chapter. The tube has an outer diameter of 50mm and an inner diameter of 35mm.

3.1.2 Microstructure characterization

Scanning Electron Microscopy (SEM) was used to observe a polished longitudinal cross-section of the tube. Figure 3.2 illustrates the position of the longitudinal cross-section in the tube. The face observed with SEM is represented in orange in Figure 3.2a. Figure 3.2b shows an overview optical micrograph, where a porous region of ~2.5 mm thickness is clearly visible as a darker zone. Figure 3.3 displays a panorama made up of a series of SEM micrographs, corresponding to the orange rectangle drawn in Figure 3.2b The panorama is done from the inner part (top left) to the outer part (bottom right) of the tube and illustrates in more detail the variation of microstructure across the tube wall thickness. The first 500μm, close to the inner edge, are porous with second phase inclusions. At the end of this 500μm region, second phase inclusions are more elongated with a length varying between 10μm and 100μm. After these two regions, over a length of 600μm, the tube is dense with approximately 1/3 of the micrograph area corresponding to second phase inclusions. The next 2.5 mm correspond to the porous region, less visible than in Figure 3.2a because the least porous zone was selected for the panorama (see the rectangle in Figure 3.2b). From the end of the porous region to the outer surface of the tube, the size and amount of second phase inclusions is decreasing and the Bi-2212 matrix is predominant. This evolution of microstructure from inner surface to outer surface justifies the study of texture in three different regions of the tube (See Chapter 4). Hereafter, they will be called "inner", "center", and "outer" for parts of the tube cut respectively (i) close to the inner surface, (ii) between the end of the porous region and the outer surface, and (iii) close to the outer surface. Figure 3.4 illustrates the position of the three parts on the tube cross-section.

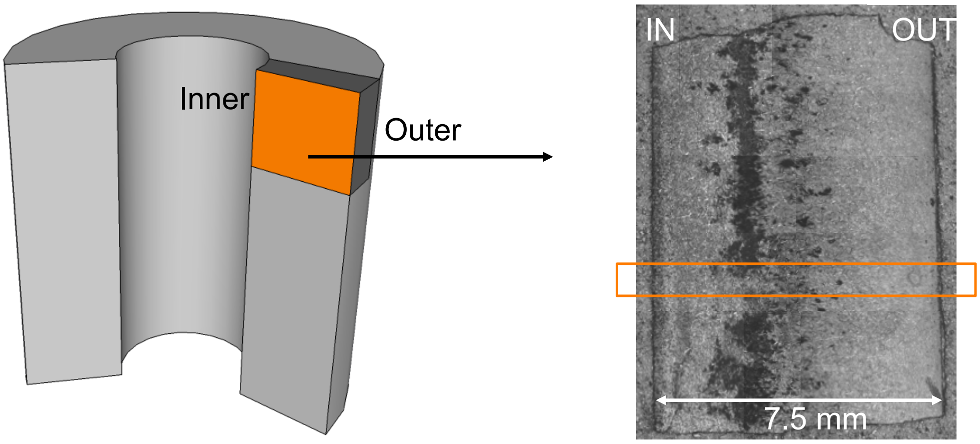

(a) **(b)**

Figure 3.2 – (a) Illustration of the longitudinal cross-section cut in the tube for SEM observations. A piece of the tube in dark gray and orange was cut longitudinally. The face observed in the microscope is the one in orange. (b) Image of the cross-section acquired with an optical microscope.

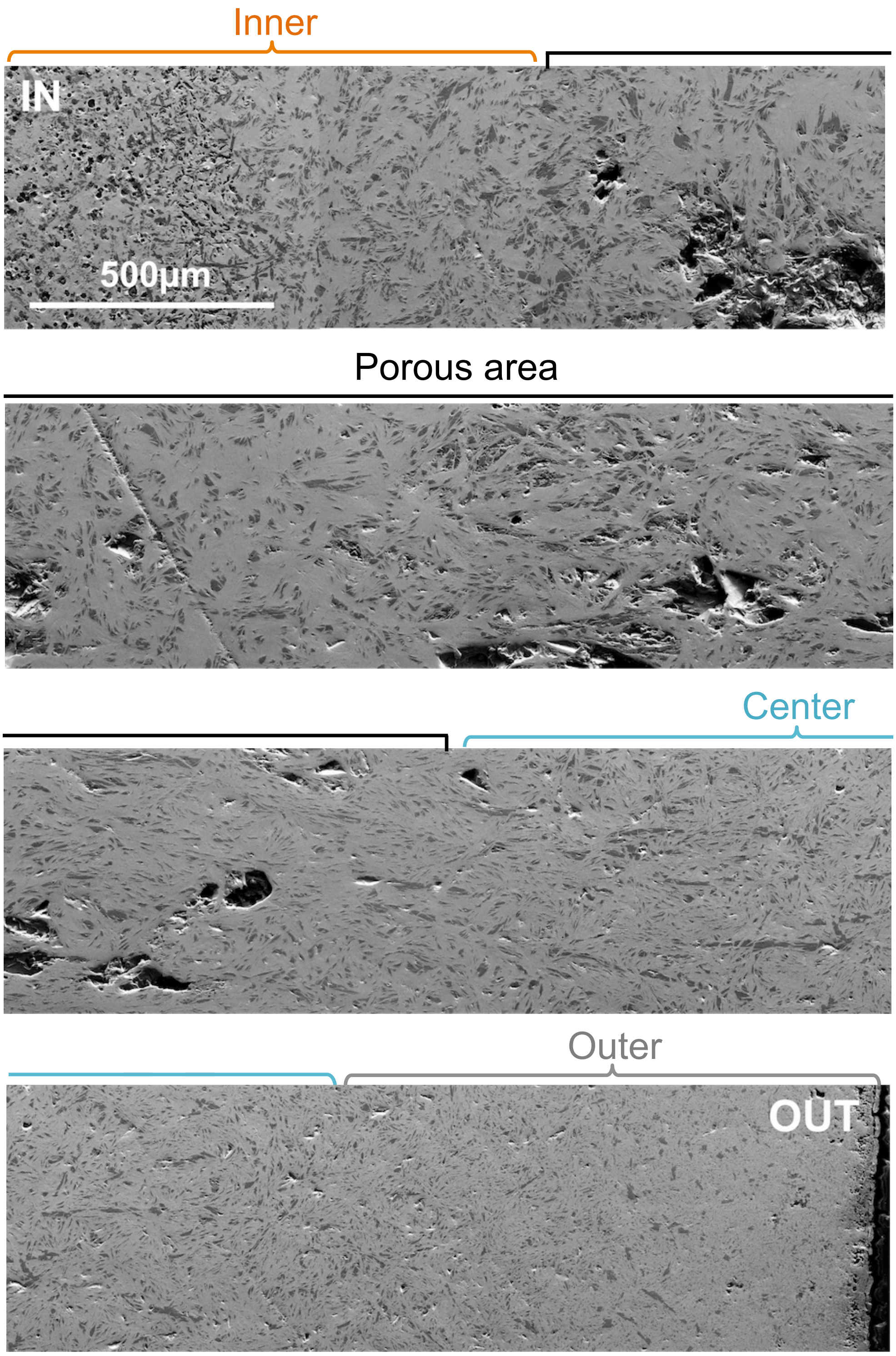

Figure 3.3 – Panorama of a cross section across the tube wall made with SEM micrographs. The panorama is done from the inner part to the outer part of the tube. See Figure 3.2 for details about sample positioning in the tube.

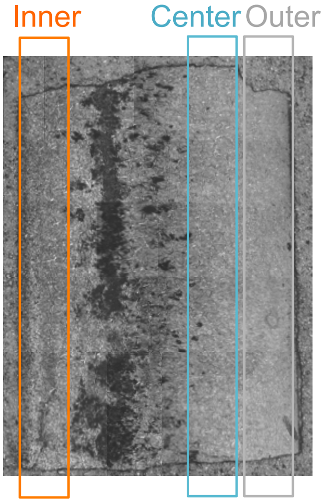

Figure 3.4 – Description of the different parts of the tube: inner (close to the inner edge of the tube), center (between the end of porosity and the outer edge of the tube), and outer (close to the outer edge of the tube).

3.1.3 Phase identification using EDX

The average elemental ratio of each phase was measured with an energy dispersive X-ray spectrometer (EDX) coupled to a scanning electron microscope. Figure 3.5 presents higher magnification SEM micrographs of the polished cross-section of the tube. Micrograph (a) is a view of a section close to the inner edge of the tube and micrograph (b) of a section at the center of the tube. The presence of second phases was evidenced by the EDX measurements. In Figure 3.5a mid-gray grains are $(Ba,Sr)SO_4$ grains and dark gray grains are $(Sr,Ca)_2CuO_3$ grains. In Figure 3.5b dark gray grains are $(Sr,Ca)CuO_2$ and dark gray grains with shiny center are $(Ba,Sr)SO_4$ grains. On both Figure 3.5a and Figure 3.5b, the light gray matrix corresponds to an average cation composition $Bi_{2.26}Sr_{2.25}Ca_{0.71}Cu_{1.78}O_x$. Average elemental ratios calculated from EDX measurements for the different phases are listed in Table 3.2.

The presence of these four phases corresponds to what is usually observed in annealed melt-cast samples. The annealing treatment drives the formation of the Bi-2212 phase by transformation of the Bi-2201 and Ca- and Cu-rich second phases of the as-melt-cast sample (not yet annealed). Calcium and copper cations diffuse in Bi-2201 layers to form Bi-2212 grains. In the literature, studies of melt-cast processing of Bi-2212 bulks reported the presence of Bi-2201 as major phase in the as-melt-cast sample and second phases as $(Sr,Ca)_{14}Cu_{24}O_x$ [116], $Bi_2Sr_3CaO_x$ [117], $SrSO_4$ [117], $CaCuO_2$ [117], $(Sr,Ca)CuO_2$ [53], Cu_2O [118] or $Bi_2(Sr,Ca)_3O_x$ [53]. More specifically, researchers at Nexans Superconductors studied in details the influence of synthesis parameters on the as-melt-cast sample during Bi-2212 bulk synthesis.

They determined from EDX measurements that the as-melt-cast sample contains Bi-2201, (Sr,Ca)CuO_2, (Ba,Sr)SO_4, $Bi_2(Sr,Ca)_3O_x$, and Cu_2O. If second phase grains are too large, the diffusion distance of Ca and Cu cations from second phase grains to Bi-2201 is too long. As a consequence, these cations cannot be consumed during the cooling stage, leaving second phases grains in the bulk material. [118] Another phenomenon that occurs during melt-cast synthesis is the persistence of Bi-2201 intergrowths layers within the Bi-2212 grains [116]. These intergrowths result from an incomplete transformation of Bi-2201 to Bi-2212 phase.

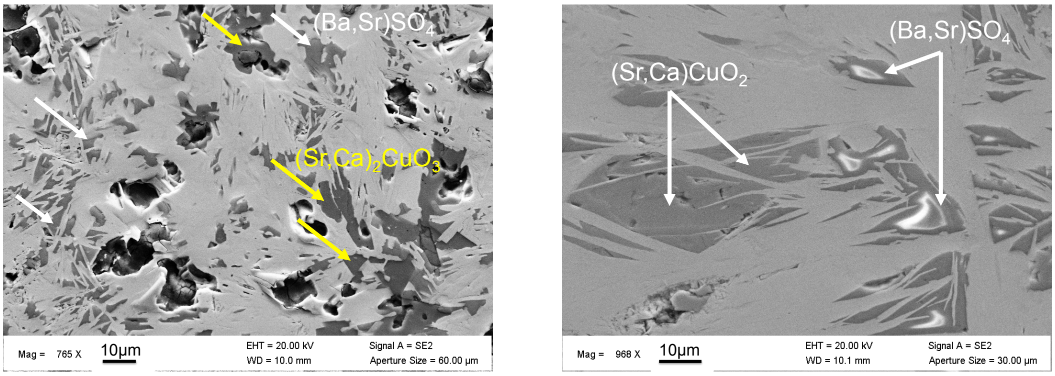

(a) (b)

Figure 3.5 – second electron SEM micrographs of a polished longitudinal cross-section of the tube close to (a) the inner edge of the tube and (b) at the center part of the tube. In Figure (a) light gray is Bi-2212 phase, mid-gray is (Ba,Sr)SO_4 phase and dark gray is $(Sr,Ca)_2CuO_3$ phase. In Figure (b) light gray is Bi-2212 phase, dark gray is (Sr,Ca)CuO_2 and dark gray grains with shiny center are (Ba,Sr)SO_4 phase.

3.2 Profile analysis using θ-2θ X-Ray diffraction data

In this section, a powder X-ray diffraction pattern collected using a classical diffractometer in Bragg-Brentano geometry is used to verify the space group and cell parameters of the crystalline phases in the sample.

3.2.1 Experimental description

A piece cut in the central part of the tube was ground manually in an agate mortar. The resulting powder was sieved on a depolished glass sample holder producing low background. The X-ray diffraction pattern was collected in θ-2θ geometry with a diffractometer D8 Advance Vario 1 from Bruker. This diffractometer is equipped with a Cu X-ray tube, a θ-2θ goniometer in Bragg-Brentano configuration (i.e. reflection geometry), a monochromator (Ge-111 type johansson to select Cu $K\alpha, 1$ radiation) and a Lynx Eye detector. Different slits are used to limit axial divergence and beam size (see Table 3.1). The configuration of the D8 diffractometer is illustrated in Figure 3.6. The Bruker program DIFFRAC.SUITE EVA and the ICDD PDF4+ database were used to identify the crystallographic phases.

Divergence slit: 0.6mm
Soller slits: 2.5°
Anti-scatter slit before sample: 0.2mm
Anti-scatter slit after sample: 8.0mm
Detector aperture: 3,0°

Table 3.1 – The diffractometer configuration used during the measurement

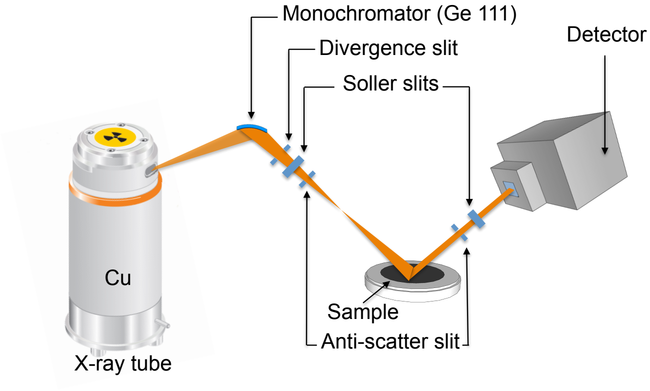

Figure 3.6 – $\theta-2\theta$ Bragg-Brentano geometry of D8 advanced Bruker diffractometer.

3.2.2 Phase identification of a tube powder

Figure 3.7 shows a θ-2θ pattern of the tube powder. The reflections of the PDF4+ reference phases (see also Table 3.2) are displayed as colored lines. The peaks with highest intensity correspond to the Bi-2212 phase. Most of the other peaks can be index as (Ba,Sr)SO_4, (Sr,Ca)CuO_2, and (Sr,Ca)$_2CuO_3$, i.e., the second phases identified with EDX. Besides, it is known from literature that Bi-2201 phase can make intergrowths with Bi-2212 phase [116, 118]. However, Bi2201 XRD reflections tend to overlap with reflections of other phases in Figure 3.7. We did not find evidence for the presence of Bi-2201 individual grains through EDX measurements but the presence of Bi-2201 intergrowth cannot be excluded at this stage.

Acronym	Cation composition (EDX)	Phases with PDF file number
Bi-2212	$Bi_{2.26}Sr_{2.25}Ca_{0.71}Cu_{1.78}O_x$	$Bi_2Sr_2CaCu_2O_{8+\delta}$ (00-041-0317)
(Ba,Sr)SO_4	$Ba_{0.13}Sr_{0.87}SOx$	$Ba_{0.13}Sr_{0.87}SO_4$ (00-039-1467)
(Sr,Ca)CuO_2	$Sr_{0.7}Ca_{0.3}CuOx$	$Sr_{0.618}Ca_{0.382}CuO_2$ (04-007-4981)
$(Sr,Ca)_2CuO_3$	$Sr_{1.6}Ca_{0.4}CuOx$	$Sr_{1.6}Ca_{0.4}CuO_3$ (00-048-1493)
Bi-2201	/	$Sr_{10}Cu_5Bi_{10}O_{29}$ (04-011-0094)

Table 3.2 – List of phases present in the tube as determined by EDX and using EVA.

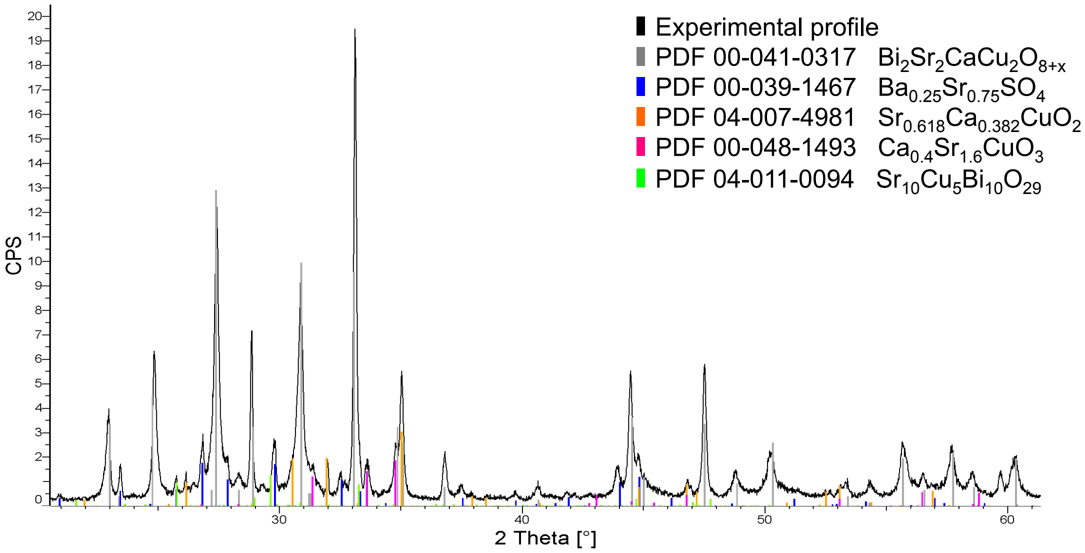

Figure 3.7 – θ-2θ pattern of tube powder showing reflections identified using Bruker's program DIFFRAC.SUITE EVA.

3.2.3 Refinement of cell parameters and phase amount determination: profile analysis

The XRD powder pattern of Figure 3.7 was refined to determine the cell parameters and percentage of each phase. Single crystal data were used as starting parameters for Bi-2212[1], (Ba,Sr)SO_4[2], (Ca,Sr)CuO_2[3], Bi-2201[4], and (Ca,Sr)$_2CuO_3$[5]. The space group and cell parameters of each phase are listed in Table 3.3. For the Rietveld refinement with the MAUD software [88], we chose a non-textured model and refined background parameters, intensity, 2θ-offset, phase volume percent, and cell parameters of each phase. The resulting pattern and the contribution of each phase are represented in Figure 3.8. The mismatch between calculated pattern and experimental pattern concerns mainly the Bi-2212 peaks and results in a goodness of fit of 2.37. During XRD sample preparation, the powder was sieved instead of pressed in order to try to decrease grain orientation effects. But the underestimation of intensity, observed on some Bi-2212 peaks, indicates that Bi-2212 platelets orientation could not be eradicated. Figure 3.9 (a) to (c) show SEM micrographs of the powder used for the measurement. Micrograph (a) shows a large distribution of particle size from a few μm to 100μm. Micrograph (b) shows a large particle of approximately 50μm length. Smaller particles are also visible around the large particle. A zoom on this large particle is shown on micrograph (c). The white arrows on the image indicate the presence of Bi-2212 platelets. The presence of such large particles with Bi-2212 platelets in the powder explains why some preferential orientation is retained after powder sieving on the depolished glass support.

Despite this residual orientation in the powder sample, a non-textured model was conserved for refinements of the XRD pattern. The refined cell parameters are reported in Table 3.4. The refined phase volume proportion are 71% of Bi-2212, 25% of (Ba,Sr)SO_4, 3% of (Ca,Sr)CuO_2, and less than 1% of Bi-2201 and (Ca,Sr)$_2CuO_3$. However these phase volume proportions should be considered with caution because of the large errors introduced by the non-textured model. Refinements suggest that Bi-2201 and (Ca,Sr)$_2CuO_3$ are actually not present (volume proportion < 1%) in the probed powder. Indeed, during the SEM characterization, grains of (Ca,Sr)$_2CuO_3$ phase were found in a small region of the tube, close to the inner edge (See section 3.1.3), while the powder studied here was obtained from the center of the tube where the presence of (Ca,Sr)$_2CuO_3$ was not evidenced by EDX.

---

[1] From Crystallographic Open Database, file # 1000285

[2] From Crystallographic Open Database, file # 9009506

[3] ICDD PDF4+ database, file # 04-007-4981

[4] ICDD PDF4+ database, file # 04-011-0094

[5] ICDD PDF4+ database, file # 04-005-5638

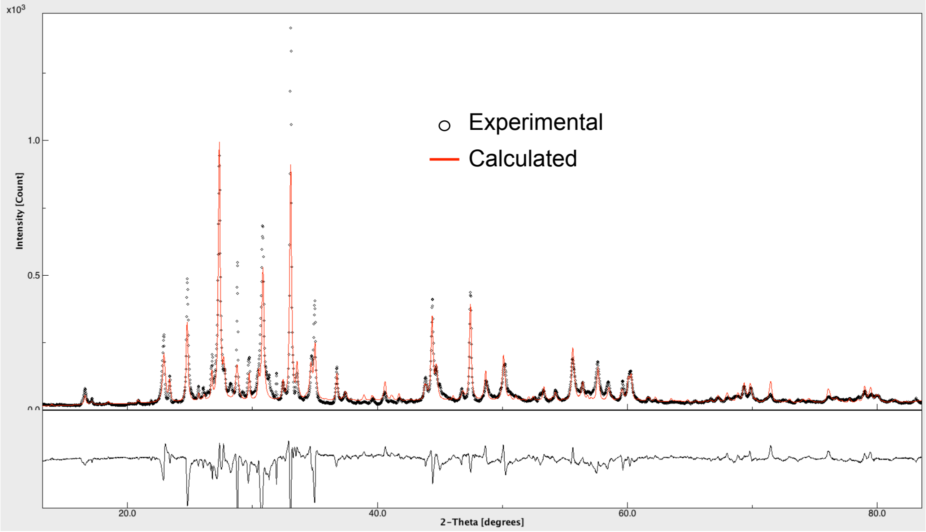

Figure 3.8 – θ-2θ pattern of tube powder with (○) experimental intensity and (—) calculated total intensity. The difference pattern at the bottom of the figure is obtained by subtraction of the experimental pattern for the calculated one.

Phase	Space group	a [Å]	b [Å]	c [Å]
Bi-2212	Amaa	5.4054	5.4016	30.7152
(Ba,Sr)SO_4	Pnma	8.408	5.372	6.897
(Sr,Ca)CuO_2	Cmcm	3.4811	16.164	3.481
Bi-2201	C121	26.8560	5.38	26.9080
$(Sr,Ca)_2CuO_3$	Immm	3.309	3.805	12.336

Table 3.3 – Space group and cell parameters of the single crystal reference data.

Phase	a [Å]	b [Å]	c [Å]	Proportion
Bi-2212	5.4120(3)	5.4143(2)	30.9870(7)	72.3(6)%
(Ba,Sr)SO_4	8.4550(6)	5.3987(4)	6.9266(5)	26.1(3)%
(Sr,Ca)CuO_2	3.4804(3)	16.219(5)	3.5063(3)	1.17(2)%
Bi-2201		Not refined		0.39(6)%
$(Sr,Ca)_2CuO_3$		Not refined		0.056(6)%

Table 3.4 – Refined cell parameters and phase proportions.

Program	**GoF**	**R$_{wp}$ [%]**	**R$_b$[%]**	**R$_{exp}$[%]**
MAUD	2.37	30.57	23.92	12.87

Table 3.5 – Reliability factors for the tube powder data refinement.

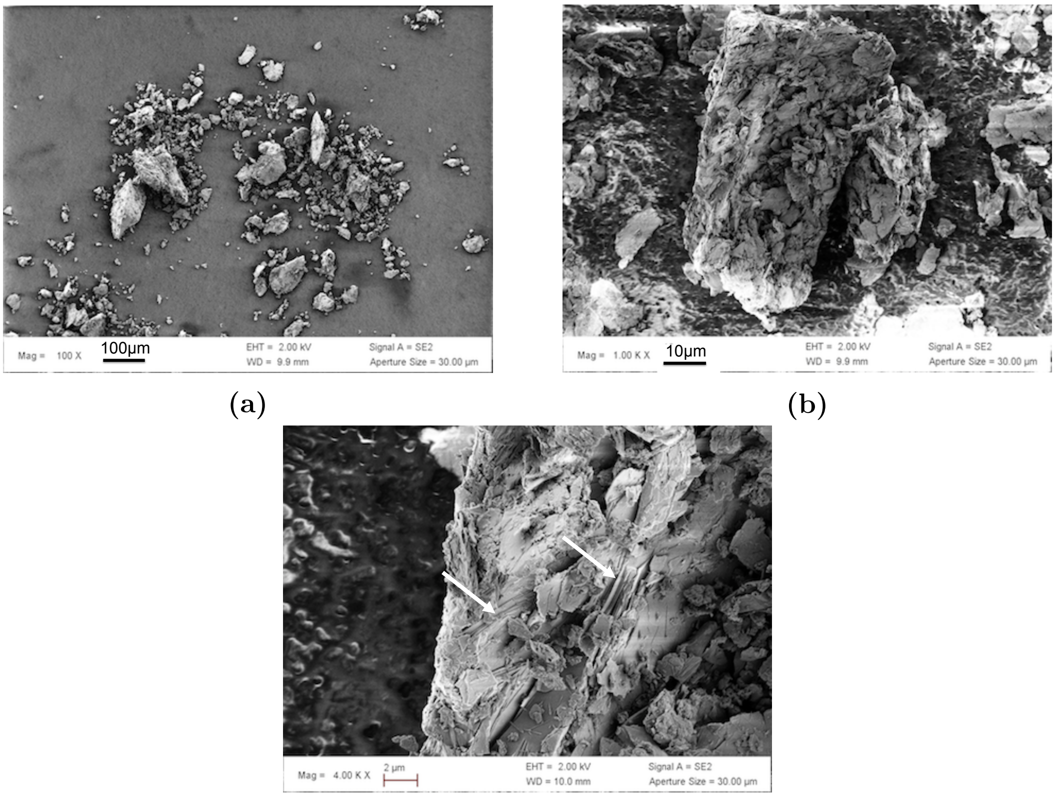

(a) **(b)**

(c)

Figure 3.9 – SEM micrographs of tube powder. Micrograph (a) shows a large distribution of particle sizes in the power. Micrograph (b) is a zoom on a region containing a particle of 50μm large. Micrograph (c) is a zoom on the big particle where platelets of Bi-2212 are visible (indicated by arrows).

3.3 Texture analysis using neutron diffraction: experimental procedure

This section is dedicated to texture characterization using the D19 and D1B neutron diffraction lines at Institut Laue Langevin (ILL) in Grenoble. The instrument description, measurement parameters and sample preparation of the tube are detailed for the D19 and D1B lines successively. The results of texture characterization using neutron diffraction data are reported and analyzed in section 3.5.

3.3.1 D19 line

D19 is a monochromatic single-crystal and fiber diffractometer performing in a wavelength range varying between 1.0 and 2.4Å. The D19 line is one of the lines closest to the reactor and receives a high neutron flux between 10^7 and 10^8 n $\text{cm}^{-2}\text{s}^{-1}$. The beam size diameter can be regulated with variable slits with a maximum diameter of 10mm. The D19 diffractometer layout is illustrated in Figure 3.10a with the sample mounted at the center of an Eulerian cradle (Figure 3.10b). The Eulerian cradle can be rotated according to three rotation axes omega (ω), chi (χ), and phi (φ) where ω is the rotation angle of the Eulerian cradle around the vertical axis, χ is the rotation angle of the sample around the normal to the cradle plane, and φ is the rotation angle of the sample around its normal. Figure 3.10c shows the D19 large (120° x 30°) 2D position-sensitive detector (PSD) allowing a simultaneous measurement of 120° in 2θ and 30° in χ for a single sample χ position. A 90° range in χ is then spanned with only 4 χ sample positions. Compared to a 1D PSD detector, the time needed for a complete experiment is highly reduced.

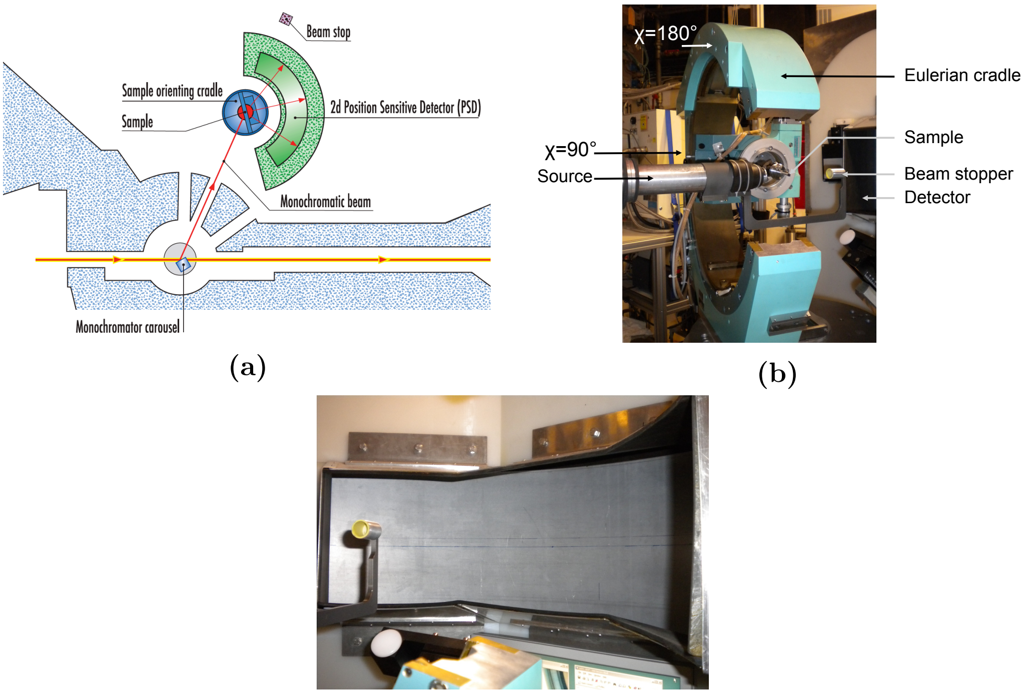

(a)

(b)

(c)

Figure 3.10 – Illustration of (a) D19 line layout with its (b) Eulerian cradle and (c) 2D PSD detector.

The choice of the Eulerian cradle ω angle depends on the fact that only the pole figure located at 2 ω =2 θ is measured completely. All the other pole figures exhibit a blind area in their centers due to localization corrections [95]. Therefore an ω value so that 2ω is around the range of 2θ where the main peaks are located satisfies the measurement of maximum information in pole figures. We chose to fix 2ω=2θ=21.8° (ω =10.9°) corresponding to the position of the (008) reflection of the Bi-2212 phase. Samples were rotated in χ and φ to cover ranges of 90° in χ and 360° in φ:

$$\begin{cases} \chi = 95°, 120°, 145°, 170° \\ -175° \leq \varphi \leq 175° \text{ by } 10° \\ \omega = 10.9° \end{cases}$$

Data at each (χ,φ) position were acquired to reach 500000 incident neutrons at a wavelength of 1.4510 Å.

3.3.1.1 Sample preparation for D19

Samples for neutron diffraction should be as spherical as possible to avoid volume and absorption corrections, never perfectly controlled due to geometrical imperfections. The tube radial thickness is 7 millimeters. We decided to compare the textures in the inner (I), center (C) and outer (O) parts of the tube, cut through its thickness. To do this, two cylinders of 12mm diameter (smallest drill available) were extracted from the tube (stage 1 in Figure 3.11). The diameter of these cylinders was too large for D19 measurements because their diameter exceeds the maximal beam size of 10mm diameter. Therefore they were cut to a rectangular parallelepiped shape with dimensions of 6x6x7mm^3 as illustrated on stage 2 in Figure 3.11. The outer edge of the parallelepipeds was removed to get rid of the silver coating covering the tube. Two samples of 2mm thickness were then cut from each parallelepiped: either inner (I) + center (C) or center + outer (O) (see stage 3 in Figure 3.11). A particular attention was taken for the cut of the center part that was extracted out of the non porous region of the sample as illustrated in Figure 3.4. Finally, the edges of the samples were slightly polished to avoid sharp edges and try as much as possible to make them isotropic. Neutrons are largely penetrating our samples and we do not expect intensity variations with (χ, φ, ω) rotations with such small samples.

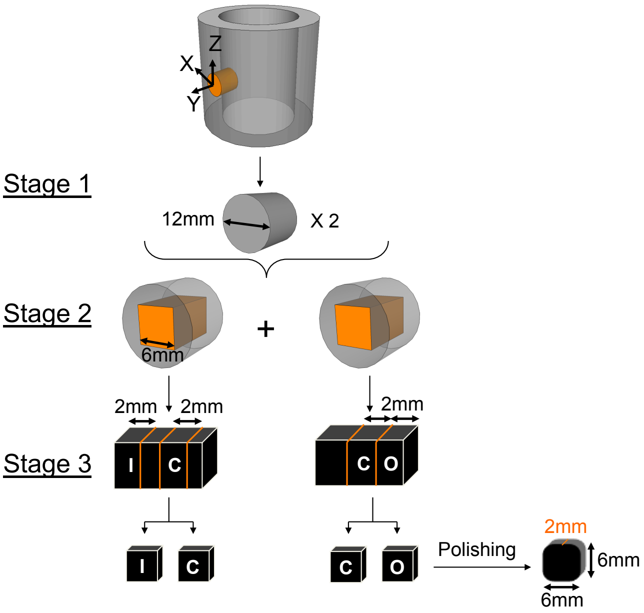

Figure 3.11 – Procedure of tube sample preparation for D19 measurements. At stage 1, two cylinders of 12mm diameter are extracted from the bulk tube. At stage 2, these cylinders are reduced to a parallelepiped shape. At stage 3, the first parallelepiped is cut in 3 pieces: inner (2mm), center (2mm), and trashes. The second parallelepiped was cut in 3 pieces: trashes, center (2mm), and outer (2mm). Only the 2mm thick samples were kept for neutron measurements.

The reference frame of the cylindrical pieces is illustrated in Figure 3.12a with axis Z defined along the tube axis and axis Y defined along tube radius. Samples were mounted on the Eulerian cradle using a sample holder as the one shown in Figure 3.12b. Experimental mounting of the sample is illustrated in Figure 3.12c with the sample (orange) at the center of the Eulerian cradle. The sample is oriented with axis Y along the sample holder (parallel to the φ axis) and axis Z parallel to the χ axis at φ=0. Note that the same sample mounting was used for the D1B and Inel experiments discussed later.

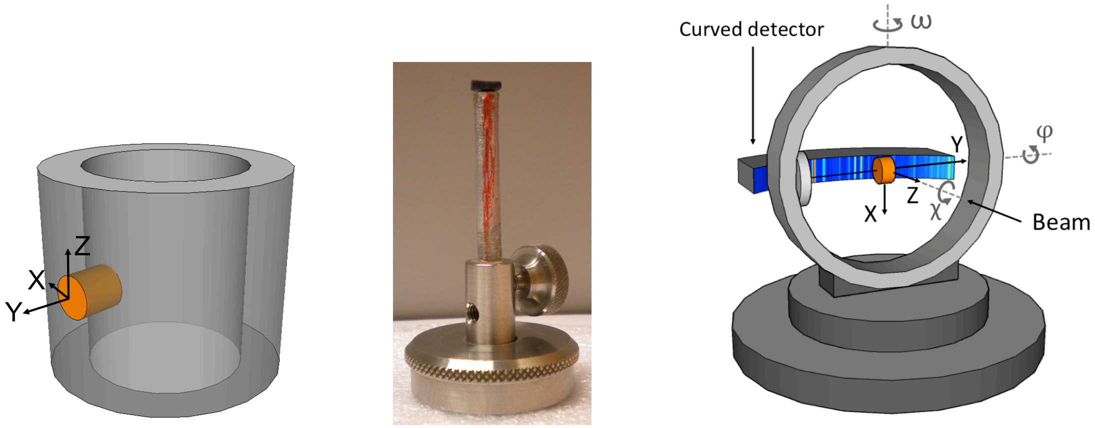

(a) (b) (c)

Figure 3.12 – (a) Illustration of the reference frame of cylindrical samples extracted from the tube. Z axis is along tube axis and Y axis is along tube radius. (b) Sample holder used for mounting samples at D19 and D1B lines. (c) Experimental mounting on D19, D1B and Inel diffractometers with the sample (orange) at the center of the Eulerian cradle. The sample is oriented with axis Y along the sample holder and axis Z parallel to the χ axis at φ=0.

3.3.2 D1B line

D1B is a high intensity powder diffractometer performing at a wavelength of 2.52Å (pyrolytic graphite monochromator), used for the present work, or 1.28Å (germanium crystal monochromator) with respective fluxes of 6.5x10^6 or 0.4x10^6n.cm^{-2}.s^{-1} at the sample position. The D1B diffractometer layout is illustrated in Figure 3.13 with its steady ^{3}He/Xe position-sensitive detector composed of a system of multi-electrodes with 1280 cells. The detector covers an angular range of 0.8° to 128.8° in 2θ and allows measurement at one (χ, φ) position at a time. Samples are mounted on an Eulerian cradle and can be rotated according to ω, χ, and φ angles (Figure 3.12c). The beam size can be regulated with variable slits with a maximum size of 5x2cm^2, which we adjusted to our sample sizes to optimize peak-to-background ratio.

D1B has a closed Eulerian cradle that intercepts the beam if the ω angle is not adequately chosen. ω angle was fixed at 44.95° , an angle larger than for D19 or the INEL diffractometer. Samples were rotated in χ and φ to cover ranges of 90° in χ and 360° in φ:

$$\begin{cases} 0^\circ \leq \chi \leq 90^\circ \text{ by } 5^\circ \\ 5^\circ \leq \varphi \leq 360^\circ \text{ by } 5^\circ \\ \omega = 44.95^\circ \end{cases}$$

Data at each (χ, φ) position were acquired during 30 seconds.

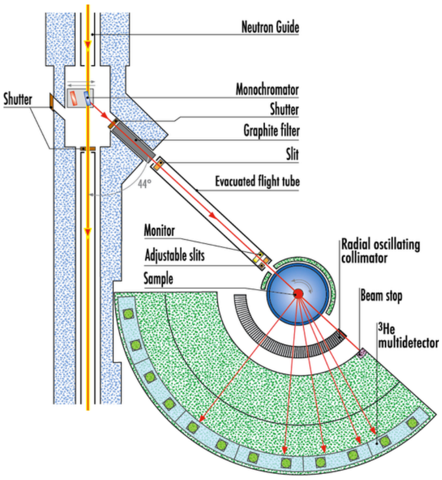

Figure 3.13 – D1B instrument layout.

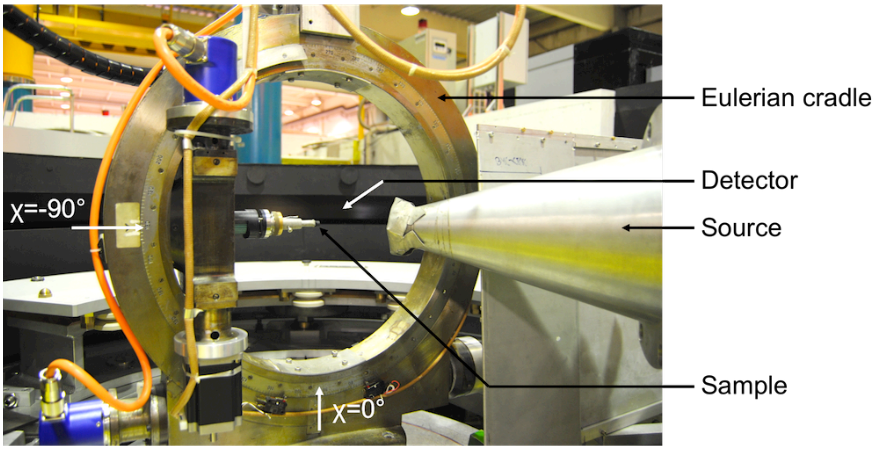

Figure 3.14 – D1B instrument geometry when χ=-90°.

3.3.2.1 Sample preparation for D1B

D1B sample preparation is similar to D19 sample preparation. The main difference to consider is the larger D1B beam size allowing the measurement of larger samples than for the D19 line. As for D19 sample preparation, a cylinder was extracted from the tube along the thickness of the tube (3.15a). The cylinder was then cut in three parts (3.15b) and contrarily to D19 sample preparation, samples kept their cylindrical form. Only the center sample was considered for measurements and was mounted on a Eulerian cradle the same way as for D19 instrument (Figure 3.12c)

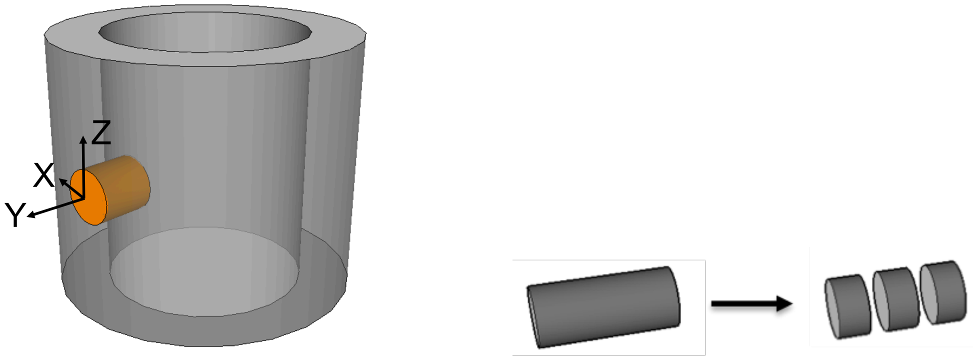

(a) (b)

Figure 3.15 – Illustration of (a) the sample extracted from the tube sample for D1B measurement and (b) the 3 parts (inner, center, and outer) cut along Y in the sample.

3.4 Quantitative texture analysis using 4-circle diffractometer: experimental procedure

This section describes the INEL X-ray 4-circle diffractometer, the instrumental parameters and the mounting of the sample.

3.4.1 Experimental description of Inel diffractometer

Texture measurements were carried out on the 4-circle INEL diffractometer (Figure 3.16) at CRISMAT laboratory. Samples were analyzed in reflection with a monochromatized Cu-K$\overline{\alpha}$ radiation. The INEL CPS 120 curved detector allows simultaneous measurement of 120° in 2θ. Both the X-ray tube and the detector are fixed for our experiment. The instrument collimator is equipped with 2x2 Huber crossed slits. In order to keep the beam imprint on the sample, sample size should not be smaller than 5mm x 5mm and χ should not be too large (here $\leq 55°$). [119] During the experiment, the incident X-ray beam angle was tilted at ω=15° and patterns were recorded using a regular grid of 5°x5° in χ and φ with $0° \leq \chi \leq 55°$ and $0° \leq \varphi \leq 355°$. Exposure time for each pattern was 180 seconds. The 5°x5° grid in χ and φ implies that 864 patterns were collected for each experiment:

$$\begin{cases} 0° \ \leq \chi \leq 55° \ \text{ by } 5° \\ 0° \ \leq \phi \leq 355° \ \text{ by } 5° \\ \omega = 15° \end{cases}$$

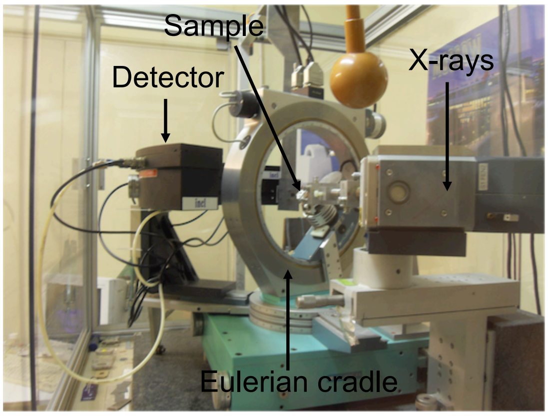

Figure 3.16 – Inel diffractometer at CRISMAT laboratory.

3.4.2 Sample preparation for Inel experiment

Samples used for Inel measurements were the same as for D19 and D1B experiments. They were mounted on the Eulerian cradle the same way as for D19 (See section 3.3.1.1).

3.5 Comparison and interpretation of measurements done on D8, Inel, D1B, and D19

This section contains the results of texture characterization from the X-ray and neutron experiments described respectively in Sections 3.3 and 3.4 on samples extracted from the center part of the tube. After presenting the experimental patterns obtained from each technique, these patterns are compared in terms of resolution, phase content and crystallographic parameters. Then the texture results are presented by way of pole figures, followed by an analysis of these results.

3.5.1 Comparison of experimental patterns

For all techniques, the collected data were imported in MAUD software [88]. A Rietveld refinement was performed on each set of data with the Bi-2212 and (Ba,Sr)SO_4 phases since they are the major phases. When possible, the (Ca,Sr)CuO_2 phase was also taken into account in the refinement. For the refinement of the Orientation Distribution of crystallites (OD), we selected the E-WIMV model and refined background parameters, intensity, 2θ offset, phase volume fractions, and cell parameters of each phase. Figure 3.17 shows three Intensity versus 2θ plots corresponding respectively to the sum of all patterns acquired in (χ, φ) on D19, D1B, and Inel. The previously discussed $\theta - 2\theta$ powder pattern acquired on D8 instrument is reproduced at the bottom of the figure. To make comparison easier, all patterns are plotted for Cu wavelength (i.e. λ_{Inel}=1.5406 Å). There are three principal observations arising from these plots, concerning: (i) the 2θ measurement range, (ii) the intensity of the peaks, and (iii) the peaks width.

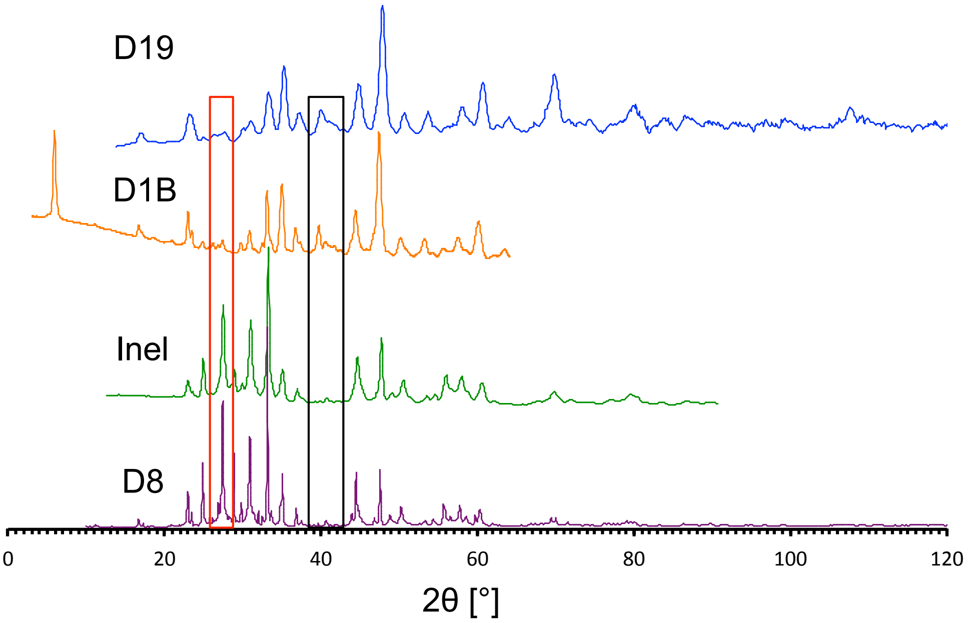

Figure 3.17 – Intensity-2θ patterns resulting of the sum of the patterns collected at all (χ, φ) positions on (-) D19, (-) D1B, (-) Inel, and (-) θ-2θ powder pattern acquired on D8 diffractometer for the tube sample. All data are plotted for Cu K_α wavelength for easier comparison. The rectangles highlight two regions were peak intensities differ considerably between X-ray and neutron experiments.

The first observation is that the 2θ range of acquisition varies from one instrument to the other resulting from the difference in wavelength and detector size. Inel, D1B, and D19 instruments possess a curved PSD detector that allows simultaneous measurement on a wide range of 2θ angles. Contrarily to other instruments, the D8 diffractometer possesses a small 1D detector and the measurement was done in a Bragg-Brentano geometry.

The second observation concerns the large difference of intensity for some peaks. As examples, two angular ranges are highlighted with red and black rectangles in Figure 3.17. The red rectangle evidences a peak with a high intensity in X-ray patterns and small intensity in neutron patterns. The black rectangle shows the inverse situation. In both cases, the peaks correspond to (Ba,Sr)SO_4 reflections. As explained in Section 2.2.1, X-ray and neutrons do not interact the same way with the atoms. X-rays are scattered by the electronic cloud of atoms and as consequence, the Ba atom in the (Ba,Sr)SO_4 phase will scatter much more than the other atoms that are lighter. These differences in scattering may explain the differences in diffracted intensities.

The last observation made from this figure concerns the instrumental resolution and the peak width. Compared with Inel and even more with D8 peaks, D1B and D19 peaks are broader and some small reflexions are overlapped with peaks having higher intensity. Figure 3.18 shows the instrumental functions for all diffractometers used to acquire data during this thesis[1]. The D8 instrument has the best instrumental resolution manifested by peaks having the smallest FWHM. The FWHM function is θ dependent and increases with 2θ angle. For the D8 instrument, the increase is less than 0.1° from 0° to 120° in 2θ. Inel and neutron instruments have large FWHM even at 2θ=0°. D19 and D1B instruments have the largest FWHM with a value of 1° for 2θ=83° and up to 2° for 2θ~120°. These values are large and explain why some parameters cannot be refined from neutron data due to a lack of resolution. For example, anisotropic crystallite size cannot always be refined using neutron data. Even if the resolution of Inel diffractometer is better, it was not possible to refine parameters such as atomic positions or atomic site occupations. However, the Inel instrumental resolution was sufficient to resolve peaks arising from the (Ca,Sr)CuO_2 phase and allows to introduce this phase in the refinement. In the case of D19, the large size of the dataset does not allow the refinement of more than two phases. The neutron datasets (D19 and D1B) were refined with only the two main phases, i.e. Bi-2212 and (Ba,Sr)SO_4.

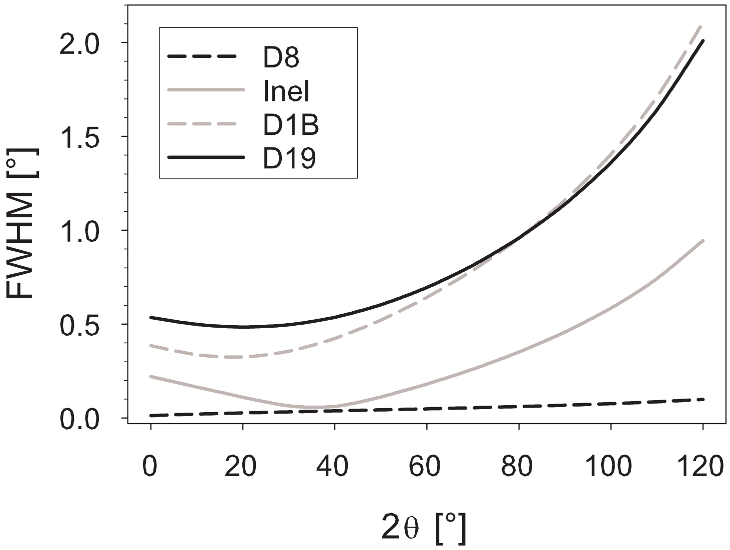

Figure 3.18 – Evolution of the instrumental function with 2θ for the different instruments.

---

[1] Full Width at Half Maximum: $FWHM^2 = H_k^2 = Utan^2\theta + Vtan\theta + W$ See Section 2.2.3.2 for more details

Figure 3.19 (a), (b), and (c) are Intensity versus 2θ plots representing the sum of all patterns acquired in (χ, φ) on Inel, D1B, and D19 respectively. The D8 pattern is not represented here as it is not considered for texture characterization. The difference in 2θ scale between all patterns of Figure 3.19 arises from the difference in wavelength: λ_{D1B}= 2.5249 Å, λ_{D19}=1.4510 Å, and λ_{Inel}=1.5406 Å. The sum diagrams in principle should be close to a powder pattern, since the diagrams are measured at many orientations. This is less true for X-rays since defocussing phenomena impose to limit the measured χ-range to 55°. Examples of individual (χ, φ) scans are represented for D1B data on the tube in Figure 3.20. The fact that the sample is textured is clearly visible as diffracted intensities vary with (χ, φ).

Visual inspection of figure 3.19 shows that the calculated patterns fit rather well with the experimental patterns, considering that the parameters related to the cationic ratios were not refined. The best agreement is observed for the D1B data, as confirmed by the reliability factors in Table 3.10. In the case of the Inel data, there seems to be some problems regarding the anisotropic broadening, despite the use of the POPA anisotropic model (see section 2.2.3.2). In the case of D19 data, the refinement of the texture model was hindered by the huge size of the dataset (see next section) and the 2θ range above 75° is not very useful because of the poor signal to noise ratio. Refined cell parameters and phase percentages for the Inel, D1B, and D19 datasets are presented respectively in the Tables 3.6, 3.7, and 3.8. The corresponding results for the pattern collected on D8 can be found in Table 3.9, which is a copy of a table presented in section 3.2.3. Comparison of the tables shows that the cell parameters refined from Inel and neutron diffraction data differ significantly from the input model. Because of the best resolution of D8, the cell parameters refined on D8 can be considered as more reliable.

On the contrary, the phase content refined from the D8 data are likely to suffer from a significant error because texture was not taken into account. All techniques give a Bi-2212 phase volume proportion between 77% (Inel) and 82% (D1B).

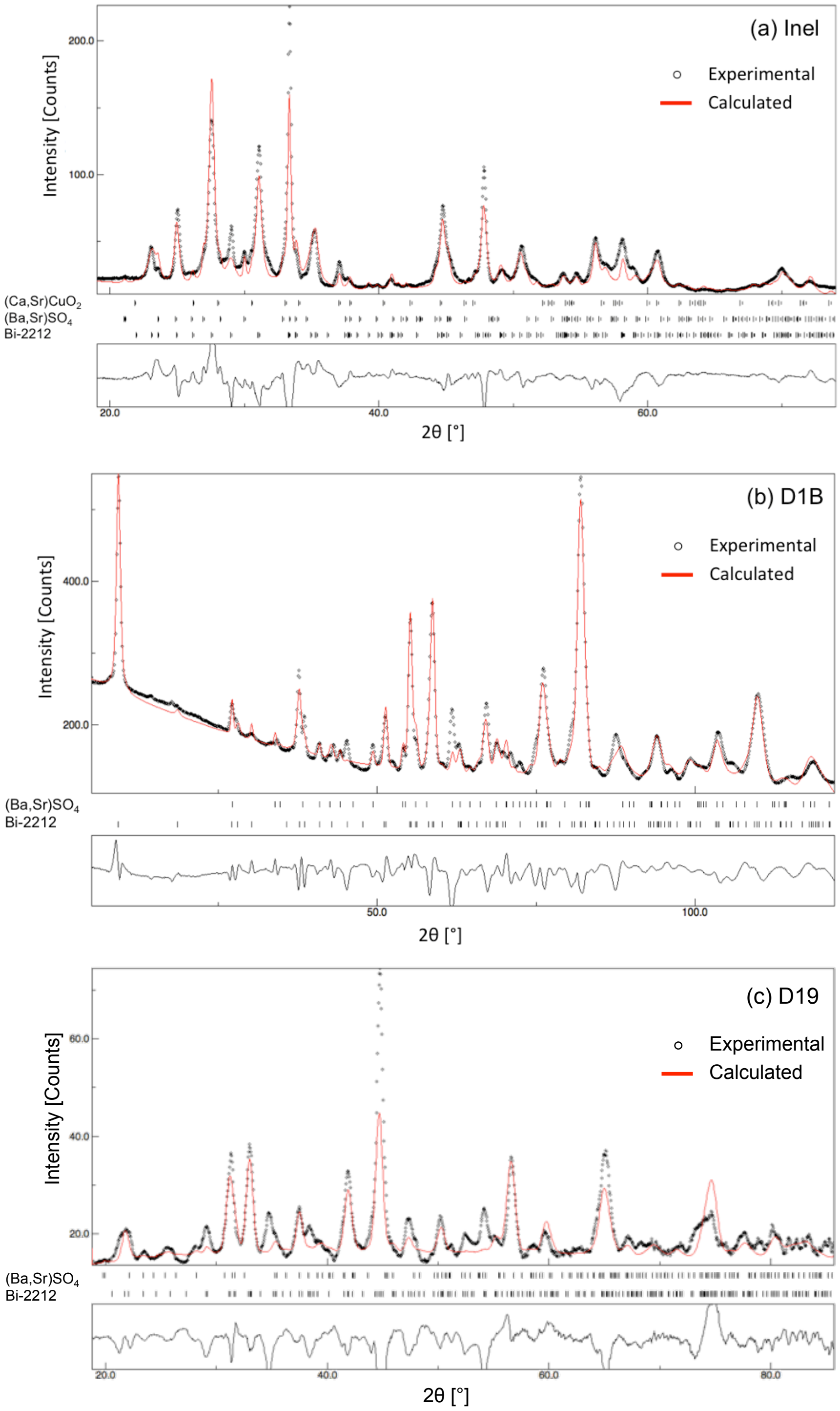

Figure 3.19 – 2θ patterns resulting from the sum of patterns acquired at all (χ, φ) positions on (a) Inel, (b) D1B, and (c) D19 diffractometer for the tube sample. (**--**) Experimental intensity, (**--**) calculated total intensity from phases Bi-2212 and (Ba,Sr)SO4.

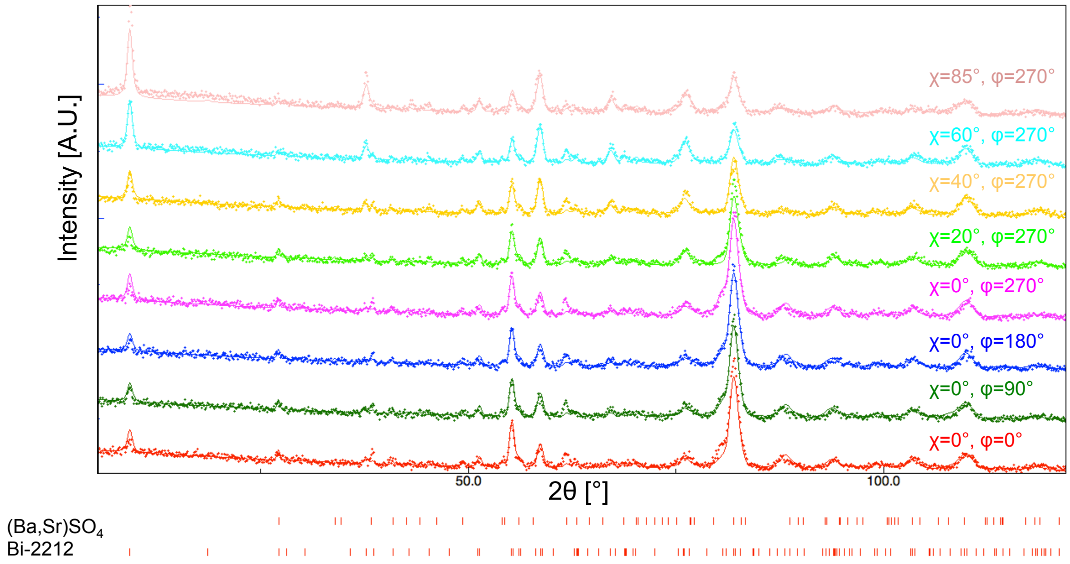

Figure 3.20 – Experimental patterns acquired on D1B instrument and showing the variation of diffracted intensities for some (χ, φ) angles.

Phase	a [Å]	b [Å]	c [Å]	Vol %
Bi-2212	5.4028(1)	5.38743(9)	30.8668(5)	77.2(5)%
(Ba,Sr)SO$_4$	8.3918(5)	5.3764(4)	6.8945(4)	17.59(7)%
(Ca,Sr)CuO$_2$	3.4439(3)	16.622(1)	3.5317(3)	5.14(4)%

Table 3.6 – Results of refinement on tube bulk from Inel data.

Phase	a [Å]	b [Å]	c [Å]	Vol %
Bi-2212	5.43722(8)	5.45450(8)	31.2118(3)	82%
(Ba,Sr)SO$_4$	8.4583(4)	5.5240(3)	6.9552(4)	17%

Table 3.7 – Results of refinement on tube bulk from D1B data.

Phase	a [Å]	b [Å]	c [Å]	Vol %
Bi-2212	5.385(5)	5.420(3)	30.834(1)	80(1)%
(Ba,Sr)SO$_4$	8.50(1)	5.42(1)	6.91(1)	20(2)%

Table 3.8 – Results of refinement on center part of the tube from D19 data.

Phase	a [Å]	b [Å]	c [Å]	Proportion
Bi-2212	5.4120(3)	5.4143(2)	30.9870(7)	72.3(6)%
(Ba,Sr)SO_4	8.4550(6)	5.3987(4)	6.9266(5)	26.1(3)%
(Sr,Ca)CuO_2	3.4804(3)	16.219(5)	3.5063(3)	1.17(2)%
Bi-2201		Not refined		0.39(6)%
(Sr,Ca)$_2$CuO$_3$		Not refined		0.056(6)%

Table 3.9 – Results of refinement on tube powder from D8 data.

Instrument	GoF	R_{wp}
D8	2.37	30.57%
Inel	1.26	31.13%
D1B	1.47	10.98%
D19	0.93	21.46%

Table 3.10 – Reliability factors of refinements.

3.5.2 Comparison of textures

As mentioned in the previous section, texture was refined using the E-WIMV formalism. This aspect of the refinement is discussed here in more details. The orientation distributions were refined with a 5°x5°x5° grid for the Inel and D1B data. In the case of the huge D19 datasets, calculation often stopped due to a lack of computer memory. Therefore we decided to import only one half of the D19 data (one scan over two) in order to reduce the size of the dataset. This decision implies that the ODF was refined using a E-WIMV grid of 10°x10°x10°.

Figure 3.21, Figure 3.22, and Figure 3.23 show a two-dimensional representation of calculated (upper part) and experimental (bottom part) datasets from Inel, D1B, and D19 instruments respectively. They are constructed by stacking up all diagrams from (χ_i, φ_i) to (χ_i, φ_n), to (χ_n, φ_n), where χ_i, φ_i are the initial χ and φ values and χ_n and φ_n are the highest χ and φ values. The appearance of the plot for D19 data is different from the D1B and Inel data, because of the 2D detector of D19[1]. A variation of diffracted intensities along (χ, φ) is visible on every two-dimensional representation of datasets, indicating the presence of texture in the sample. These

---

[1] In fact, for a given vertical extent of the D19 detector of 30°, the pole figure spanning in ϑ_y varies with 2θ, because of localization corrections. This creates larger ϑ_y around 2θ=20° in our measurements.

variations are mostly visible for the Bi-2212 reflections. The D1B calculated data fit well with experimental data. In the case of the Inel data, there is an inversion of the intensity ratio of the peaks at ~27° and at ~33° with respect to the experimental data, as also observed in the sum pattern shown in the previous section. In the case of the D19 experiment, the grid of 10° resolution is not good enough to describe the sharpest texture components; if the computing problem can be solved in the future, a OD refinement with a grid of 5° resolution should be performed.

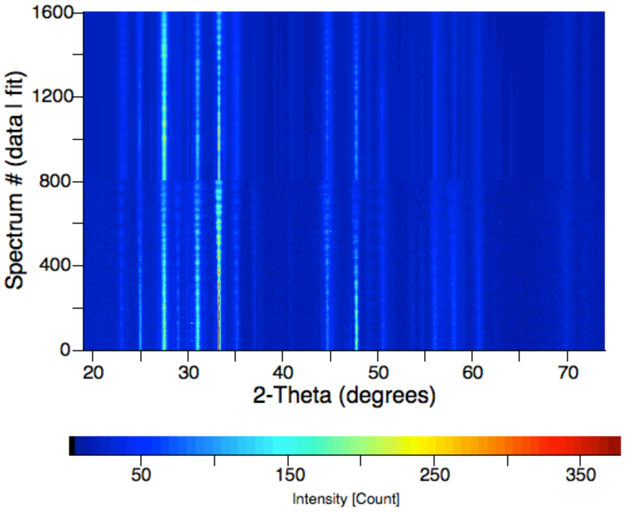

Figure 3.21 – 2D representation of the simulated (top) and experimental (bottom) datasets from Inel diffractometer. (χ, φ) patterns are stacked up from (0°, 0°) to (0°, 355°), to (55°, 355°) (from bottom to top).

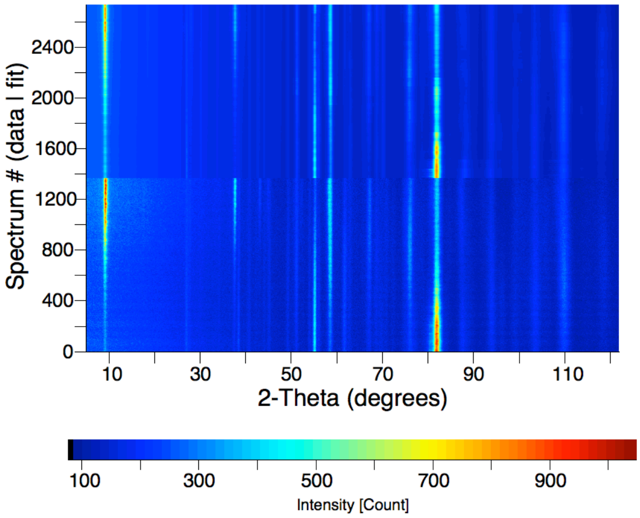

Figure 3.22 – 2D representation of the simulated (top) and experimental (bottom) datasets from D1B diffractometer. (χ, φ) patterns are stacked up from (0°, 0°) to (0°, 355°), to (90°, 355°) (from bottom to top).

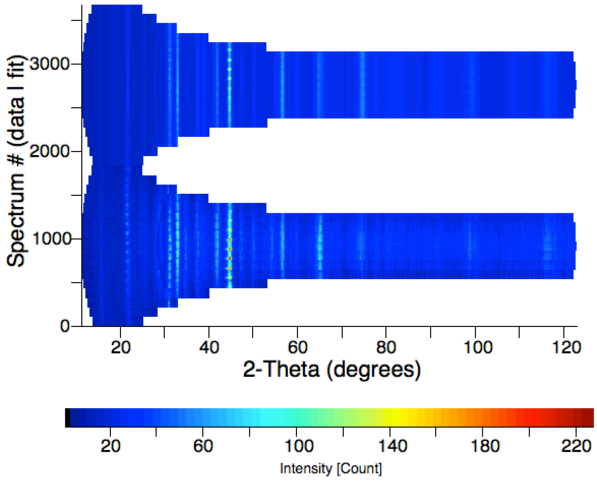

Figure 3.23 – 2D representation of the simulated (top) and experimental (bottom) datasets from D19 diffractometer. (χ, φ) patterns are stacked up for each η value (from -40° to 40° by 5°) from (10°, -175°) to (10°, 175°), to (80°, 175°) (from bottom to top).

Figure 3.24 shows normalized pole figures calculated from the orientation distribution refinement of the Bi-2212 phase measured on the D1B instrument. {200}, {020}, and {00$\underline{10}$} pole figures (PF) correspond to planes for which the normal is aligned with the main crystallographic axes **a**, **b**, and **c**, respectively. The first conclusion to draw from these pole figures is that the maxima of orientation density are weak, below 10 m.r.d.. This confirms the conclusions drawn at Nexans Superconductors based on the analysis of $\theta - 2\theta$ patterns collected with a laboratory Bragg-Brentano diffractometer at fixed χ_i (See Section 3.6). In the following, we try to go further in the analysis of texture by identifying texture components in the pole figures. The {00$\underline{10}$} PF exhibits a maximum of orientation density around 7 m.r.d. located at the center of the PF with a sharp distribution of *c*-axes around the Y axis of the tube. This type of texture is called a <001>-fiber texture. When the maximum of the density scale is reduced to 2 m.r.d. ({00$\underline{10}$} PF at the bottom of Figure 3.24), a reinforcement on the equator of the PF is revealed, corresponding to a texture component with the *c*-axes distributed at random in the sample plane XOZ. There is also an equatorial reinforcement in the {200} PF. These two components are compatible with the 7 m.r.d. fiber texture at the center of the {020} PF (<010>-fiber texture). In order to compare the two texture components in the {00$\underline{10}$} PF, it should be noted that the fiber component (sharp orientation peak in the center of {00$\underline{10}$} PF) corresponds to small measured solid angles, i.e., small orientation volumes. On the contrary, the equatorial reinforcement in the {00$\underline{10}$} pole figure corresponds to larger orientation volumes. The principal texture component is thus the <010>-fiber texture with *c*-axes oriented in the XOZ plane of the tube. This texture component is schematically drawn in Figure 3.25b, the reference frame XYZ being the one of the tube.

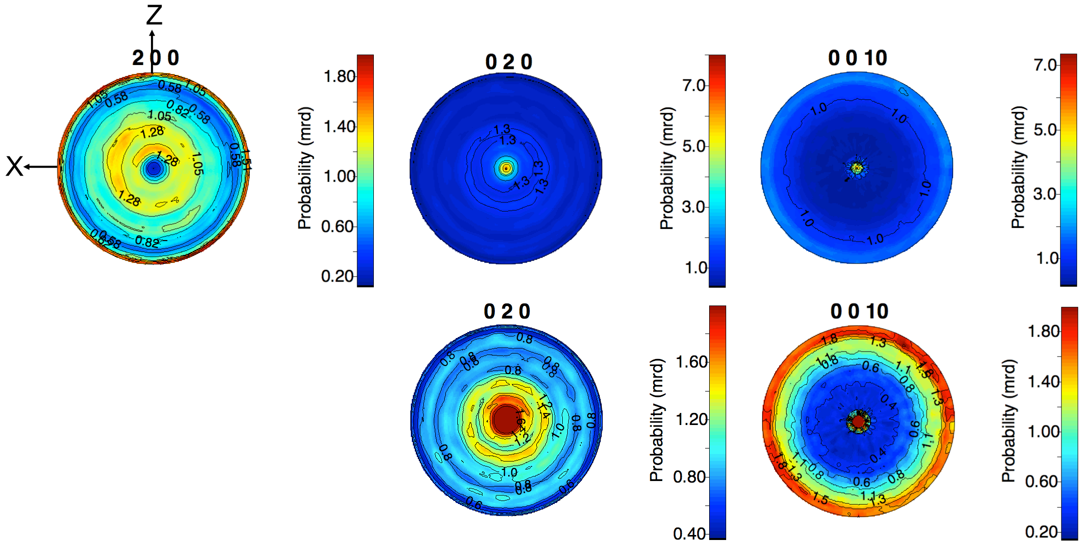

Figure 3.24 – {200}, {020}, and {00<u>10</u>} normalized pole figures calculated from data acquired on D1B instrument for Bi-2212 phase in the tube sample.

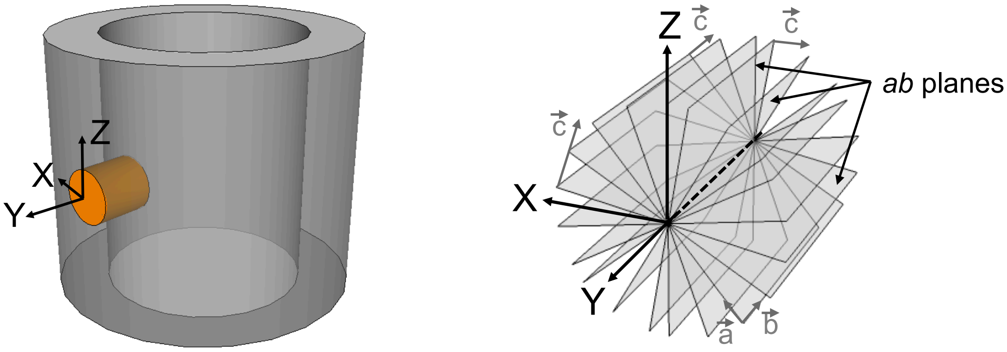

(a) **(b)**

Figure 3.25 – Illustration of (a) the tube reference frame and (b) the main texture component in the tube, with a distribution of *c*-axes in the XOZ plane.

As a complement to pole figures, representing the orientation distribution is useful to give a complete view of the texture and confirm that no texture component has been missed. Figure 3.26 illustrates the 3-dimensional orientation distribution of Bi-2212 phase calculated from D1B data. This OD is represented as a function of the α, β, γ Euler angles. Each rectangle in this figure is a β-section corresponding to a 180°x180° map in (α, γ). The use of OD as a representation of texture is detailed in section 2.1.3.2. The following discussion is based on a different orientation of the X,Y,Z reference axes (here Z = radial direction; Y = tube axis) by comparison with the pole figures. In this particular OD the major texture component is visible in the β=5° cell (2^{nd} cell). The variation of intensity in α is lower than in γ. This observation is true for all β cells. In this situation the crystallite reference frame K_c is assimilated to the orthorhombic reference frame so that $K_c=\{\mathbf{a}, \mathbf{b}, \mathbf{c}\}$. The β=5° cell corresponds to a situation where **c** is at 5° from the radial direction of the tube. The reinforcements in the β=5° cell are observed for values of γ around 20° and 160° and for α values varying from 0° to 180°. In other words, the texture component related to this particular cell is a fiber component with *c*-axes oriented close to the radial direction of the tube with a sharp distribution. In the reference framework used for the pole figures, it corresponds to the <001>-fiber texture observed in the $\{00\underline{10}\}$ pole figure. As this texture component is 5 times more intense (in m.r.d) than the <001>-fiber texture associated to the equatorial reinforcement of the $\{00\underline{10}\}$ pole figure, this is the only one visible in the ODF at the scale used for the plot.

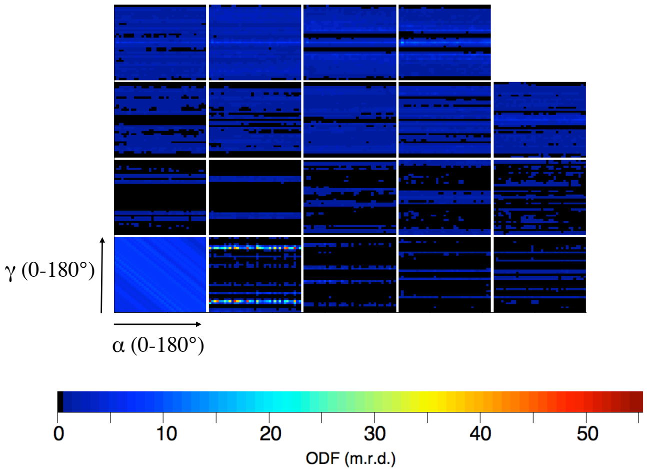

Figure 3.26 – Two dimension β-sections representing the orientation distribution of the Bi-2212 phase calculated from D1B data on the tube. OD is divided in cells every 5° in β (from bottom left to top right). Each cell of the OD is a 180°x180° grid in (α, γ).

Figure 3.27 shows the normalized pole figures calculated from OD refinements of the Bi-2212 phase measured on the Inel instrument. Contrary to D1B, the surface probed with Inel is only typically 10μm deep in such material. The three PFs exhibit small values of orientation density. The observed trends are in general agreement with the D1B results but the maximum of orientation density at the center of the $\{00\underline{10}\}$ PF is only ~1.7 m.r.d.. As for D1B, the {200} and {020} PFs exhibit small values of orientation density with maxima located respectively near the equator of the pole figure and around the center of the pole figures.

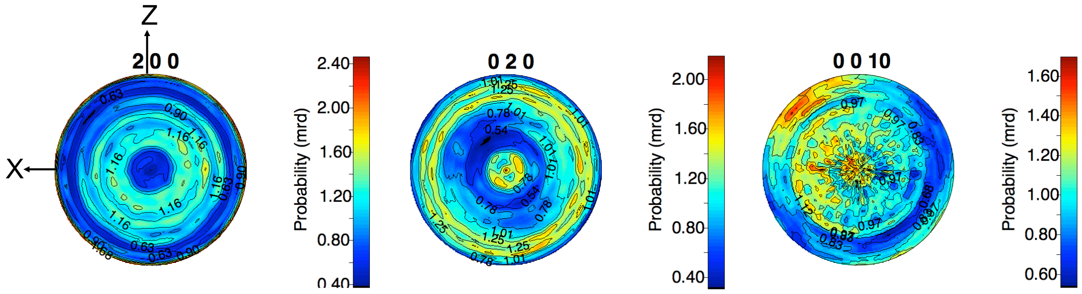

Figure 3.27 – {200}, {020}, and $\{00\underline{10}\}$ normalized pole figures calculated from data acquired on Inel instrument for Bi-2212 phase in tube sample.

Figure 3.28 shows the normalized pole figures calculated from OD refinement of Bi-2212 phase from data measured on D19 instrument. The details of the texture components described hereafter might be modified if the quality of the refinement can be improved by using a 5°x5°x5° to take better account of the sharpest texture components. The $\{00\underline{10}\}$ pole figure exhibits a maximum of orientation density of 1.35 m.r.d. located on the equator of the pole figure. The major texture component is with *c*-axes distributed at random in the sample plane XOZ. The {200} and {020} pole figures exhibit a maximum of OD of 1.17 m.r.d. localized nearly in the center of the pole figure indicating that *a*-axes and *b*-axes are distributed at random around *c*-axes and reveal a major planar-like texture, with *c*-axes at random in XOZ plane. This component was also visible in the D1B experiment, however allied with other components. Since the sample probed with D19 is smaller than the D1B sample and more concentrated at the center of the tube wall, we conclude the planar component is occurring in this area.

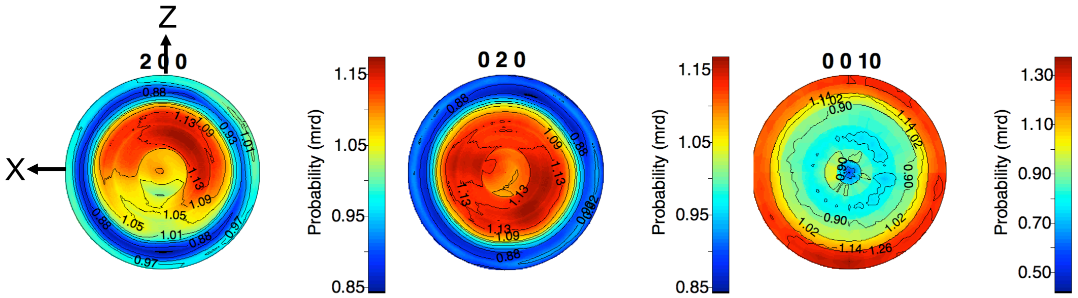

Figure 3.28 – {200}, {020}, and {00$\underline{10}$} normalized pole figures calculated from data acquired on D19 instrument for Bi-2212 phase in tube sample.

In conclusion, pole figures calculated from data acquired on Inel, D1B, and D19 instruments exhibit small maxima of orientation distribution, not larger than 10 m.r.d., meaning that the tube is slightly textured. The D1B pole figures revealed the existence of 2 major texture components: a <001>-fiber texture, and a <010>-fiber texture with *c*-axes oriented in the XOZ plane. <010>-fiber texture is the principal component of texture and is in majority found in the center region along the tube thickness. We observe different results from the texture point of view when using the three different instruments. These differences are associated to the differently probed volumes, and allow some discrimination between the respective textures.

3.5.3 Physical properties of the tube along X,Y,Z directions

As described in the introduction (See Section 1.2.1.2), physical properties of the Bi-2212 phase differ between the **c** direction and along *ab* planes. Therefore an important question is whether the existence of the relatively weak texture components detected in the previous section results in an anisotropy of the physical properties of the tube. In order to investigate this point, electrical resistivity vs. temperature and magnetization vs. magnetic field curves have been measured along the three directions X, Y, Z. Electrical resistivity was measured on small bars of 1x1x7mm^3 cut along X, Y, Z as illustrated in Figure 3.29. The measurements were carried out with the usual four-probe technique in a Quantum Design Physical Property Measurement System (PPMS). A current of 5 mA was injected in the bars and the resulting voltage was measured using a sweep sequence for temperatures ranging from 300K to 70K at 0 T. The resistance was derived from Ohm's law and transformed into resistivity (ρ) using the equation: $\rho = R\frac{S}{L}$ where L is the distance between voltage contacts and S the section of the bar.

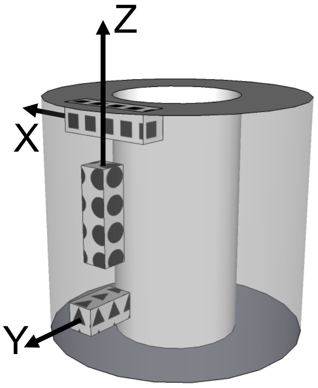

Figure 3.29 – Illustration of the way bars were cut in the tube for resistive measurements along (■) X, (▲) Y, and (•) Z directions.

Figure 3.30 shows the resistivity versus temperature curves for bars cut along X, Y, Z. For all three curves, the critical temperature, T$_c$, is 91.5K. The normal state resistivities along X and Z directions are similar and larger than the one measured along the Y direction. It means that electrical conduction is better along Y than along X and Z. These observations are consistent with the texture results since the main texture component corresponds to *ab* planes parallel to the Y direction (see Figure 3.25b). More discussion about the anisotropy of the electrical resistivity can be found in Chapter 6, where the experimental $\rho_{X,Z}(300\text{K})/\rho_Y(300\text{K})$ ratio, ≃2.3, will be compared to a calculation based on the experimentally determined orientation distribution and literature data for the single crystal resistivity tensor.

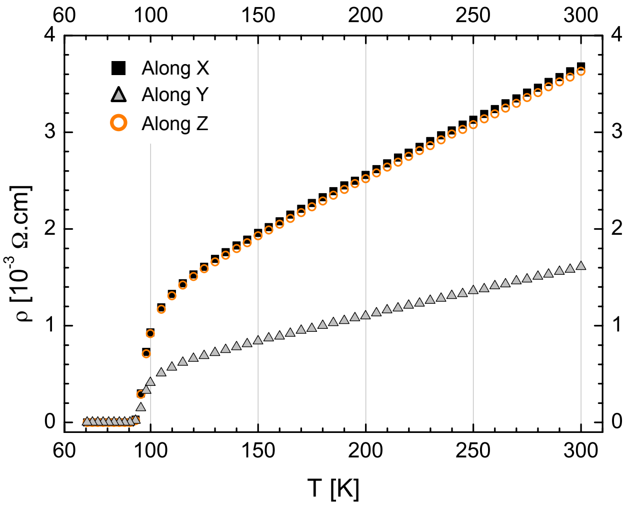

Figure 3.30 – Temperature dependence of electrical resistivity measured on 1x1x7mm^3 bars cut in the tube (■) along X, (▲) along Y, (○) and along Z.

Magnetic moment vs. magnetic field curves were measured at 4.2 K and up to 5 T in a Quantum Design SQUID. The measurements were carried out on an approximately 1x1x1mm^3 cube cut from the center part of the tube, with the magnetic field applied parallel to the X, Y and Z directions. Figure 3.31 shows the M(H$_{app}$) hysteresis curves for the three sample orientations. Above the full penetration field, the three curves are superimposed, meaning that in these conditions, J$_c$ is independent of the magnetic field orientation and thus unaffected by texture effects.

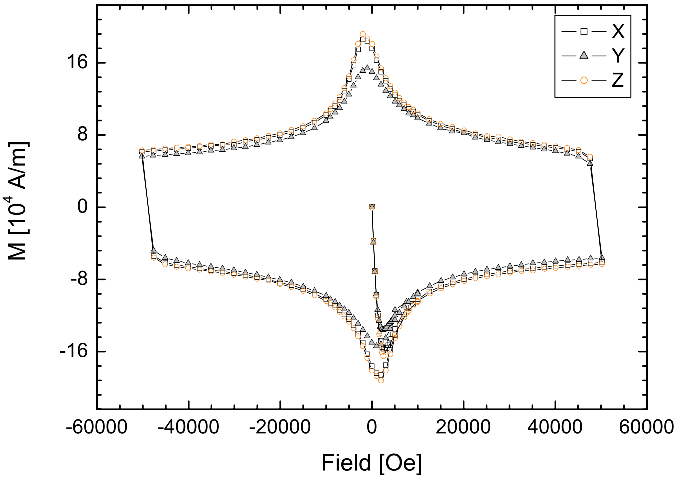

Figure 3.31 – M(H$_{app}$) curves at 4.2K for a sample extracted at the center of the tube and rotated to apply the magnetic field along X, Y, and Z directions.

3.6 Studying preferred orientation using a standard $\theta - 2\theta$ X-ray diffractometer

3.6.1 Limitations with respect to the full texture characterization

This section examines how texture may affect $\theta-2\theta$ patterns collected with a 0D (or a small 1D) detector in a standard Bragg-Brentano X-ray diffractometer. A typical geometry is shown in Figure 3.32, where the sample is not moved along the cradle angle (i.e., χ is fixed).

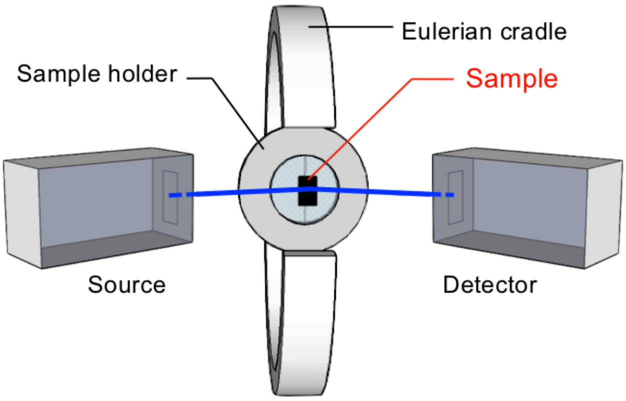

Figure 3.32 – Geometry of the X-ray diffractometer at Nexans SuperConductors.

In such a configuration, the detector receives only the intensity diffracted by (hk$l$) planes parallel to the sample surface. As a consequence, a non-random orientation of the crystallites can be detected as modifications of relative intensity ratios if some (hk$l$) planes are over-represented or under-represented in their orientation parallel to the surface.

A few simulated $\theta - 2\theta$ patterns for the Bi-2212 phase are shown in Figure 3.33 for illustration. Y is the direction perpendicular to the surface (XOZ plane) of the sample. The pattern of the untextured sample is shown for reference at the bottom of the figure, with the hk$l$ indices of the reflections. The other patterns correspond to a planar texture with c-axes distributed randomly in the sample plane and to fiber textures with c-axes oriented along X, Y, and Z respectively. In the case of the fiber texture with c parallel to Y, the (00l) planes are preferentially oriented parallel to the sample surface, so that the relative intensity of the corresponding reflections increases strikingly. The opposite is true in the case of the three other patterns, where the c-axes are preferentially oriented along the X direction, the Z direction or in the XOZ plane. In all these cases, the orientation of the (00l) planes parallel to the sample surface is underrepresented and the relative intensity of the

$(00l)$ reflections decreases. It is important to realize that the planar texture, the fiber texture with c-axes$\|$X, and the fiber texture with c-axes$\|$Z result in the same $\theta-2\theta$ diffraction pattern for fixed χ. This illustrates that a single $\theta-2\theta$ pattern does not always allow to discriminate between different textures.

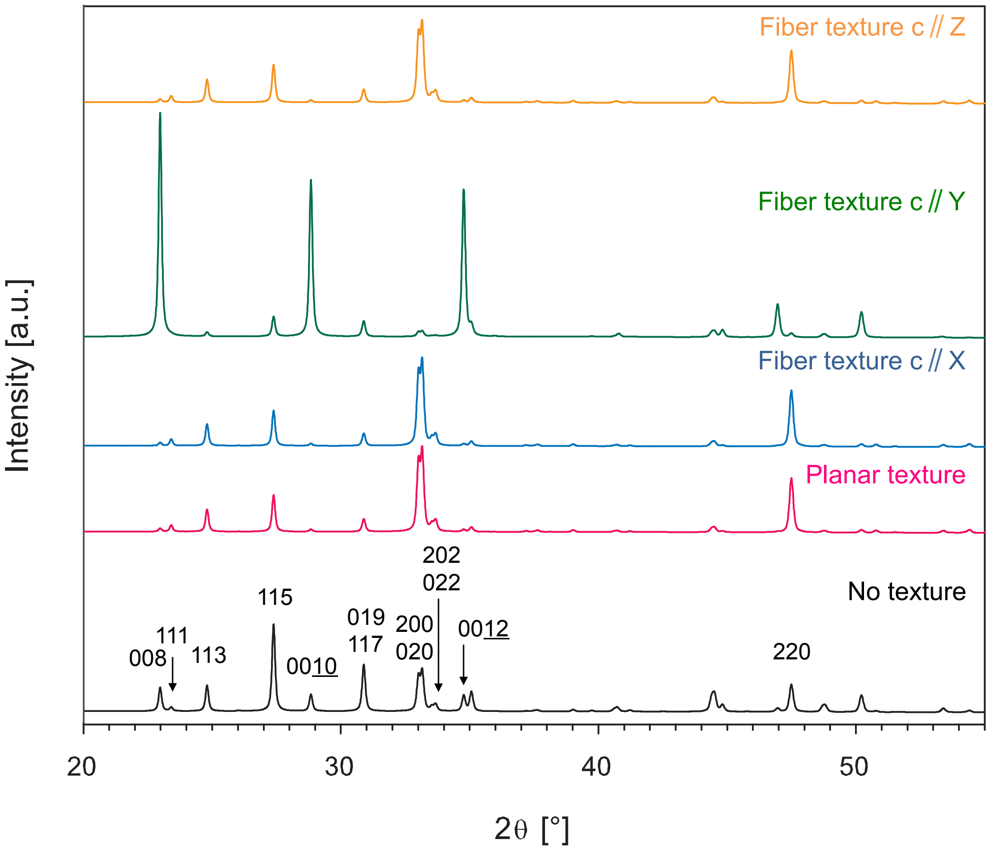

Figure 3.33 – $\theta-2\theta$ diffraction patterns simulated for Bi-2212 phase with (--) no texture, (--) a planar texture, (--) a fiber texture with c-axes$\|$X, (--) a fiber texture with c-axes$\|$Y, and (--) a fiber texture with c-axes$\|$Z.

This limitation can be further discussed by comparing the pole figures associated to the three fiber textures, displayed in Figure 3.34. For example, the three $\{006\}$ pole figures are different from each other but because a $\theta-2\theta$ diffraction experiment with fixed χ probes only the center of the probe figure, the c$\|$X and c$\|$Z fiber textures cannot be distinguished. The same is true for the other pole figures, as shown more clearly in Figure 3.35 where the $\{220\}$ pole figures are reproduced with a more convenient intensity scale. These few simple examples are provided as a proof that measuring a $\theta-2\theta$ diffraction pattern at only one (χ,φ) position does not ensure a full characterization of texture. This applies also to more complex cases, where several texture components coexist as in the previous sections. Each component of texture requires several (χ,φ) sample orientation to be measured.

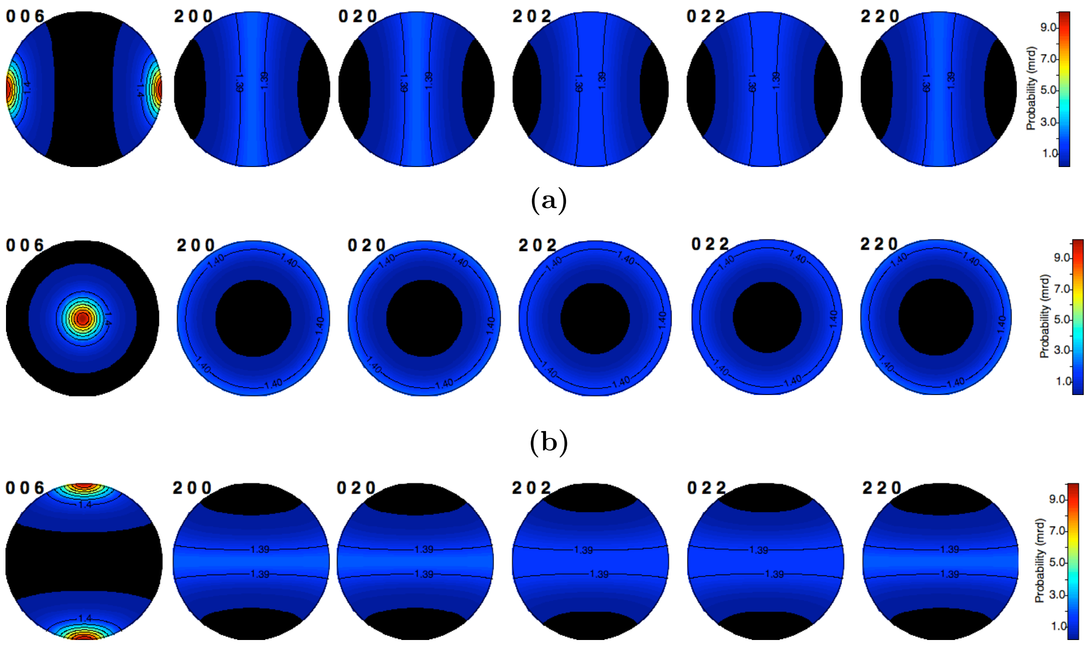

(a)

(b)

(c)

Figure 3.34 – Pole figures simulated for a fiber texture with c-axes aligned along (a) X, (b) Y, and (c) Z. All pole figures are simulated with a distribution of 30°.

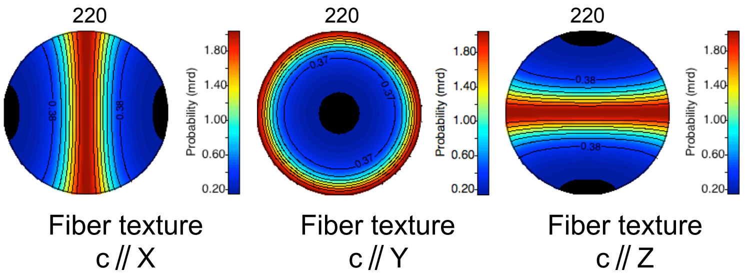

Figure 3.35 – {220} pole figures simulated (from left to right) for fiber textures with c-axes aligned with X, Y and Z, respectively.

3.6.2 March-Dollase approach for preferred orientation determination

When previous knowledge suggests that the texture of a sample can be described by a single texture component with unambiguous signature in the $\theta - 2\theta$ pattern at fixed χ, the "single pattern" approach retains its interest due to its simplicity, since it requires no dedicated equipment (or allocation of beamline time).

3.6.2.1 Rietveld refinement

In the case of Rietveld refinement of a pattern affected by preferred orientation, the influence of the preferred orientation is represented by the factors $P_{\Phi k}$ (one for each hk$l$ reflection) in the equation of the calculated intensities (see Section 2.2.3 in Chapter 2 for a description of the other factors):

$$y_{ic} = y_{ib} + \sum_{\Phi=1}^{N_\Phi} S_\Phi \sum_{k=K_1}^{K} j_{\Phi k} Lp_{\Phi k} P_{\Phi k} |F_{\Phi k}|^2 \Omega_{i\Phi k} A_i \tag{3.1}$$

When only a single pattern is available so that the full texture analysis is not possible, the $P_{\Phi k}$ factors are usually described by a March-Dollase function:

$$P_{\Phi k} = \frac{1}{\left[G^2 \cos^2 \varphi_{hkl} + \frac{1}{G} \sin^2 \varphi_{hkl}\right]^{3/2}} \tag{3.2}$$

where φ_{hkl} is the angle between [hk$l$]* and the direction of preferred orientation (that must be postulated through an educated guess) and G is a refinable parameter. G is the same for all reflections of the phase and is equal to 1 if no preferential orientation exists. Taking as an example the case of a preferential orientation of the (220) planes parallel to the sample surface with G=0.5, the intensity of the 220 reflection will be increased by a factor of:

$$P_{220} = \frac{1}{\left[0.5^2 \cos^2(0°) + \frac{1}{0.5} \sin^2(0°)\right]^{3/2}} = 8 \tag{3.3}$$

while the intensity of the 00l reflections will decrease due to a mutiplication by a factor of:

$$P_{00l} = \frac{1}{\left[0.5^2 \cos^2(90°) + \frac{1}{0.5} \sin^2(90°)\right]^{3/2}} = 0.35 \tag{3.4}$$

Figure 3.36 plots the March-Dollase function for φ_{hkl} angles between -90° and +90° for different values of G while Figure 3.37 plots $\theta - 2\theta$ patterns simulated for the Bi-2212 phase for different values of G considering that orientation of preferred orientation is either [220]* or [001]*.

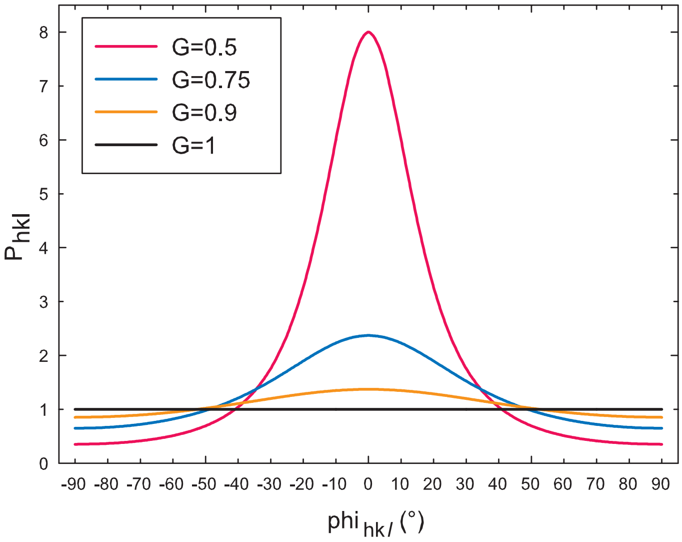

Figure 3.36 – March-Dollase function for φ_{hkl} angles between -90° and +90° for (--) G=0.5, (--) G=0.75, (--) G=0.9, and (--) G=1.

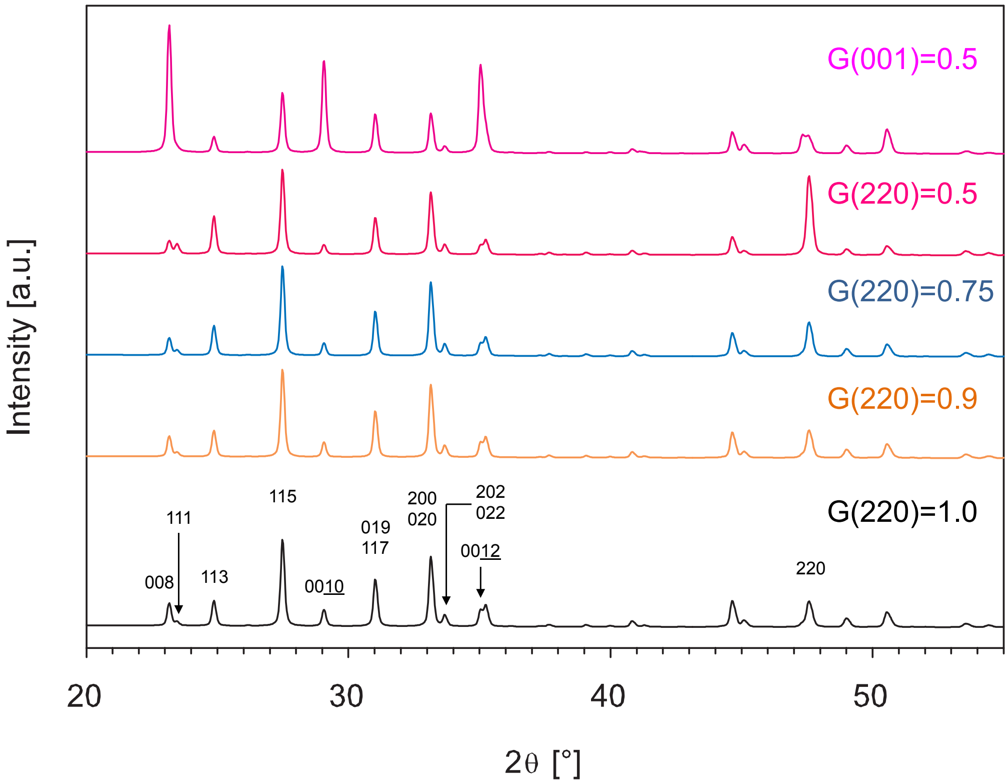

Figure 3.37 – $\theta - 2\theta$ diffraction patterns simulated for Bi-2212 phase for different values of G considering that orientation of preferred orientation is either [220]* or [001]*.

3.6.2.2 Principle of the procedure used at Nexans Superconductors [120, 121]

Because the Rietveld refinement of the $\theta - 2\theta$ pattern of the multiphase melt-cast processed materials is a very complex procedure, the researchers at Nexans Superconductors prefer to apply the March-Dollase approach to the integrated intensities of a few key reflections. As discussed above, preferred orientation in a material contributes to a variation of the integrated intensity of a hk$l$ reflection (I_{hkl}^{pref}) compared to the intensity of the same reflection in an isotropic material (I_{hkl}^{iso}). The intensity ratio between two reflections hk$l$,1 and hk$l$,2 can then be written:

$$\frac{I_{hkl,1}^{pref}}{I_{hkl,2}^{pref}} = \frac{I_{hkl,1}^{iso}\left[PO^2\cos^2\varphi_{hkl,1} + \frac{1}{PO}\sin^2\varphi_{hkl,1}\right]^{-3/2}}{I_{hkl,2}^{iso}\left[PO^2\cos^2\varphi_{hkl,2} + \frac{1}{PO}\sin^2\varphi_{hkl,2}\right]^{-3/2}} \tag{3.5}$$

where 'G' of equation 3.2 is renamed 'PO' to follow standard practice at Nexans Superconductors.

The 200 line is chosen as hk$l$,2 because it is one of the most intense and it allows to reduce as much as possible the error σ_{hkl} of measured relative intensities:

$$\sigma_{hkl} = \frac{I_{hkl}}{I_{200}}\sqrt{\left(\frac{\sigma_{I_{hkl}}}{I_{hkl}}\right)^2 + \left(\frac{\sigma_{I_{200}}}{I_{200}}\right)^2} \tag{3.6}$$

PO can be evaluated using different hk$l$ reflections and an average PO value is determined by least-square minimization of

$$\chi^2 = \frac{1}{N-1}\sum\frac{\left[\frac{I_{hkl}^{obs}}{I_{200}^{obs}} - \left(\frac{I_{hkl}}{I_{200}}\right)_{calc}\right]^2}{\sigma_{hkl}^2} \tag{3.7}$$

where $\left(\frac{I_{hkl}}{I_{200}}\right)_{calc}$ is calculated with Equation 3.5 and N is the number of reflections used.

3.6.2.3 Experimental details

A piece of tube was cut along the tube axis as illustrated in gray in Figure 3.38. The sample was embedded in resin and measurements were made at different depths across the tube thickness thanks to successive polishings.

Figure 3.38 describes the sample reference frame for PO measurements at Nexans. The reference frame is the same as described in previous sections for texture measurements: the Y-axis is oriented along the normal to the surface. The Z-axis is oriented along the tube axis. The diffractometer at Nexans Superconductors is a D5000 Siemens diffractometer equipped with a Cu X-ray tube and an Eulerian cradle. Measurements were performed at χ=90° and φ=0° with the long side of the sample (i.e. the Z direction) placed vertically. The geometry of the diffractometer was already shown in Figure 3.32.

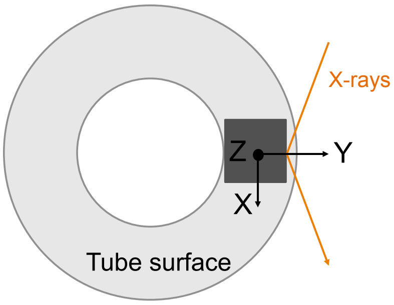

Figure 3.38 – Description of the reference frame for the sample (dark gray) used for PO measurements. The sample was cut with its longest side along the tube axis. The reference frame is defined with Z along the tube axis, X axis is tangent to the surface and Y is the radial direction.

The measurement procedure consists in the following:

1. A fast θ-2θ scan is collected to evaluate roughly the position of the $00\underline{10}$ and 200 reflections in 2θ.
2. θ-2θ scans from 28.5° to 29.5° ($00\underline{10}$ reflection) and from 32.5° to 34° (200 reflection) are collected with a higher resolution than the first one to determine for each reflection the angular position of maximum intensity.
3. A scan is collected at a fixed position in 2θ (i.e. angular position of maximum intensity of $00\underline{10}$ or 200 reflection) by moving the sample under the beam along the X direction. This scan is used to determine the exact position of the sample in the resin. Figure 3.39(b) illustrates schematically the X-scan associated to the sample, the zone of highest intensity corresponds to the position of the sample in the resin.

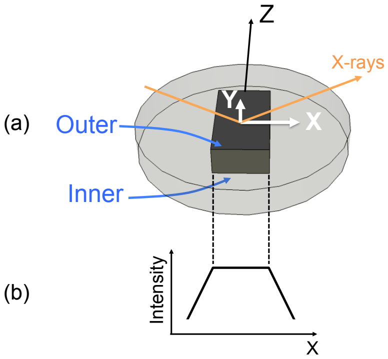

Figure 3.39 – (a) Description of the reference frame for the sample embedded in resin and (b) illustration of the associated X-scan.

4. θ-2θ scans are collected in a 2θ range from 23° to 48° that allows to measure the intensity of the main Bi-2212 reflections listed in the table shown in Figure 3.40.

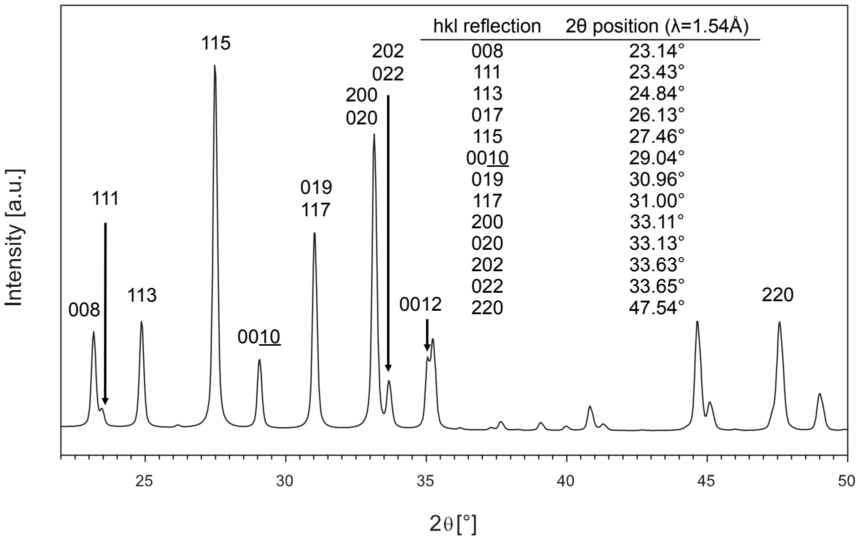

hkl reflection	2θ position (λ=1.54Å)
008	23.14°
111	23.43°
113	24.84°
017	26.13°
115	27.46°
0010	29.04°
019	30.96°
117	31.00°
200	33.11°
020	33.13°
202	33.63°
022	33.65°
220	47.54°

Figure 3.40 – 2θ position of the main reflections of Bi-2212 phase between 23° and 48° in 2θ. Inset table is the list of 2θ positions for major hk$l$ reflections of Bi-2212 phase.

3.6.2.4 Evolution of PO across the tube thickness

The PO parameter was determined by M.O. Rikel at Nexans Superconductors for different positions across the thickness of the tube (i.e. along the Y axis), taking [001]* as the direction of preferential orientation. The integrated areas under the 008, 111, 113, 115, 0010, 117, 202 and 220 reflections were obtained from the diffraction patterns using the Bruker software EVA. Figure 3.41 shows the evolution of PO along the tube thickness from the outer surface (0mm) to inner surface (7mm) for a tube similar to the one we have studied in this chapter. Samples 1 and 2 correspond to two different but equivalent parts of the tube. PO starts from 1 (no preferred orientation) at the outer surface, increases to reach a plateau between ~2mm and ~4mm and decreases to reach almost PO=1 near the inner surface. The region characterized by a plateau corresponds to what we previously called the center region of the tube, where texture is best defined. The PO value of ~1.5 in this region indicates a preferred orientation of the *c*-axes parallel to the surface of the sample. In other words, the *ab* planes are preferentially oriented perpendicular to the surface of the sample. This preferential orientation corresponds to the planar-like texture component where *c*-axes are oriented in the XOZ plane of the tube. This is the main texture component identified during the full texture characterization. However, this procedure does not allow to detect the minor texture components, and might become problematic if the volume of the sample probed by the XRD experiment contains the same phase with different textures of similar strength.

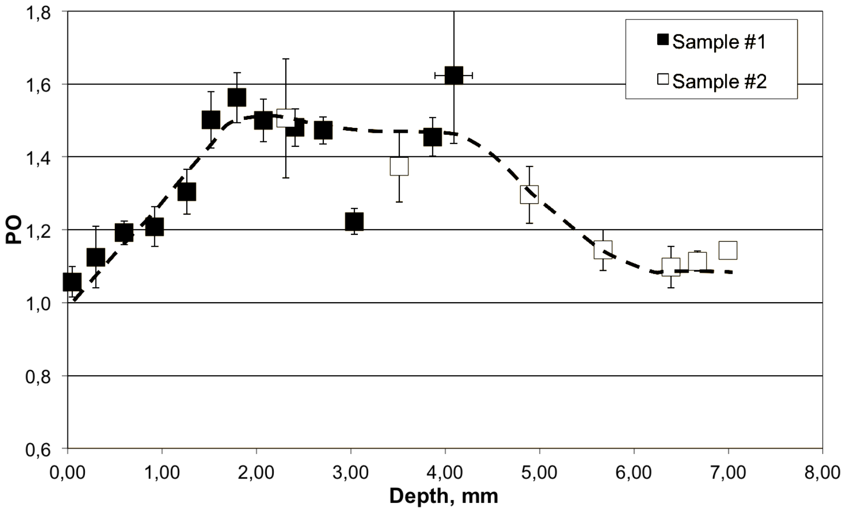

Figure 3.41 – March Dollase parameter, PO as function of the depth of the tube, from outer surface (0mm) to inner surface (7mm).

3.7 Conclusion

This chapter was devoted to the characterization of a melt-cast processed Bi-2212 tube through a variety of measurements to determine the microstructure, texture and some physical properties of the tube.

Regarding microstructure, the tube can be divided in several regions: inner, porous, center, and outer, composed of a matrix of $Bi_2Sr_2CaCu_2O_8$ (~ 70-80%) and inclusions of second phases that can reach sizes of 100μm. The two principal second phases are $(Ba,Sr)SO_4$ and $(Ca,Sr)CuO_2$, with a minor second phase, $(Ca,Sr)_2CuO_3$.

The texture in the tube was studied using an X-ray 4-circle diffractometer and two neutron beamlines (D1B and D19) at the ILL. All calculations were based on Rietveld refinements in the program MAUD, using the E-WIMV model for texture calculation. Neutrons probed the entire sample volume while X-rays only probed the first 10μm at the surface of these samples. These experiments showed that texture is weak in the tube. The main texture component indicates that most of the crystallographic ab-planes, containing CuO_2 conductive planes, are parallel to and randomly distributed around the Y-axis (radial direction) of the tube. A <001>-fiber texture with *c*-axes close to the Y-axis is a minor texture component, corresponding to small orientation volume. The comparison of texture experiments on different probed volumes suggests that variations in the strength texture components.

Resistivity (vs. temperature) and magnetization (vs. magnetic field) were measured along the three main directions of the tube. An anisotropy of the normal state electrical resistivity was revealed, with a ratio of 2.3 between the resistivity along the tube axis and the resistivity along the radial direction. These observations are qualitatively consistent with the texture results regarding ab-plane orientations. Magnetization was not much affected by the direction of magnetic field orientation.

Finally, we have discussed the limitations of the procedure used at Nexans Superconductors Gmbh to calculate a preferred orientation index using a March-Dollase model and θ-2θ patterns acquired at only one (χ, φ) position. It has been demonstrated that the procedure cannot replace a full texture characterization. However, the main texture component of the Bi-2212 tube is such that it can be detected by the procedure. Consequently, the March-Dollase model can be used as a first approach to characterize texture in the tube, as long as the main texture component corresponds to an orientation of the ab-planes in the tube around the radial direction.

CHAPTER 4 | *Homogeneity of the tube*

Tubes manufactured by Nexans Superconductors Gmbh are long samples synthesized by a melt-cast process in a rotating mould followed by post-annealing (see section 1.3.1 in Chapter 1). This procedure results in temperature gradients and differences of cooling rates in different parts of the tube. It is therefore appropriate to investigate the homogeneity of the tube in terms of microstructure, texture, or physical properties. This chapter proposes an analysis of the tube homogeneity (i) across the tube wall thickness and (ii) along the tube length and perimeter.

Chapter content

4.1 Homogeneity across the tube wall thickness

The homogeneity of the microstructure, texture and physical properties across the tube thickness was investigated by characterizing samples extracted from the inner, center and outer part of the tube wall, as detailed in Chapter 3 and schematically shown in Figure 4.1.

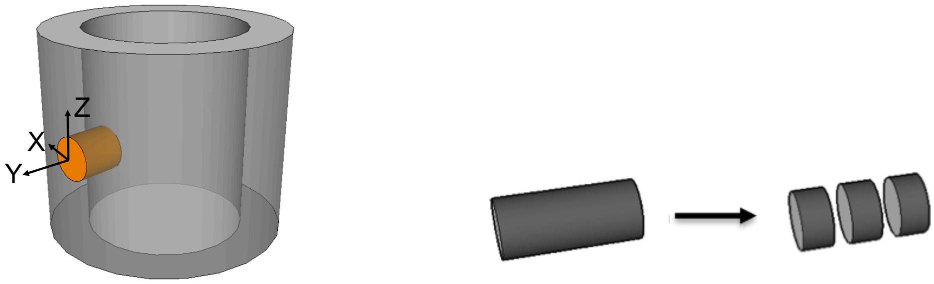

(a) Sample extracted across the tube thickness

(b) 3 parts of the tube: inner, center, outer

Figure 4.1 – (a) Illustration of the sample cut in the tube for diffraction measurements and (b) cut of this sample in inner, center, and outer parts.

4.1.1 Microstructure

The microstructure of the inner, center, and outer parts of the tube (Figure 4.2) has already been discussed in the previous chapter (See section 3.1.2). The differences in porosity and amount of second-phase inclusions are summarized in Table 4.1.

Part of the tube	Microstructure
Inner	High amount of second phase inclusions, porous in the 500μm-thick layer closest to surface
Center	Dense with second phase inclusions, separated from the inner part by a thick layer with large pores ("solidification shrink hole")
Outer	Dense with second phase inclusions whose size decreases to approximately 10μm when approaching the surface

Table 4.1 – Description of the tube microstructure in the inner, center and outer parts across the wall thickness.

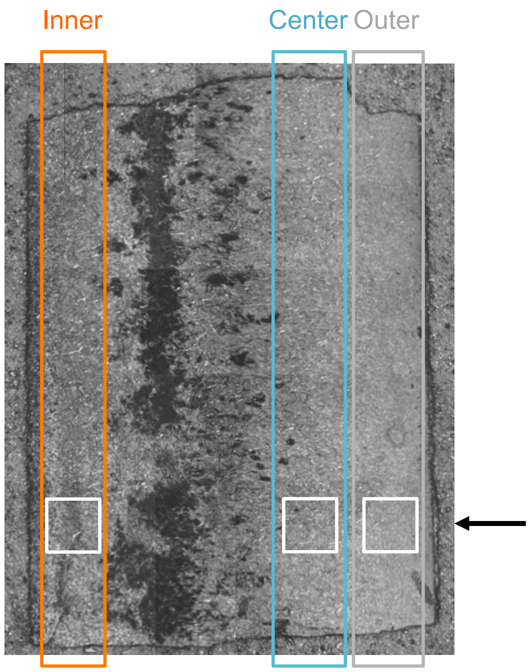

Position of the inner, center, and outer samples cut in the tube for ρ(T) and M(H,T) measurements

Figure 4.2 – Description of the different parts of the tube: inner (close to the inner edge of the tube), center (between the end of porosity and the outer edge of the tube), and outer (close to the outer edge of the tube). Small white squares indicate the position of the inner, center, and outer samples cut in the tube for ρ(T) and M(H,T) measurements

4.1.2 Texture and phase content

Texture was measured on the inner, center and outer parts using the D19 beamline at ILL. The bulk sample preparation and the conditions for data collection are the same as described in section 3.3.1.1. The normalized $\{200\}$, $\{020\}$, and $\{00\underline{10}\}$ pole figures calculated from the D19 data are shown in Figure 4.3 (a) to (c). All pole figures, whatever the sample, show weak maxima of orientation density, i.e., not higher than 1.3 m.r.d. The texture is best defined in the center sample, whose texture (discussed in section 3.5.2 of Chapter 3) is characteristic of texture with c-axes at random in the XOZ plane and *a*-axes and *b*-axes distributed at random around c-axes in the XOZ plane. The texture of the inner sample is close to random orientation but one still sees a weak $\{200\}$ equator reinforcement and a weak planar texture component in the $\{00\underline{10}\}$ pole figure.

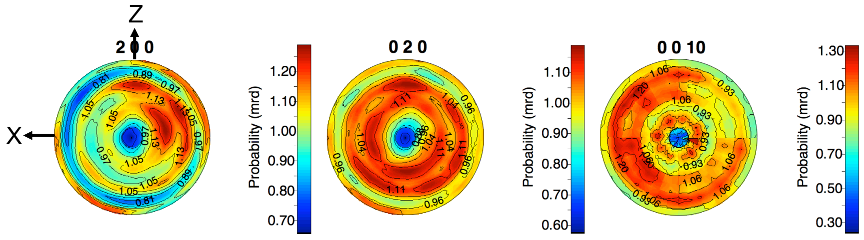

(a) Inner

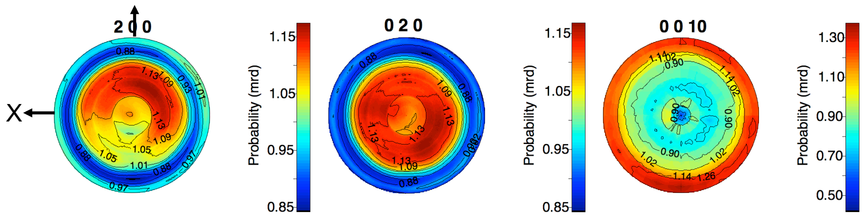

(b) Center

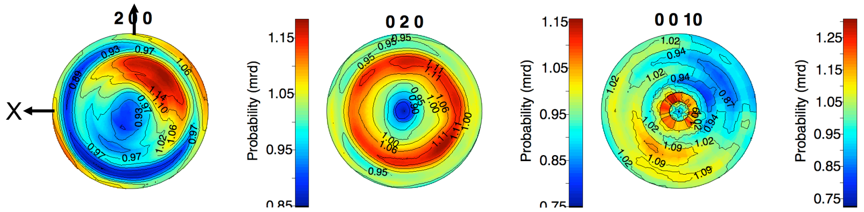

(c) Outer

Figure 4.3 – {200}, {020}, and {00$\underline{10}$} normalized pole figures calculated from data acquired on D19 instrument for samples cut from (a) inner, (b) center, (c) and outer part of the tube.

The volume percentage of the different phases in the inner, center and outer samples were calculated by quantitative texture analysis using the D19 data presented above. The volume proportion of Bi-2212 is between 72 and 80%, with the lower value for the outer sample. However, only the two main phases are taken into account in the refinements.

	Phase volume proportion [%]	
Sample	**Bi-2212**	**(Ba,Sr)SO$_4$**
Inner	78	22
Center	80	20
Outer	72	28

Table 4.2 – List of phase volume proportion estimated in different parts of the tube using D19 data.

4.1.3 Electrical and magnetic properties

Electrical resistivity was measured on small bars of 1x1x7mm^3 cut from the inner, center and outer parts of the tube wall, with the long axis of the bars parallel to the tube axis (Z). The positions of the samples cut in the tube are illustrated in Figure 4.2. The measurements were carried out with the usual four-probe technique in a Quantum Design Physical Property Measurement System (PPMS). Four contacts were made on the bar with indium, two contacts were made on the smaller edges of the bar and two other contacts were made on a long face of the bar. A current of 5 mA was injected in the bars and the resulting voltage was measured using a sweep sequence for temperatures ranging from 300K to 70K at 0 T. The resistance was derived from Ohm's law and transformed into resistivity (ρ) using the equation: $\rho = R\frac{S}{L}$ where L is the distance between voltage contacts and S the section of the bar.

The electrical resistivity vs. temperature curves are presented in Figure 4.4. The three samples display positive slopes of the resistivity vs temperature dependence above T_c. The normal state resistivity of the bar cut in the outer part of the tube is somewhat lower than in the other two samples. However, the difference does not exceed a factor of 1.3, some of which possibly resulting from differences in porosity. By comparison, the difference in resistivities along the X or Z and the Y axis measured in Chapter 3 was significantly larger (ρ(Z)/ρ(Y)=2.3 at normal state). In the present case, there does not seem to be a correlation with texture, which is weak in all cases. The lower resistivity in the outer sample might be related to the smaller size of second phase inclusions, which would tend to decrease the length of percolation paths and increase the effective cross-section for current transport if the second phases are considered as insulators.

Figures 4.5 (a) and (b) both display an enlargement of the ρ(T) curve centered on the superconducting transition. The critical temperature T_c is respectively 92.5K, 92.5K, and 93K in the inner, center and outer parts of the tube. These very close Tc values suggest that the cationic ratios and the oxygen content of the Bi-2212 phase do not vary significantly across the tube wall. This is confirmed, on the one hand, by EDX analyses (not shown) and, on the other hand, by the absence of a shift in the cell parameter c (as shown by the $00\underline{10}$ reflections of the Inel data for inner, center and outer samples in Figure 4.6.

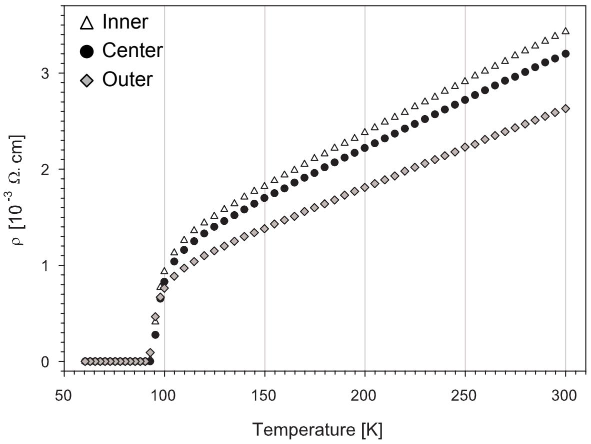

Figure 4.4 – Temperature dependance of resistivity measured on 1x1x7mm^3 bars cut in the tube (△) in inner part, (•) in center part, (◆) and in outer part.

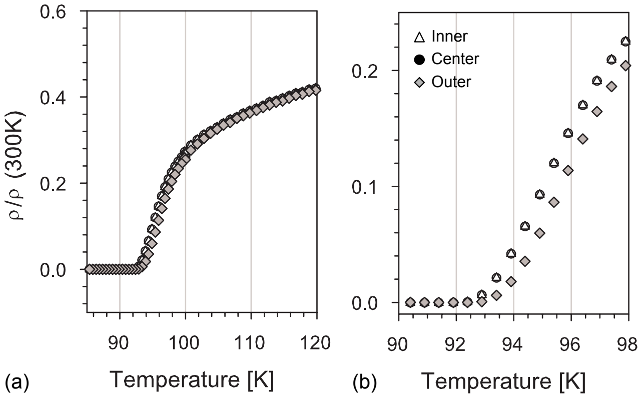

Figure 4.5 – Zooms on the ρ(T) transition of Figure 4.4. Resistivities are normalized over ρ(300K).

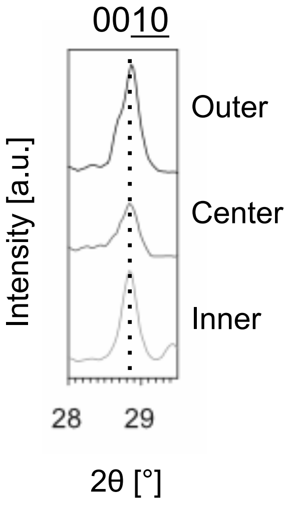

Figure 4.6 – 00<u>10</u> diffraction peak from Inel data of inner, center, and outer samples.

The magnetic moment of cubes of approximately 1x1x1mm^3 (the exact sizes are listed in Table 4.3) extracted from the inner, center and outer parts of the tube wall was measured at 4.2 K as a function of magnetic field. The measurements were carried out in a Quantum Design SQUID with the applied magnetic field (H_{app}) up to 5 T applied parallel to the tube axis (Z) direction. The M(H_{app}) hysteresis curves are presented in Figure 4.7. Since the samples have the same geometry, it is not necessary to take demagnetization effects into account in order to compare the curves of the different samples. The hysteresis curves can be used to assess the critical current densities J_c, which is proportional to ΔM calculated as the difference between the magnetization in the field increasing and the field decreasing sectors in the region where the applied magnetic field is higher than the penetration field. [122] From the difference in the values of ΔM for the three curves, it can be concluded that the highest J_c is found for the center part of the tube. An intermediate J_c is observed for the outer part and the lowest J_c is that of the inner part. The higher J_c of the inner part is consistent with transport J_c measurements at 77K carried out at Nexans Superconductors[1].

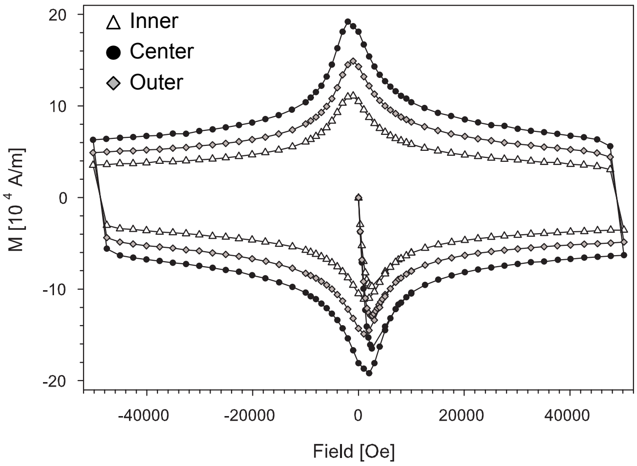

Figure 4.7 – M(H_{app}) curves at 4.2K for samples cut in inner, center, and outer parts of the tube with applied magnetic field parallel to Z axis of the tube.

Sample	Weight [g]	L_X [mm]	L_Y [mm]	L_Z [mm]
Inner	0.0059	1.02	1.03	0.99
Center	0.0062	1.00	0.99	0.98
Outer	0.0060	1.02	0.99	0.99

Table 4.3 – Weight and dimensions of the samples cut from the tube and used for M(H) measurements.

---

1. Transport J_c measurements: S. Elschner, 1996 private communication to Mark Rikel

4.2 Homogeneity along the tube axis and around the tube axis

A second set of measurements was performed on the tube to compare texture at different positions along the tube axis (Z) and around its perimeter (α). To do this five cylinders were extracted from the tube (represented by circles 1 to 5 in Figure 4.8. Samples 1 to 3 were extracted at different positions along the tube axis Z and samples 2, 4, and 5 at 120° from one another around the tube axis. Since it was found in the previous section that the tube texture is more clearly defined in samples extracted from the center of the tube wall, all the characterizations in the present section were done on central parts.

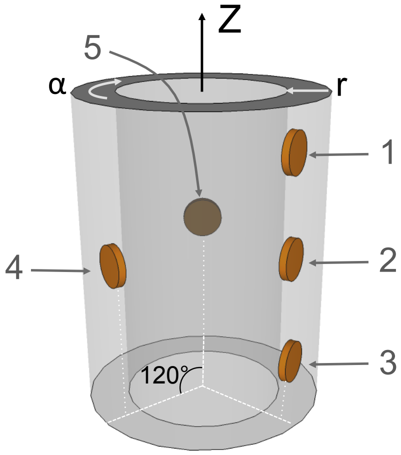

Figure 4.8 – Illustration of the tube cut for D1B measurements, 5 cylinders were extracted at different (Z, α) positions. Samples 1 to 5 were cut in 3 parts (inner, center, and outer) and only the center parts were used for the measurements.

4.2.1 Texture and phase content

Texture was measured using the D1B beamline at ILL. The sample mounting and the conditions for data collection are the same as described in Section 3.3.2.

The normalized {200}, {020}, and $\{00\underline{10}\}$ pole figures calculated from the D1B data are presented in Figure 4.9 for samples 1 to 3 and in Figure 4.10 for samples 2, 4, and 5. The texture is similar in all samples but the texture strength for the fiber textures is higher in {020} and $\{00\underline{10}\}$ pole figures of samples 1 and 2, as marked by higher values for the maximum of orientation density compared to the same pole figure for other samples. As explained in more detail in Section 3.5.2 the sharp orientation peaks in the center of {020} and $\{00\underline{10}\}$ corresponds to small orientation volumes. In Figure 4.9a, {020} and $\{00\underline{10}\}$ pole figures of sample 1 are represented by limiting the orientation density scale to 2 m.r.d.. By doing so, these pole figures reveal a texture similar to the texture of sample 3.

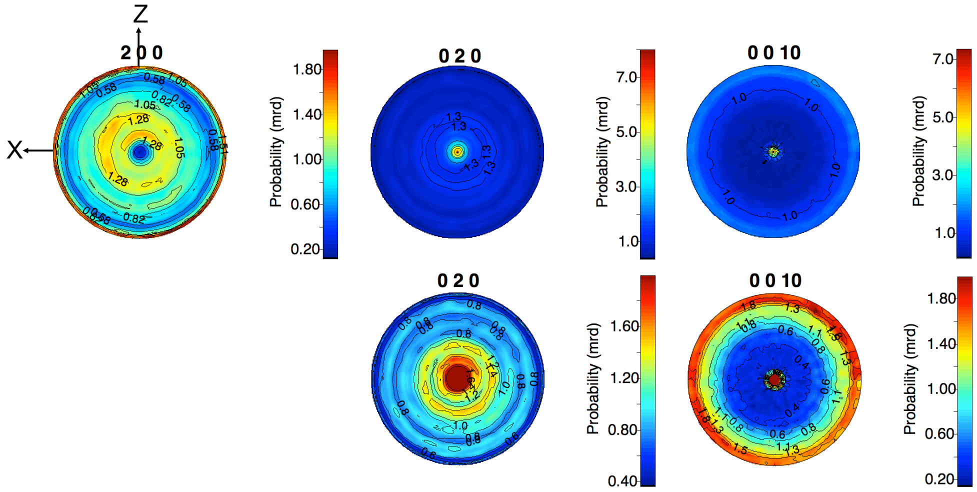

(a) Part 1

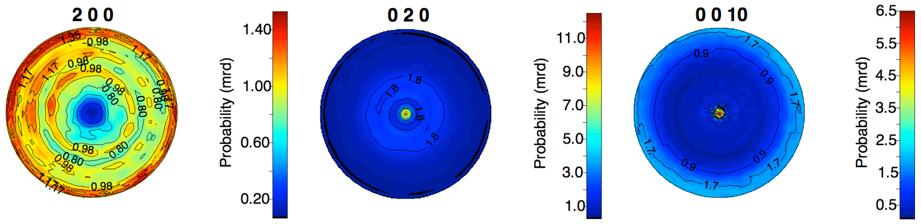

(b) Part 2

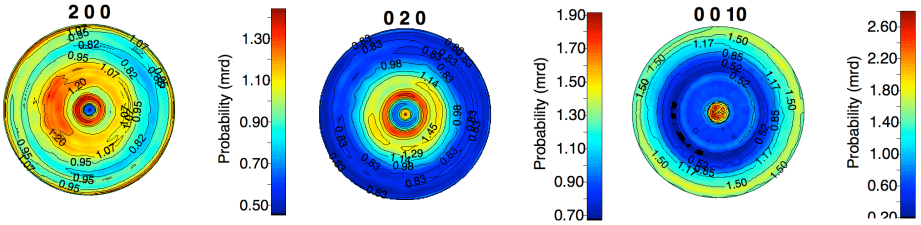

(c) Part 3

Figure 4.9 – {200}, {020}, and {00$\underline{10}$} normalized pole figures calculated from data acquired on D1B instrument for tube samples 1 to 3 extracted at different positions along the tube axis.

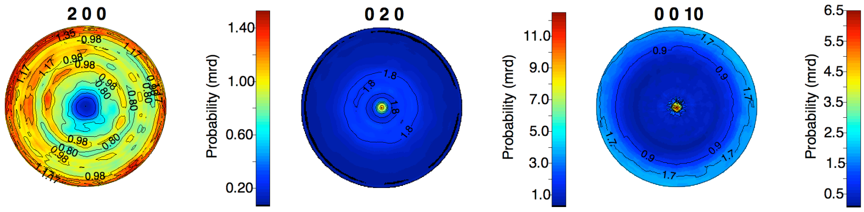

(a) Part 2

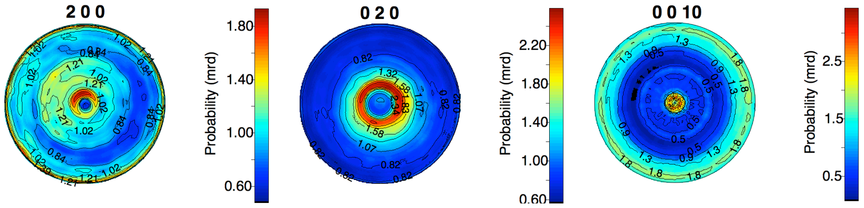

(b) Part 4

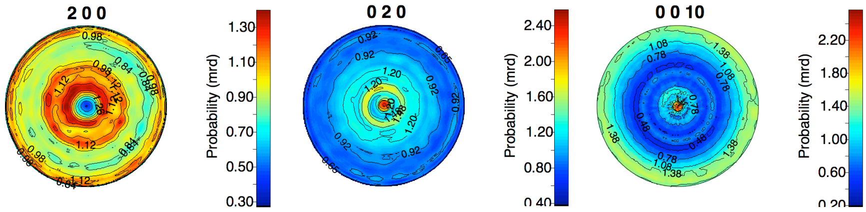

(c) Part 5

Figure 4.10 – {200}, {020}, and {00<u>10</u>} normalized pole figures calculated from data acquired on D1B instrument for tube samples 2, 4, 5 extracted at the same position along the tube axis but at 120° from one another.

The volume fraction of different phases in the different samples were calculated by quantitative texture analysis using the Inel data and are displayed in Table 4.4. As in the previous section, phase contents determined from Inel data are shown because the better resolution allows to distinguish more phases. Globally, all samples presented above show a phase volume proportion of Bi-2212 between 61 and 77%.

		Phase volume proportion		
Sample	**Instrument**	**Bi-2212**	**(Ba,Sr)SO_4**	**(Ca,Sr)CuO_2**
Part 1	Inel	77%	18%	5%
Part 2	Inel	61%	28%	11%
Part 3	Inel	72%	19%	9%
Part 4	Inel	65%	26%	9%
Part 5	Inel	72%	21%	7%

Table 4.4 – List of phase volume proportion estimated in different tube samples.

4.3 General conclusion on tube homogeneity

The objective of this chapter was to examine the homogeneity of the tube studied in Chapter 3 across the tube wall thickness and along the tube length and perimeter.

The homogeneity across the tube wall thickness was considered by studying samples cut along the tube wall and called inner, center, and outer parts. Calculations of texture and phase proportions was done in MAUD using Rietveld refinements of D19 data. Refinements converge to Bi-2212 phase volume proportions between 70 and 80%. The center part of the tube shows the highest amount of Bi-2212 and the texture component corresponding to ab-planes parallel to the radial direction. The inner and outer part of the tube show a <001> weak fiber texture, which is not observed at the center of the tube. All parts of the tube have similar T_c's and the difference in normal state resistivities does not exceed a factor of 1.3. The center part of the tube is the one showing highest J_c values.

Secondly, the homogeneity of the tube along its length and around its principal axis was considered by comparing 3 samples cut in the center of the tube wall at different heights in the tube and 3 samples cut in the center of the tube wall at different positions around the perimeter of the tube. The pole figures refined from D1B data display some differences in the texture strength associated to the fiber texture components but since these correspond to small volumes, the conclusion is that the tube can be considered as homogeneous in texture on its length and around its principal axis.

CHAPTER 5 | *Rod samples*

This chapter concerns melt-cast processed samples shaped as rods of different diameters and annealed to different oxygen contents (δ in the $Bi_2Sr_2CaCu_2O_{8+\delta}$ phase). The first section of the chapter provides a short description of the samples. The second section reports about the microstructure and texture characterization of two series of samples: a first series of three rods with different diameters and a second series of 8 mm diameter rods with different oxygen contents. Because oxygen equilibration by annealing is more efficient in the case of smaller samples, the influence of the oxygen content on the physical properties is investigated in the third section for 5 mm diameter rods.

Chapter content

5.1 Description of the samples

Rods manufactured by Nexans Superconductors Gmbh are full cylinders synthesized by melt-casting followed by post-annealing (see section 1.3.1 in Chapter 1). Samples are first annealed to convert the as-melt-cast material into Bi-2212. The oxygen content (8+δ) can then be adjusted during a second annealing along T-pO_2 trajectories calculated from the diagram given by Schweizer et al. (Figure 5.1) [54]. This diagram shows that higher values of δ (d on the diagram) are reached for lower post-annealing temperatures and vice-versa.

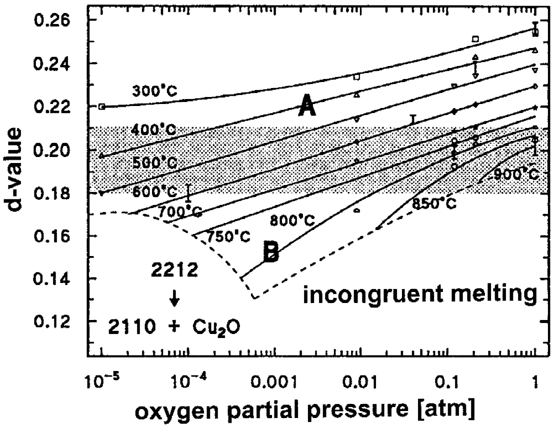

Figure 5.1 – The d value (d = oxygen stoichiometry - 8) of the 2212 phase versus the oxygen partial pressure during heat treatment at different temperatures of 20 mm diameter pellets [54].

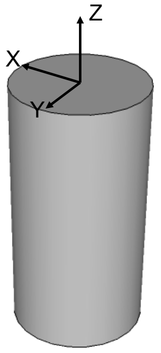

Figure 5.2 – Reference frame established for the rod samples with Z axis along the rod axis and X, Y in the radial plane.

Rods are manufactured with different diameters, i.e. 5mm, 8mm or 15mm diameter. For all rods, the reference frame (See Figure 5.2) is taken with the Z axis along the rod axis (X and Y are arbitrary radial directions). Depending on the requirements for the different kinds of characterizations of the rods, the rods were cut with different shapes and sizes, as described in the relevant sections. All rods studied in this chapter are listed in Table 5.1, 5.2 and 5.3 and named according to their diameter and δ value : **Rod-diameter size-δ value**. The oxygen content in the table is the nominal one, deduced from the Schweizer et al. diagram. The qualitative evolution of the oxygen content is verified from the variation of the c cell parameter, as reported in the next sections.

Sample	Oxygen content ($O_{8+\delta}$)	Nexans code
Rod–5mm-0.175	δ=0.175	147-5-6-0.175
Rod-5mm-0.180	δ=0.180	147-5-6-0.180
Rod-5mm-0.185	δ=0.185	147-5-5-0.185
Rod-5mm-0.190	δ=0.190	147-5-7-0.190
Rod-5mm-0.200	δ=0.200	147-5-5-0.200
Rod-5mm-0.210	δ=0.210	147-5-5-0.210
Rod-5mm-0.219	δ=0.219	147-5-5-0.219
Rod-5mm-0.225	δ=0.225	147-5-7-0.225
Rod-5mm-0.232	δ=0.232	147-5-6-0.232
Rod-5mm-0.240	δ=0.240	147-5-6-0.240
Rod-5mm-0.245	δ=0.245	147-5-6-0.245
Rod-5mm-0.248	δ=0.248	147-5-4-0.248
Rod-5mm-0.252	δ=0.252	147-5-5-0.252

Table 5.1 – List of 5mm diameter rods denominated Rod-diameter size-δ value and their corresponding δ value and Nexans code.

Sample	Oxygen content ($O_{8+\delta}$)	Nexans code
Rod-8mm-0.187	δ=0.187	R3904
Rod-8mm-0.198	δ=0.198	R3900
Rod-8mm-0.205	δ=0.205	R3903
Rod-8mm-0.215	δ=0.215	R3902
Rod-8mm-0.225	δ=0.225	R3915
Rod-8mm-0.230	δ=0.230	R3929

Table 5.2 – List of 8mm diameter rods denominated Rod-diameter size-δ value and their corresponding δ value and Nexans code.

Sample	Oxygen content ($O_{8+\delta}$)	Nexans code
Rod-15mm-0.203	δ=0.203	146-01

Table 5.3 – 15mm diameter rod denominated Rod-diameter size-δ value and its corresponding δ value and Nexans code.

5.2 Microstructure and texture

This section is dedicated to the investigation of the influence of the rod diameter size and the rod oxygen content using two series of samples. Each subsection starts by a description of the microstructure of the samples and continues with texture results.

5.2.1 Rods with different diameters and similar oxygen content

In order to investigate the effect of rod diameter, we selected rods with a diameter of 5mm, 8mm, and 15mm and similar oxygen content: Rod-5mm-0.200, Rod-8mm-0.205 and Rod-15mm-0.203. There is one difference between synthesis process of the rods: 5 and 8 mm rods were obtained by casting in quartz ampoules preheated to 800° C, whereas 15 mm rod were cast in the non preheated ampoules. The time-temperature paths upon solidification are therefore different.

5.2.1.1 Microstructure

Due to a shrinkage during solidification, the center of the rods is highly porous, as shown in the optical micrograph of Figure 5.3.

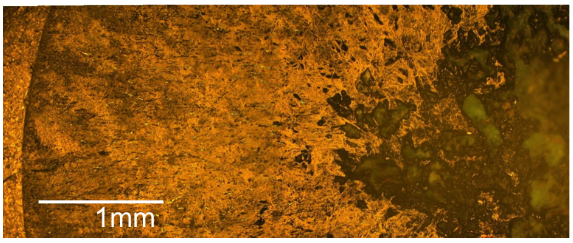

Figure 5.3 – Image of the half cross-section of a 8mm rod acquired with an optical microscope.

Figure 5.4 displays panoramas of polished cross-section of the 5mm, 8mm, and 15mm rods, made using second electron SEM images. Micrographs at higher magnification are shown in Figure 5.5. Visual inspection suggests that, compared to the 8 mm rod, the 5mm rod shows a higher amount of second phases inclusions, with a smaller size. Compared to the 8 mm rod, the 15mm rod also shows a higher amount of second phases inclusions, with similar sizes explained by the difference in synthesis process. In all rods, the second phase inclusions tend to align along the rod radius. As observed for the tube sample in Chapter 3, the rods have a different microstructure at the edges. During the cooling step, the outside surface of the rods cools faster than the center of the rods. This results in a more advanced grain growth at the center of the rod than at the edges explaining why grains are smaller at the edges than close to the center.

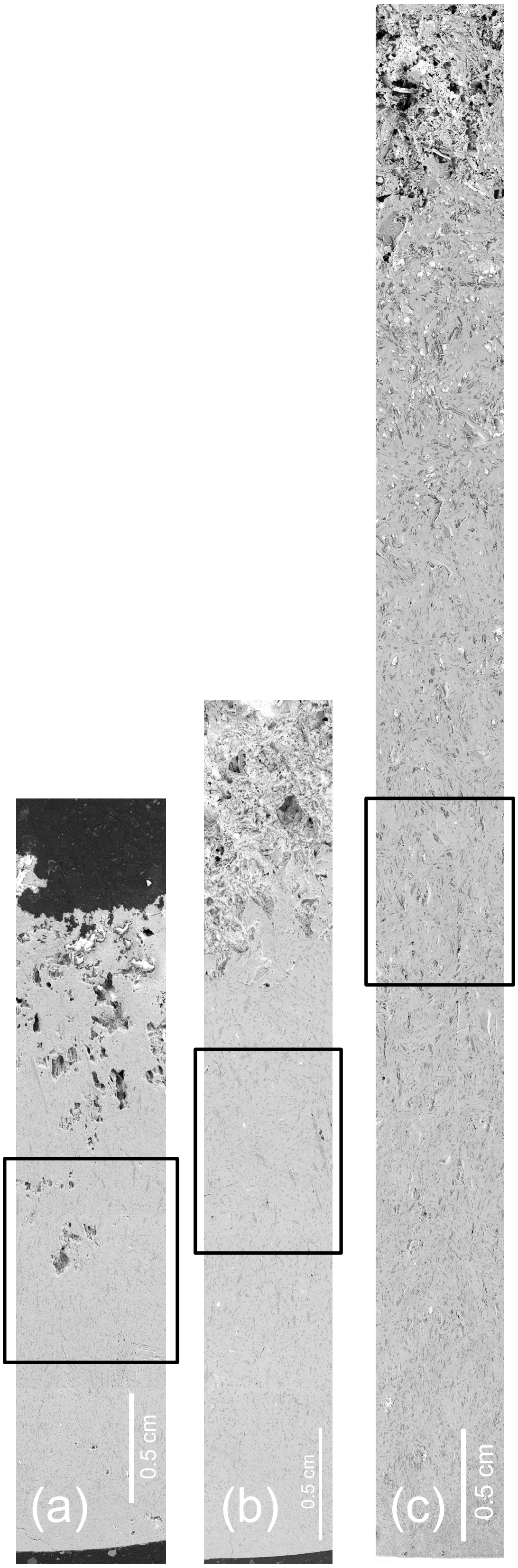

Figure 5.4 – SE SEM images compiled to a panorama of (a) half 5mm rod, (b) half 8mm rod and (c) half 15mm rod. Black rectangles highlight the position of the micrographs illustrated in Figure 5.5.

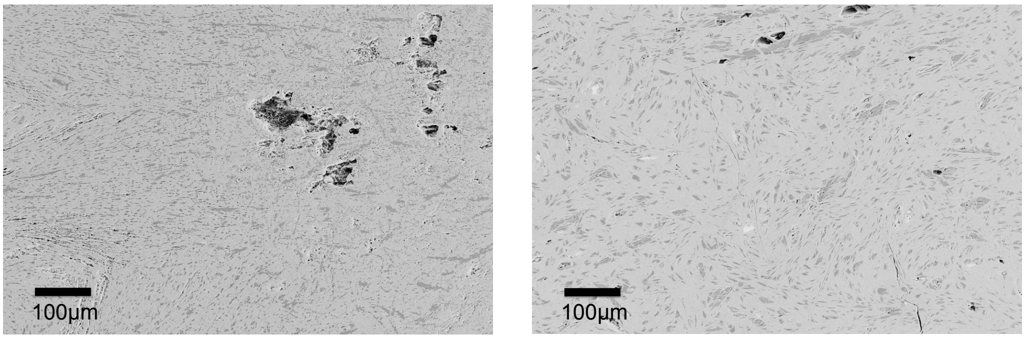

(a) Rod-5mm-0.200 **(b)** Rod-8mm-0.205

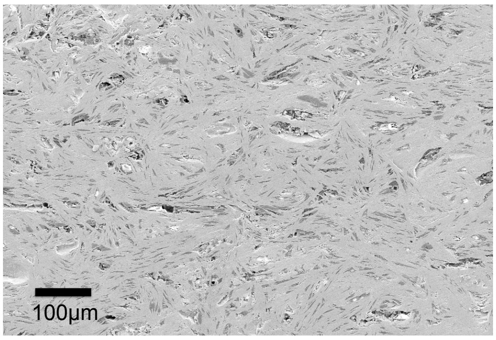

(c) Rod-15mm-0.203

Figure 5.5 – SE Scanning electron micrographs of (a) 5mm, (b) 8mm, and (c) 16mm rods taken on polished radial cross-sections.

EDX measurements (not shown) reveal that the large inclusions of 50μm-100μm are (Ca,Sr)CuO_2 phase while the small inclusions of ~10μm correspond to smaller (Ca,Sr)CuO_2 inclusions or (Ba,Sr)SO_4 inclusions. In the case of the 15-mm rod, an additional, Cu-free, second phase was detected with a mean composition close to $Bi_2(Ca,Sr)_3O_x$.

The phase identification was confirmed by collecting θ-2θ powder diffraction patterns on powders obtained by gently grinding pieces of the 5mm, 8mm, and 16mm rods. The three patterns are shown in Figure 5.6, where reflections marked by stars in the patterns of the 5mm and 16mm rods may correspond to the Cu-free phase evidenced by EDX. Rietveld refinements taking into account the two main phases Bi-2212 and (Ba,Sr)SO_4 result in the refined Bi-2212 cell parameters listed in Table 5.4. The a- and b- cell parameters are similar for the 5mm and 8mm rods and only slightly larger for the 15mm rod. More importantly, the evolution of the c-cell parameters is in agreement with the O content of the rods: c (rod 8mm)< c (rod 15mm)< c (rod 5mm). Bi-2212 phase volume proportions are similar in the 5mm (71%) and 8mm (72%) rods while this value is smaller in the 15mm rod (64%). The smaller amount of Bi-2212 in the 15mm rod is explained by a larger amount of second phases visible both in the rod panorama and on the diffraction pattern, where Bi-2212 reflections have smaller intensities compared to the 5mm and 8mm rods.

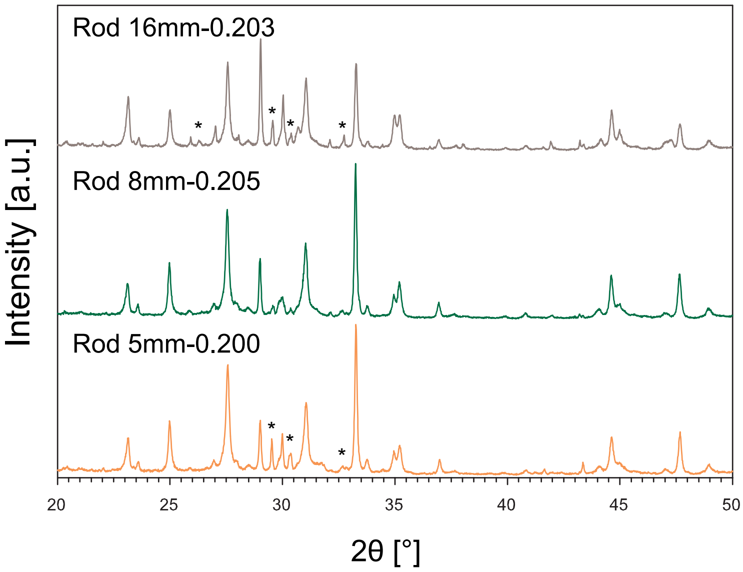

Figure 5.6 – θ-2θ powder diffraction patterns for 5mm, 8mm, and 15mm rods. The stars indicate the position of reflections probably due to the $Bi_2(Ca,Sr)_3O_x$ phase.

D8	**Bi-2212**			
Sample	a [Å]	b [Å]	c [Å]	Vol %
Rod-5mm-0.200	5.4143(8)	5.4140(5)	30.978(5)	71.4(2)%
Rod-8mm-0.205	5.4140(3)	5.4131(5)	30.967(2)	72.2(1)%
Rod-15mm-0.203	5.4195(4)	5.4176(3)	30.973(2)	63.6(2)%

Table 5.4 – Refined cell parameters and phase proportion of the Bi-2212 phase in the 5mm, 8mm, and 16mm rods from D8 powder data.

5.2.1.2 Texture

The texture of the 5mm and 15mm rod was only measured on the Inel diffractometer. Texture measurements were collected on 6mm-long sections cut from the rods (Figure 5.7). The samples were mounted with the Z direction (i.e., the rod axis) aligned with the Eulerian cradle rotation axis φ. X and Y are randomly positioned around Z since they are equivalent due to the cylindrical symmetry.

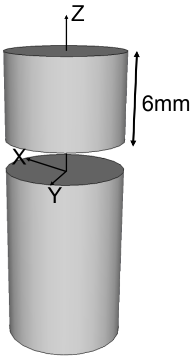

Figure 5.7 – Rods for diffraction measurement are cut in 6mm long small rods.

Data were refined with the MAUD program using the same procedure as for the tube (Section 3.5). The Bi-2212, (Ba,Sr)SO_4, and (Ca,Sr)CuO_2 phases were included in the refinement. {200}, {020}, and {00$\underline{10}$} normalized pole figures of the three rods are represented in Figure 5.8. All {00$\underline{10}$} pole figures reveal a fiber texture component with *c*-axes oriented along the rod axis. This <001>-fiber component is in agreement with the equatorial reinforcements visible on {200} and {020} pole figures. In the case of the 5mm rod, the <001>-fiber component is not perfectly aligned with the Z direction, as also visible on the {200} and {020} pole figures that are indeed shifted from the equator. This could result from an imperfect alignment of the small sample in the Inel cradle and/or a cross-section miscutting. The 15mm rod exhibits also a <010> fiber texture visible by a reinforcement on the equator of {00$\underline{10}$} and {200} pole figures and a reinforcement at the center of the {020} pole figure. PO index determinations performed on melt-cast processed rods at Nexans Superconductors R&D center using the procedure described in section 3.6.2.2 reveal that *c*-axes are preferentially not aligned with the radial direction of the rods. Such an observation is coherent with the absence of a reinforcement at the equator of the {00$\underline{10}$} pole figure for the 5mm and 8mm diameter rods.

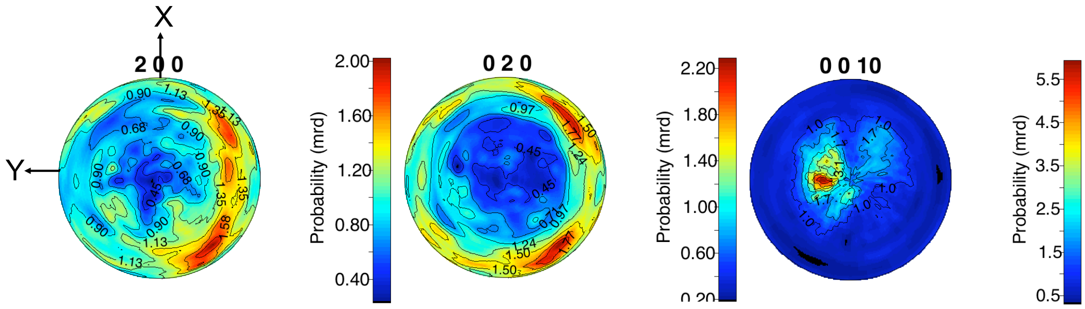

(a) Rod-5mm-0.200

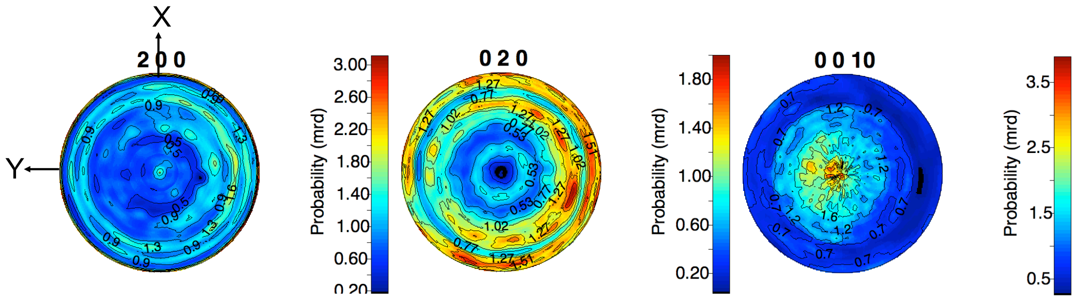

(b) Rod-8mm-0.205

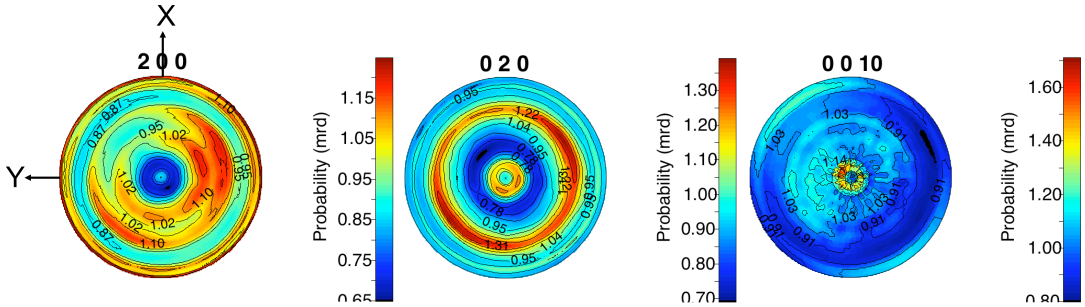

(c) Rod-15mm-0.203

Figure 5.8 – {200}, {020}, and $\{00\underline{10}\}$ normalized pole figures calculated from OD refinement for (a) 5mm, (b) 8mm, and (c) 15mm from Inel data.

5.2.2 8mm diameter rods with different oxygen contents

In order to investigate the effect of oxygen content, we selected three rods amongst the series of 8mm-diameter rods with different oxygen contents in Table 5.2: Rod-8mm-0.187, Rod-8mm-0.205 and Rod-8mm-0.230.

It is necessary to compare the microstructure and texture of these samples, because the second annealing along T-pO_2 trajectories can be done at temperatures as high as 800 ° and may cause some partial melting of the samples, thereby potentially modifying the microstructure and texture of the rods.

5.2.2.1 Microstructure

Figures 5.9 (a) to (c) present SEM micrographs of polished cross-section of the three 8mm rods. All rods have a similar microstructure with inclusions of (Ba,Sr)SO_4 and (Ca,Sr)CuO_2 second phases. It is visible on these micrographs that some inclusions of second phases have grown along the temperature gradient during the cooling step (i.e. along the radial direction).

A micrograph of the edge of Rod-8mm-0.230 is shown in Figure 5.9d. Some inclusions of second phases are smaller and in particular, (Ba,Sr)SO_4 inclusions are forming dendrites. Examples of dendrites are framed in the micrograph by black rectangles. Based on visual inspection, the post-annealing step during the manufacture of the rods in the range δ=0.187-0.230 does not seem to have affected the microstructure of the samples.

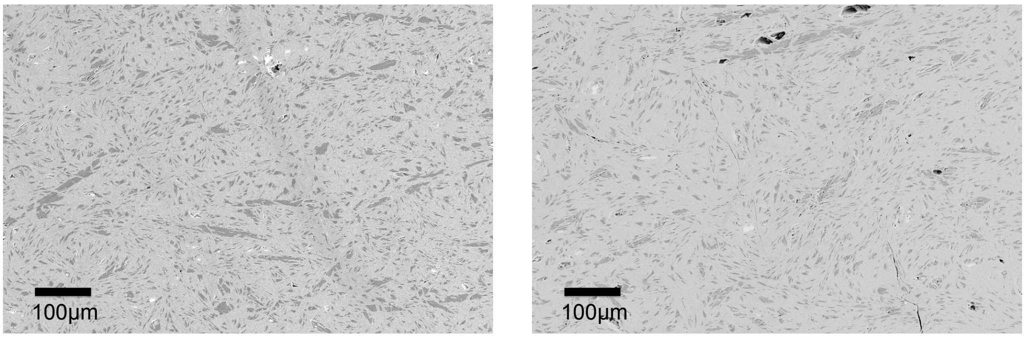

(a) Rod-8mm-0.187 **(b)** Rod-8mm-0.205

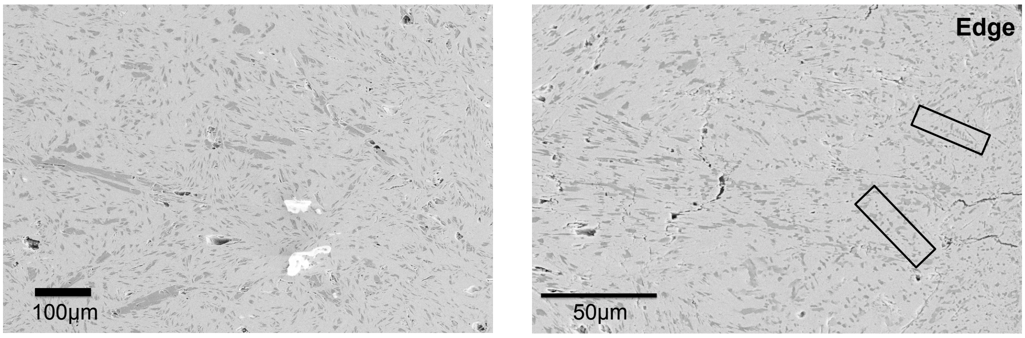

(c) Rod-8mm-0.230 **(d)** Rod-8mm-0.230 edge

Figure 5.9 – SE Scanning electron micrographs of three rods taken on polished radial cross-sections (a-c) at the center of the non porous region and (d) close to the edge.

The similarity of the phase content in the three rods is confirmed by the θ-2θ powder diffraction patterns collected on gently ground powder with the Bruker D8 diffractometer. The three patterns shown in Figure 5.10 have similar profiles and peak intensities. Rietveld refinements taking into account the two main phases Bi-2212 and (Ba,Sr)SO_4 result in the refined Bi-2212 cell parameters listed in Table 5.5. For all rods, a and b cell parameters vary of maximum 0.0014Å with the O content increase. The c-cell parameter decreases of 0.04Å with oxygen content increase. This decrease of the c-cell parameter is visible in the right part of Figure 5.10 by a shift of $00l$ reflections to higher 2θ values. Some authors [22] observed the same behavior and attributed it to a contraction of the Bi_2O_2 double layer when oxygen atoms are inserted in the Bi_2O_2-layer. Phase volume percentage of the Bi-2212 phase are similar in all rods.

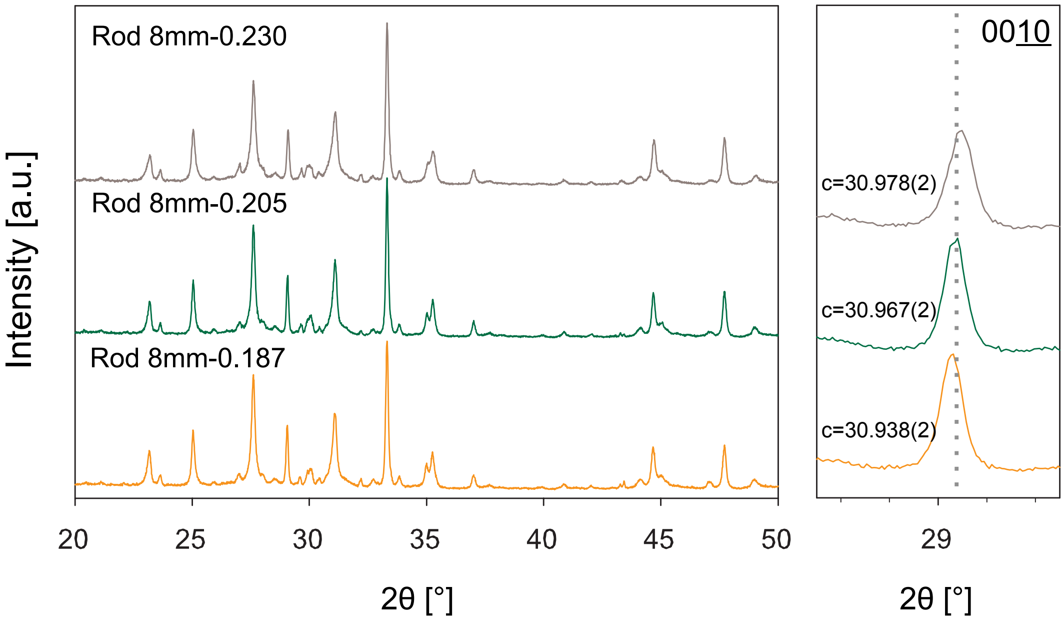

Figure 5.10 – The graph on the left is a θ-2θ powder diffraction pattern for 8mm rods with increasing oxygen content from bottom to top. The graph on the right is a zoom on the $00\underline{10}$ reflection showing the shift of the peak to high 2θ values when O content is increased (i.e. c is decreased).

D8	**Bi-2212**			
Sample	a [Å]	b [Å]	c [Å]	Vol %
Rod-8mm-0.187	5.4145(7)	5.4129(4)	30.978(2)	73.0(2)
Rod-8mm-0.205	5.4143(8)	5.4131(5)	30.967(2)	72.2(1)
Rod-8mm-0.230	5.4136(8)	5.4117(4)	30.938(2)	72.9(9)

Table 5.5 – Refined cell parameters and phase proportion of the Bi-2212 phase in the 8mm rods from D8 powder data.

5.2.2.2 Texture

Rod textures were characterized on 6mm long samples (See Figure 5.7) using the D1B line at ILL according to the procedure described in details in Section 3.3.2. As for the rods in the previous section, the Z direction was aligned with the Eulerian cradle rotation axis φ. Data were refined in the MAUD program the same way as was done for the tube (Section 3.5) using Bi-2212 and (Ba,Sr)SO_4 phases in the refinement. The GoF and R_{wp} of the refinement are presented in Table 5.6 and are similar for all rods. {200}, {020}, and {00$\underline{10}$} normalized pole figures of the three rods are represented in Figure 5.11. All {00$\underline{10}$} pole figures reveal a fiber texture component with *c*-axes oriented along the rod axis with a distribution of ~ 40°. This <001>-fiber component is in agreeement with the equatorial reinforcements, also having a large distribution, visible on {200} and {020} pole figures. For rods Rod-8mm-0.187 and Rod-8mm-0.230, other texture components with a and *b*-axes preferentially oriented along Z are seen while for the Rod-8mm-0.205 rod, only *a*-axes are preferentially oriented along Z. As observed in Chapter 3 for the tube, textures are weak with maxima of OD not larger than 3.5 m.r.d. observed for the Rod-8mm-0.205 rod.

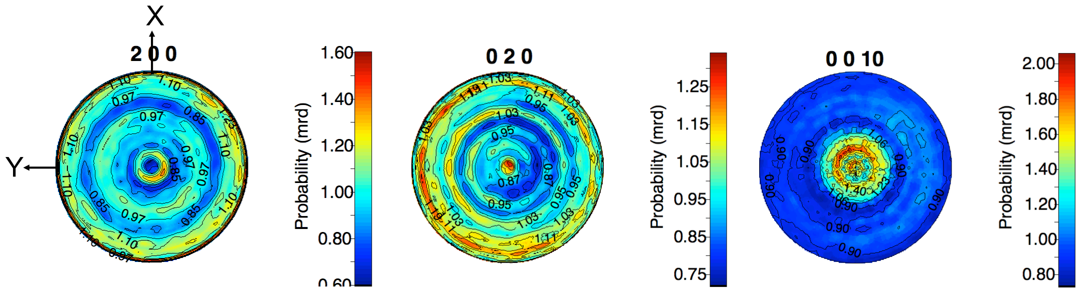

(a) Rod-8mm-0.187

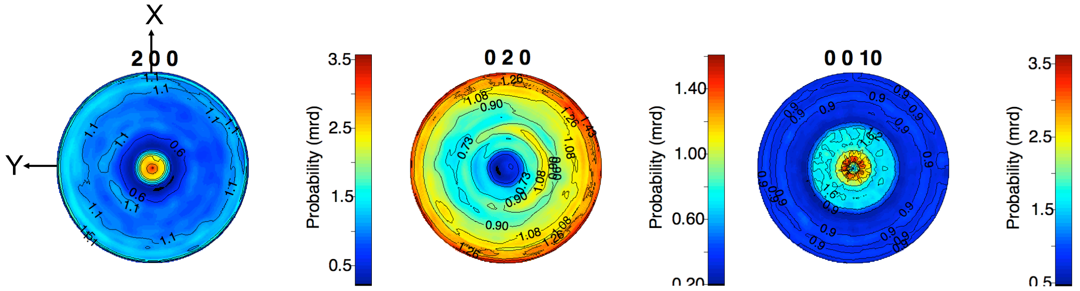

(b) Rod-8mm-0.205

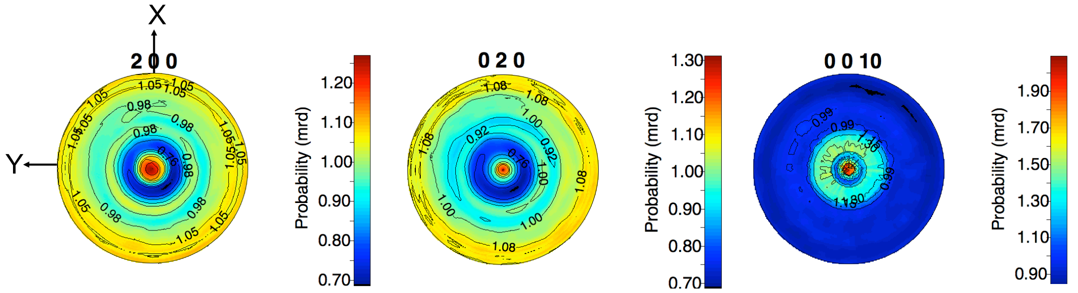

(c) Rod-8mm-0.230

Figure 5.11 – {200}, {020}, and {00$\underline{10}$} normalized pole figures calculated from OD refinement for 8mm rods from D1B data.

Sample	GoF	R$_{wp}$ [%]
Rod-8mm-0.187	1.23	10.73
Rod-8mm-0.205	1.26	11.72
Rod-8mm-0.230	1.30	11.75

Table 5.6 – Refinement data for rods 8mm-D1B.

5.3 Physical properties

5.3.1 Physical properties of rods with different diameters

The magnetic field dependence of magnetization at 4.2K was measured on small cubes cut from the three rods. For all rods, the cubes were oriented with the direction along the rod axis parallel to the applied magnetic field. The weight and dimensions of all samples are listed in Table 5.7. The samples for DC magnetization loops measurement as a function of the applied magnetic field were ZFC till 4.2K. Magnetic field was applied from 0 to +H_x, +H_x to -H_x and -H_x to H_y. H_x being the magnetic field necessary to overcome irreversibility field or maximum value reachable in the SQUID (i.e. 50000Oe) and H_y being a value of field higher than full penetration field (H_p, defined where the first magnetization curve meets the complete cycle). Half of the M(H) hysteresis are plotted in Figure 5.12. All M(H) curves are in the same range of magnitude. The 5mm rod shows the smallest ΔM while the 15mm rod shows the highest ΔM.

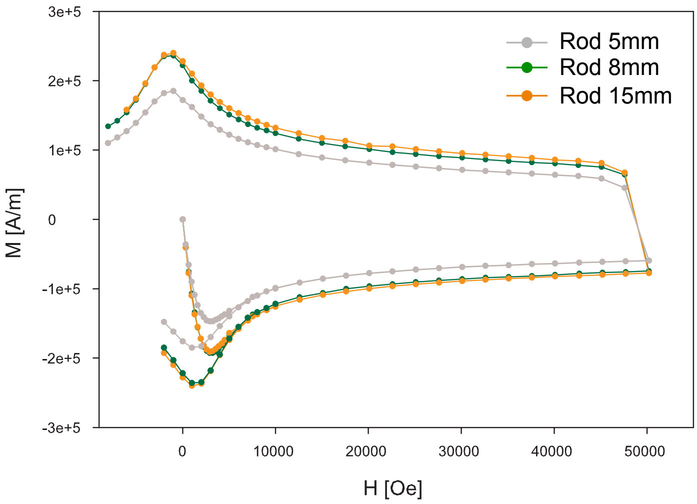

Figure 5.12 – dc magnetization loops as a function of applied magnetic field at T=4.2K for 5mm, 8mm, and 16mm rods.

		Size of the samples		
Sample	**Weight [g]**	**l1 [mm]**	**l2 [mm]**	**l3 [mm]**
Rod 5mm	0.0061	1.02	1.03	1.00
Rod 8mm	0.0053	0.91	0.98	1.00
Rod 15mm	0.0075	1.00	1.10	1.16

Table 5.7 – Weight and dimensions of the samples cut from the rods and used for M(H) measurements. l1 is the length along the rod radius.

5.3.2 Physical properties of rods with various oxygen content

Samples used for magnetization measurements were 5mm diameter rods with dimensions close to R (radius)=2.5mm and L (length)=5mm. See Table 5.8 for exact dimensions of each sample. Magnetization measurements were done in a PPMS with the applied magnetic field (Ha) parallel to rod axis. Two different kinds of measurements were done: (i) magnetization measurement as a function of temperature, M(T) and (ii) magnetization measurement as a function of applied magnetic field, M(H). For M(T) measurements, the samples were Zero-Field-Cooled (ZFC) till 30K. Then the applied magnetic field was set to 10 Oe and temperature was increased at 2K/min to 110 K while measuring magnetization averaged over every 1K. Magnetization loops measurements were done as describe in Section 5.3.1.

Rod name	**Oxygen content ($O_{8+\delta}$)**	**Length [mm]**	**Volume [cm^3]**	**Mass [g]**
Rod-5mm-0.175	δ=0.175	5.01	0.098	0.5529
Rod-5mm-0.180	δ=0.180	5.05	0.099	0.5624
Rod-5mm-0.185	δ=0.185	5.09	0.100	0.5634
Rod-5mm-0.190	δ=0.190	5.07	0.099	0.5639
Rod-5mm-0.200	δ=0.200	5.15	0.101	0.5592
Rod-5mm-0.210	δ=0.210	5.14	0.109	0.5571
Rod-5mm-0.219	δ=0.219	5.01	0.098	0.5479
Rod-5mm-0.225	δ=0.225	5.02	0.099	0.5535
Rod-5mm-0.232	δ=0.232	5.07	0.099	0.5536
Rod-5mm-0.240	δ=0.240	5.22	0.102	0.5777
Rod-5mm-0.245	δ=0.245	5.02	0.099	0.5563
Rod-5mm-0.248	δ=0.248	5.04	0.099	0.5672
Rod-5mm-0.252	δ=0.252	5.04	0.099	0.5516

Table 5.8 – Characteristics of the 5mm rods used for physical properties measurements.

5.3.2.1 Temperature dependence of magnetization

Temperature dependance of magnetization M(T) plots for 5mm diameter rods with different oxygen contents (δ) in $Bi_2Sr_2CaCu_2O_{8+\delta}$ are regrouped in Figure 5.13. The T_c of each sample has been determined from these curves. T_c is the temperature at which superconducting transition starts, i.e. where M starts to decrease. An example of T_c determination is given in Figure 5.13. T_c's versus δ are represented in Figure 5.14 for all 5mm diameter rods. T_c's versus δ curve has a bell-shaped as expected from results observed in literature [51, 54–56, 60, 64, 123]. The maximum T_c of 97K is observed for values of O content δ comprised between 0.180 and 0.185. For all samples, transitions are broad, likely due to Bi2201 intergrowths, or other second phases and voids. [124]

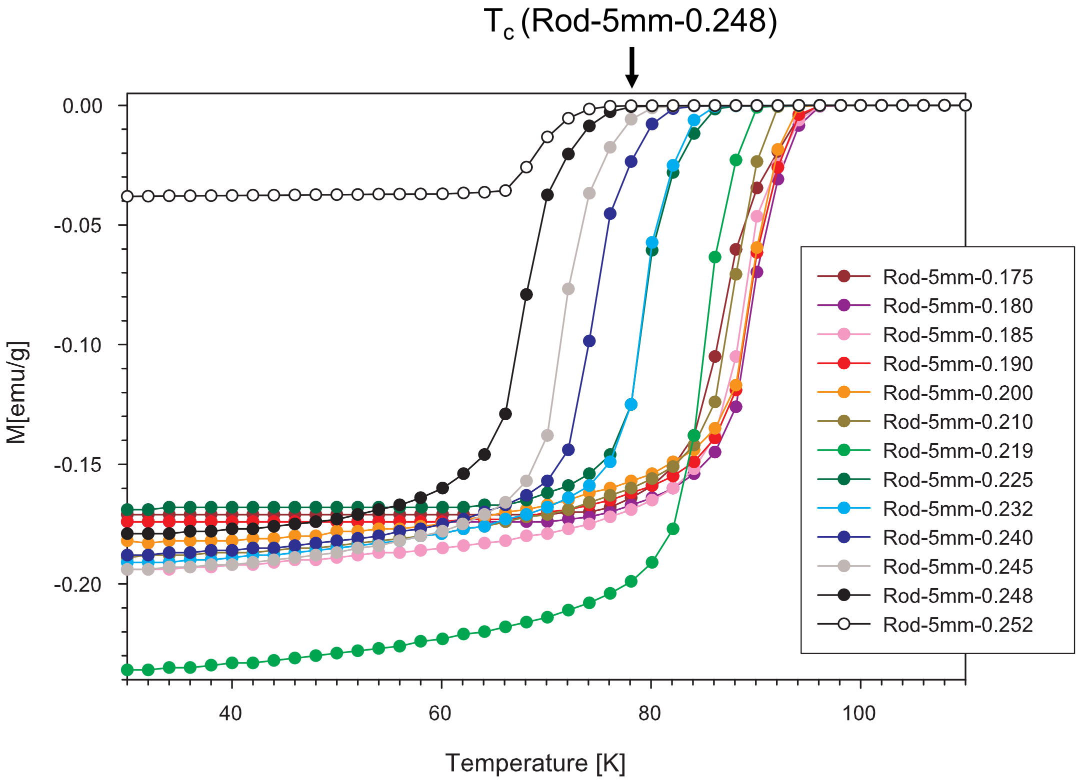

Figure 5.13 – Temperature dependence of magnetization for 5mm diameter rods with different O contents δ ($Bi_2Sr_2CaCu_2O_{8+\delta}$). T_c is determined in M(T) curves as the temperature at which M starts to decrease as represented by the arrow for the black curve.

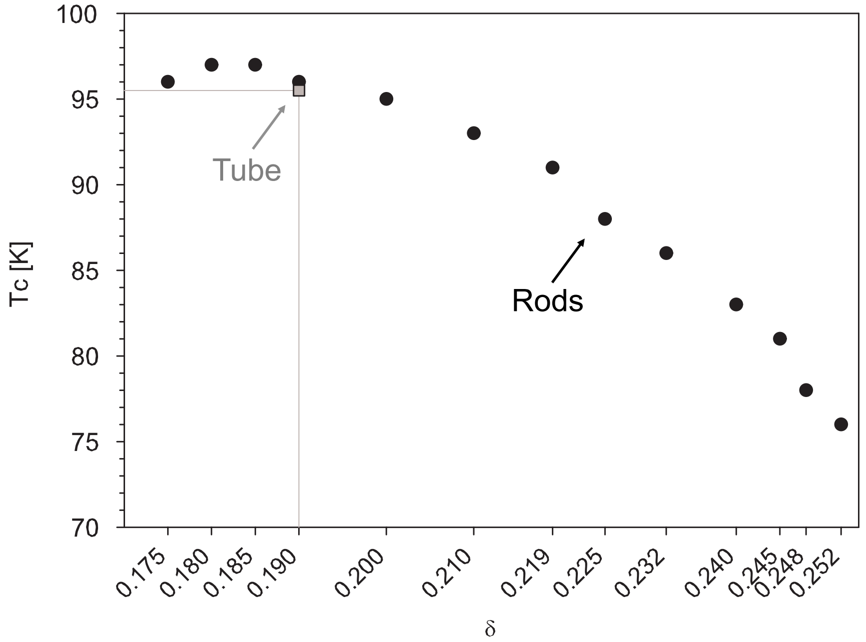

Figure 5.14 – T_c variation of (●) 5mm diameter rods with different O contents δ ($Bi_2Sr_2CaCu_2O_{8+\delta}$) and (■) value measured for the tube.

5.3.2.2 Field dependence of magnetization

Figure 5.15 shows magnetization loops for all 5mm diameter rods measured at 4.2K. J_c values may be obtained from these magnetization measurements. The width ΔM of the M(H) hysteresis loop is used to calculate J_c using: [125]

$$J_c = \frac{\Delta M}{d} \tag{5.1}$$

where d is a length characteristic of the sample size and geometry; for an infinite cylinder of radius R (for short cylinders with finite aspect ratio ~ 1, numerical modeling results [125] have shown that this formula can still be used as a very good approximation provided the full-penetration field is exceeded):

$$J_c = \frac{3\Delta M}{2R} \tag{5.2}$$

With ΔM in [A/m] and R=rod radius in [m].

ΔM corresponds to the width of the hysteresis loop took between the full penetration field (H_p) and the irreversibility field (H_{irr}) as illustrated in Figure 5.16. An example of J_c calculation is provided for information. Fluctuations are observed on the top of three M(H) curves corresponding to Rod-5mm-0.232,0.240, and 0.245 plots. These fluctuations are called flux jump and may occur at low temperatures when magnetization is locally high. [126,127] This phenomenon is beyond the scope of this thesis and won't be deeper discussed.

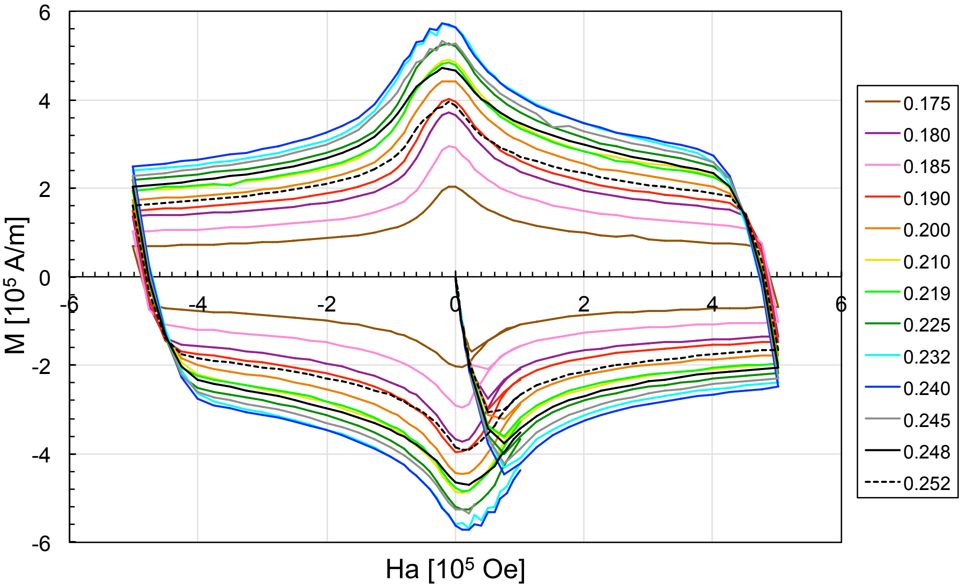

Figure 5.15 – dc magnetization loops as a function of applied magnetic field at T=4.2K for 5mm diameter rods with different O contents δ ($Bi_2Sr_2CaCu_2O_{8+\delta}$).

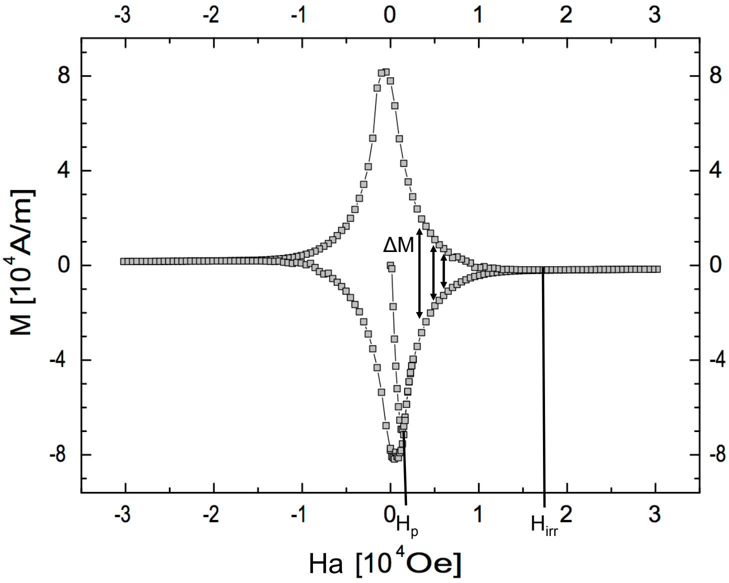

Figure 5.16 – Determination of ΔM in M(H) curve (the line is a guide for the eyes).

Figure 5.17 shows J_c versus magnetic field for sample rod-5mm-0.210 at temperatures ranging from 4.2K to 85K. At T=4K, 10K, and 20K, J_c does not decrease to 0, as H_{irr} is higher than 50 kOe, the limit of the instrument. With increasing temperature above 30K, J_c decreases rapidly with H_a. H_{irr} decreases with increasing temperature as follows: H_{irr} is about 30 kOe at 30K, 15 kOe at 40K and close to 3 kOe at 60K.

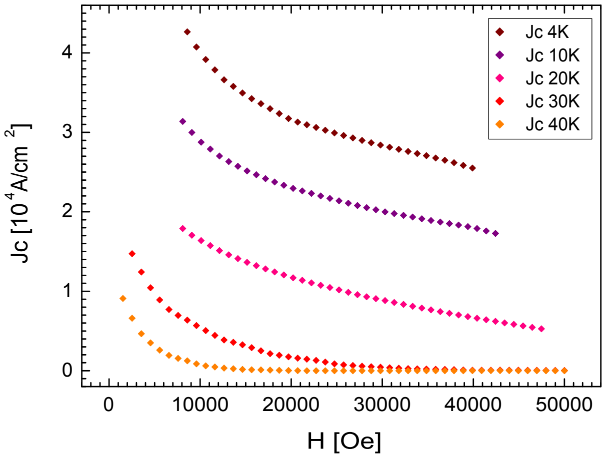

(a) T=4K, 10K, 20K, 30K, and 40K

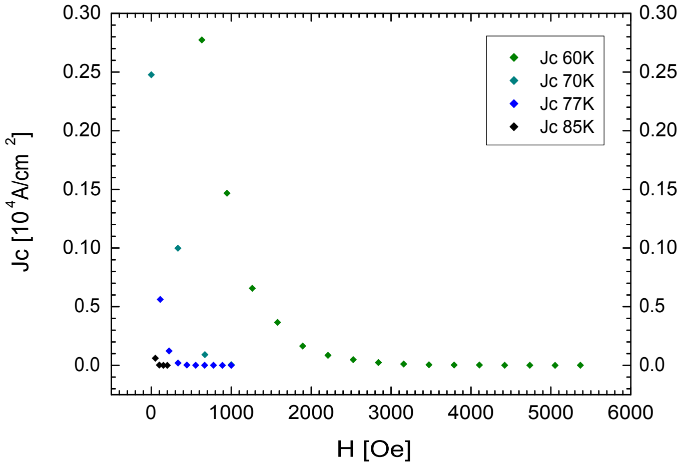

(b) T=60K, 70K, 77K, and 85K

Figure 5.17 – J_c vs H_a for Rod-5mm-0.210 at different temperatures.

Figure 5.18 shows the decrease of J_c with the applied magnetic field for all 5mm diameter rods at 4.2K. These results are plotted differently in Figure 5.19 to highlight the evolution of J_c with increasing oxygen content in 5mm diameter rods at 4.2K. J_c increases till a maximum value at δ=0.240 and then decreases abruptly. This behavior is observed for all values of applied magnetic field.

Best J_c's of all are attained in sample Rod-5mm-0.240. J_c reaches an approximate value of 5.10^4A/cm^2 at 4.2K for applied field close to H_p at 10000Oe. The magnitude of J_c is comparable to the one observed in thick films [128] (See Table 5.9) and 10 to 100 times higher to values observed on other Bi-2212 rods at 4.2K [117, 129]. Technological applications require to reach high J_c values. Depending on the application temperature, the optimal sample will differ, to illustrate this statement, the δ value corresponding to maximum J_c for temperatures of 4.2K, 40K, and 77K are plotted in Figure 5.20. At the temperature of liquid Helium (4.2K), the sample having the highest J_c is the Rod-5mm-0.240 with an oxygen content of 8.240. At the temperature of liquid Nitrogen (77K), best J_c's are reached in the Rod-5mm-0.200 sample having a lower oxygen content (J_c vs. H curves are presented in Figure 5.21).

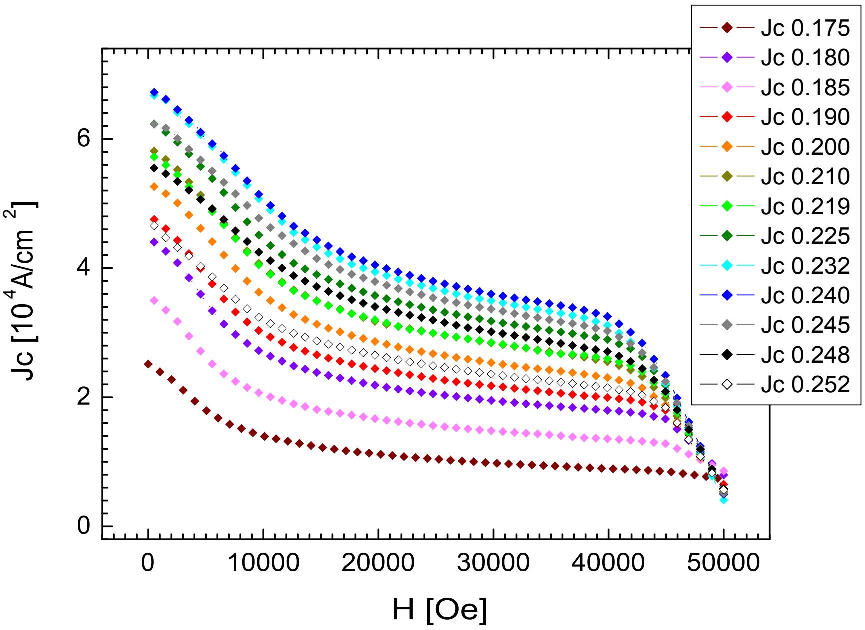

Figure 5.18 – Decrease of J_c with applied magnetic field H_a for all 5mm diameter rods at 4.2K.

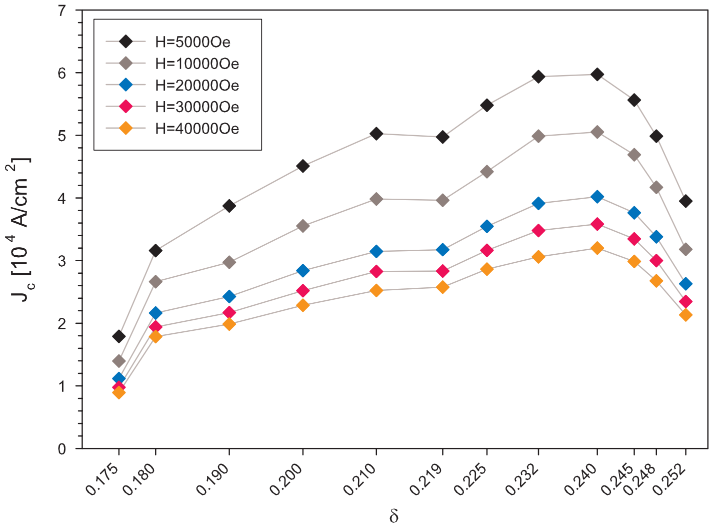

Figure 5.19 – Evolution of J_c with 5mm diameter rods O content δ ($Bi_2Sr_2CaCu_2O_{8+\delta}$) at 4.2K for different applied magnetic field H_a (the lines are guides for the eye).

Authors	Bi-2212 sample	J_c
H Miao et al. [129]	1.8mm diameter rod	3600A/cm^2 at 77K
Kim et al. [117]	1.0mm diameter rod	800A/cm^2 at 77K
Kim et al. [117]	1.6mm diameter rod	800A/cm^2 at 77K
Cecchetti et al. [128]	Bi-2212/Ag thick films	7.10^4 A/cm^2 at 4.2K
Hayashi et al. [130]	Single crystal	1.8.10^6 A/cm^2 at 4.2K

Table 5.9 – Values of J_c found in the literature.

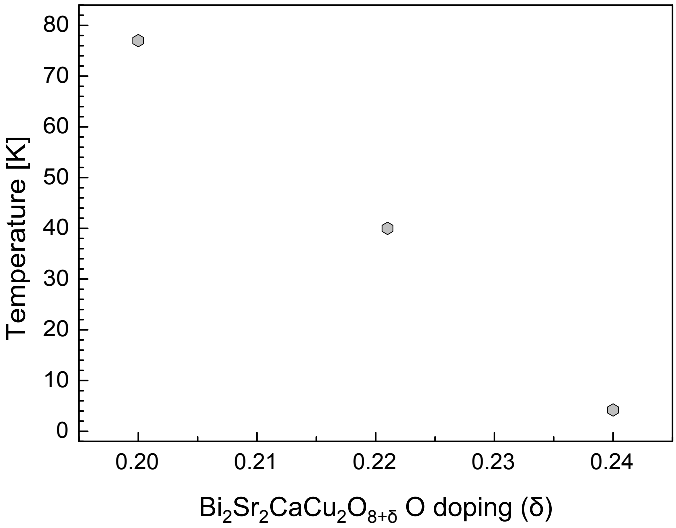

Figure 5.20 – Value of δ associated to the maximum value of J_c for each temperature.

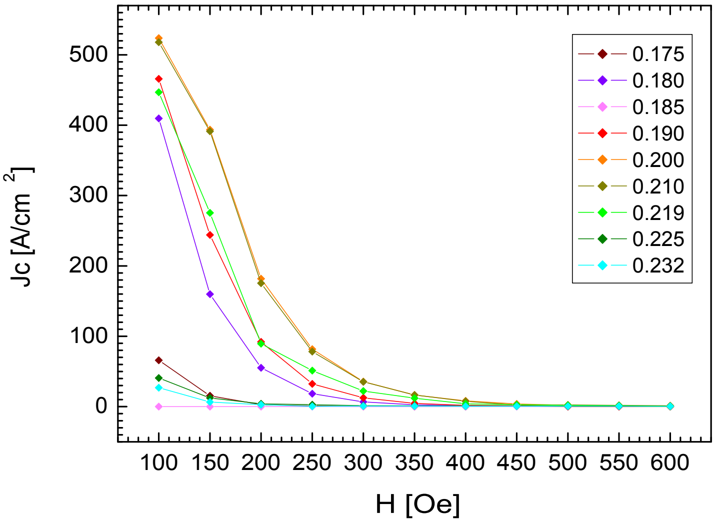

Figure 5.21 – Decrease of J_c with applied magnetic field H_a for all 5mm diameter rods at 77K.

5.4 Conclusion

This chapter was devoted to the study of melt-cast processed rods with different diameters of oxygen contents. First, rods with diameters of 5, 8 or 15 mm were compared in terms of microstructure, texture and physical properties. Microstructure results suggest that the 8 mm rod contains the lowest amount of second phase inclusions. EDX measurements evidenced the presence of $(Ba,Sr)SO_4$ and $(Ca,Sr)CuO_2$, and in addition, a Cu-free phase, close to the composition $Bi_2(Ca,Sr)_3O_x$. In all rods, it appeared that the second phase grains tend to align with the temperature gradient occurring upon cooling, i.e. along the radial direction. Texture components refined from Inel data include in all cases a <001>-fiber component with *c*-axes along the rod axis.

The control of the oxygen content in the melt-cast processed samples is achieved through T-pO_2 post-annealing treatment. These treatments are designed so that the microstructure and texture should not be affected. This was verified in 8mm diameter rods using D1B data and it was found that all investigated rods show texture components with *c*-axes, *a*-axes and sometimes *b*-axes oriented along the rod axis. As for the tube in Chapter 3, the texture strengths are weak, with maxima of OD not higher than 3.5 m.r.d.

The textures obtained from the full texture analysis of all rods are compatible with the PO index determinations performed on melt-cast processed rods at Nexans Superconductors R&D center. Using the procedure described in section 3.6.2.2, the PO index determination indicates that *c*-axes are preferentially not aligned with the radial direction of the rods. Such an observation is coherent with the absence of a reinforcement at the equator in the $\{00\underline{10}\}$ pole figures. Additional insight might be gained by combining the sequential polishing used at Nexans Superconductors and full texture characterization with the Inel diffractometer.

Although the texture results were obtained for 8mm diameter rods, it seems reasonable to expect that the 5mm diameter rods can be considered to have similar textures for different oxygen contents. M(T) and M(H) curves were compared on a series of 5mm rods carefully annealed to adjust the oxygen content in these rods. The critical temperature is highly affected by the oxygen doping and has a parabolic shape as a function of the δ value. Maximum T_c was observed in a range of δ=0.180-0.185. There is also a dependence of J_c (deduced from the M(H) curves) as a function of the oxygen content. The maximum J_c measured in these 5mm rods is around 6.10^4 A/cm^2 at 4.2K. The optimum oxygen content for maximum J_c depends on the temperature and moves from small O content to higher O content when decreasing temperature.

CHAPTER 6 | *Relation between texture and physical properties*

In this chapter, we demonstrate the use of the geometric mean of tensor properties averaged over crystallographic orientation distributions, to simulate anisotropic resistivity tensors of the Bi-2212 phase in the normal state. The orientation distributions are measured using neutron diffraction. This methodology is applied to melt-cast processed samples and evaluates the contribution of textural effects to the resulting anisotropy. The calculated tensor compares well with measured macroscopic resistivity tensors and shows that low texture strengths in such materials does not necessarily result in catastrophic effects on macroscopic conducting paths. This chapter is presented with an article layout as it is meant for publication.

Chapter content

6.1 Introduction

$Bi_2Sr_2CaCu_2O_{8+\delta}$ (Bi-2212) high-temperature superconductor has received a lot of interests because of its very large electro-magnetic anisotropy, supported by a very strong crystallographic two-dimensionality. It has been reported that Bi-2212 single crystals develop up to normal state electrical resistivity anisotropy ratio up to $\rho_c/\rho_{ab} = 10^4$-10^5 [51, 131], while the in-plane anisotropy is much smaller and does not exceed $\rho_b/\rho_a = 2.9$ [132] from T_c up to 300K, this latter anisotropy decreasing for out-of cation stoichiometric compositions. Bi-2212 also develops large critical current densities (J_c) up to relatively large magnetic fields at low temperatures [133], considered as a consequence of an enhanced condensation energy in this temperature range [134]. Z. Mori et al. [135] showed in Bi-2212 thin films deposited on $SrTiO_3$ single crystals that crystal grain boundaries act as weak links for current transport. They reported a difference of two orders of magnitude between intra-grain J_c (10^5 A/cm^2) and inter-grain J_c (10^3 A/cm^2) for a 24° tilt angle between two grains, an effect even more pronounced than for $YBa_2Cu_3O_7$ as measured by Dimos et al. [136]. However, Bi-2212 samples containing both inter- and intra-grain boundaries can still exhibit rather unexpectedly large J_c-values whose origin is till unclear, particularly in view of the low texture levels achieved in bulk samples. Among the extensive literature concerning bulk samples, the so-called melt-cast processed $Bi_2Sr_2CaCu_2O_{8+\delta}$ (Bi-2212) bulk materials exhibit intriguingly large critical current densities of J_c (77K)=4 kA/cm^2 [70], while their crystallographic textures are close to random values. In order to approach some explanation for this apparently strange behavior, we decided in this work to concentrate our calculations on the resistivity anisotropy in the normal state of such samples, keeping in mind that a metallic character still appears as a prerequisite to achieve reasonable carrier capabilities at the superconducting state. We simulate the macroscopic normal state electrical resistivity tensor ρ_{ij}^M from (i) the experimentally determined Orientation Distribution Functions (ODF) and (ii) literature experimental data for the single crystal resistivity tensor ρ_{ij}. We use for this purpose geometric mean tensor calculations, to show that melt-cast samples resistivity keeps a significant anisotropic character in such samples. This approach demonstrates why interesting well developed conducting properties can be expected even with low orientation degrees when strong anisotropy is intrinsically present.

ODF-weighted ρ_{ij}^M simulations

For perfectly randomly oriented samples with theoretical density, the calculation of macroscopic properties is usually simply operated through an arithmetic mean, T^M = <T>, of the intrinsic (single crystal) property tensor T. However such averages do not result necessarily in macroscopic property tensor homogeneity. For instance, in the case of elastic stiffness, C$_{ijkl}$, and compliance, S$_{ijkl}$, tensors, the necessary condition for homogeneity or invertibility [134], $C_{ijkl}^M = <C_{ijkl}> = <C_{ijkl}^{-1}>^{-1} = (S_{ijkl}^M)^{-1}$, is not fulfilled. This gives rise to the so-called Voigt [137] and Reuss [138] averages for $<C_{ijkl}>$ and $<S_{ijkl}>$ in which strain and stress homogeneities in all the crystals are respectively assumed, but not simultaneously. Matthies and Humbert [139] showed that in this case the Geometric Mean Average (GMA, noted [T]) resulted in homogeneous properties, coherent with visco-plastic self-consistent approaches, even for textured polycrystals. Similarly, for resistivity tensors of textured polycrystals, electric field and current density homogeneity cannot be imposed simultaneously for all crystals using arithmetic averaging, and GMA can be applied to ensure the macroscopic homogeneity for resistivity and conductivity tensors: $\rho_{ij}^M = [\rho_{ij}] = [\rho_{ij}^{-1}]^{-1} = (\sigma_{ij}^M)^{-1}$ Since ρ_{ij} is a tensor, the calculation of its geometric average over crystallite orientations requires some more details. The macroscopic resistivity tensor of the textured polycrystal (with an Orientation Distribution Function of its crystallites given by the ODF, or f(g), g being a set of three Euler angles for the orientation variable relating crystal and sample reference frames [95]) is obtained from:

$$\rho_{ij}^M = \exp(< ln\rho >_{i'j'}) \tag{6.1}$$

$$= \exp\left[< \theta >_{ij,i'j'} (\ln\rho)_{i'j'}\right] \tag{6.2}$$

With

$$\langle\Theta\rangle_{ij,i'j'} = \int_g \Theta_i^{i'}(g)\Theta_j^{j'}(g)f(g)dg \tag{6.3}$$

and $(\ln\rho)_{i'j'}$ given by:

$$(\ln\rho)_{i',j'} = \sum_{\lambda=1}^{3} \ln(\rho^{(\lambda)})\mathbf{b}_i^{(\lambda)}\mathbf{b}_j^{(\lambda)} \tag{6.4}$$

$$= \ln\left[\prod_{\lambda=1}^{3}(\rho^{(\lambda)})^{\mathbf{b}_i^{(\lambda)}\mathbf{b}_j^{(\lambda)}}\right] \tag{6.5}$$

where the (λ) exponents denote eigenvalues of the corresponding quantities, and the $b_{ij}^{(\lambda)}$ are the eigentensors resulting from diagonalisation of the arithmetic average $\langle\ln\rho\rangle_{i'j'}$ for the oriented polycrystal [140]. The two successive tensor transformations $\Theta_i^{i'}$ relate to the 2nd order resistivity tensor character. The factorial entering the calculation explains the term "geometric mean", in the sense that the oriented polycrystal macroscopic resistivity is obtained by the mean averaging of the single crystal resistivity eigenvalues. Similar expressions could be obtained for the macroscopic conductivity tensor σ_{ij}^{M} which admits as eigenvalues $\sigma^{(\lambda)} = 1/\rho^{(\lambda)}$ the reciprocal of the resistivity eigenvalues. This warrants that the same macroscopic electrical properties are calculated either using resistivity or conductivity in the GMA approach. In other words, the average of the inverse macroscopic property is consistent with the inverse of the average macroscopic property. In this work we considered for all diffraction analyses an orthorhombic Bi-2212 phase (N°1000285 from the Crystallographic Open Database [141]) with cell parameters a=5.4054Å, b=5.4016Å, and c=30.7152Å. A crystal with orthorhombic point group symmetry exhibits only 3 independent resistivity components, ρ_{11}, ρ_{22} and ρ_{33}. However all single crystal studies on Bi-2212 indicate a small in-plane anisotropy, and we will neglect it in the property tensors, considering Bi-2212 as tetragonal with $\rho_{11}=\rho_{22}$ and taking the values determined by Watanabe et al. [51] (ρ_{22} = XX and ρ_{33} = YY). Weighting of ρ_{ij}^{M} over crystallite orientations is operated using the refined ODF f(g), which is determined experimentally from a set of diffraction pole figures $P_h(\mathbf{y})$ through inversion of the fundamental equation of quantitative texture analysis:

$$P_{\mathbf{h}}(\mathbf{y}) = \frac{1}{2\pi} \int_{\mathbf{h}//\mathbf{y}} f(g) d\tilde{\varphi} \tag{6.6}$$

Here h=<hk*l*>* stands for one family of diffracting planes, $\mathbf{y}$ their orientation in the sample reference frame, linked to the diffractometer angles, and $\tilde{\varphi}$ an integration path to obtain the pole figures from $f(g)$. The inversion of this equation to refine $f(g)$ is operated by entropy maximization using the E-WIMV iterative algorithm [84].

6.2 Experimental

We studied two melt-cast processed Bi-2212 samples, with tube and plain cylinder (rod) shapes. The tube sample has inner and outer diameters of 35mm and 50mm respectively, and the rod has a diameter of 8mm. Sample reference frames for both samples are defined with a Z axis along the long sample axis, i.e. cylindrical axis of symmetry. For the tube, the X axis is tangent to the surface and Y is the radial direction, while for the rod X and Y are symmetrically equivalent radial directions (Figure 6.5 insets).

For texture measurements a cylindrical core was drilled along the radial Y tube axis, resulting in a 7mm long cylinder, while a 6mm long cylinder was cut along the Z rod axis. In order to probe the whole cylinder volume and ensure comparable volume probing between texture and resistivity measurements, texture experiments were carried out using neutron diffraction at the D1B beamline of the ILL-Grenoble, in transmission mode with the 4-circles diffractometer and CPS detector. We used a regular grid of 5°x5° in χ and φ with 0°≤ χ ≤90° and 0°≤ φ ≤355° at an ω angle of 44.95° to cover as much as possible the center of all the important pole figures [89]. The tube core was oriented on the diffractometer with its Y axis parallel to the φ goniometer axis (Figure 6.1a) and its Z axis aligned with the χ goniometer axis (at φ=0). For the rod, only the Z direction was imposed to be aligned with φ, X and Y being randomly positioned around Z. Diffraction data were analyzed within the Combined Analysis frame [89] using the MAUD software [88].

The anisotropy of the resistivity was determined from resistivity measurements on 1x1x7mm^3 parallelepiped specimens by the four-probe technique on a PPMS 14T from Quantum Design. The tube specimens were cut with the longest dimension parallel to X, Y and Z directions, while for the rod only the Z and one radial direction were used (Figure 6.5 insets). A current of 5 mA was injected in the specimens and the resulting tensions were measured at temperatures ranging from 300K to 70K at 0T.

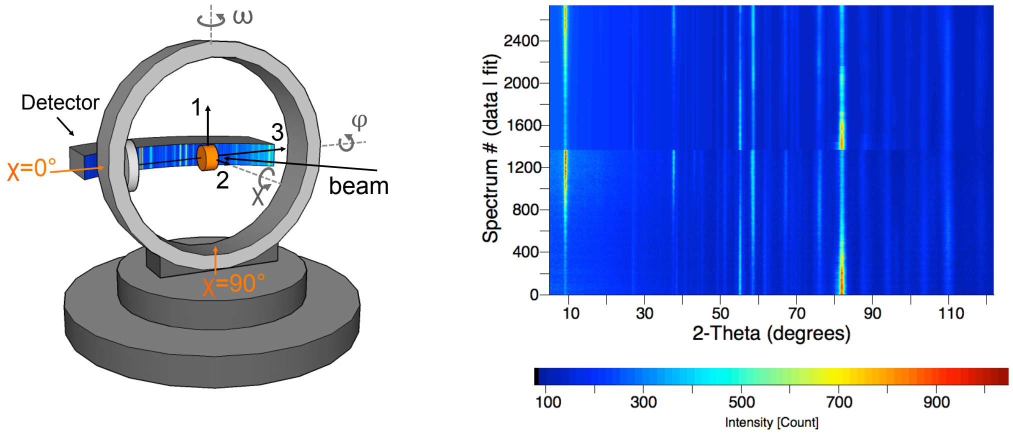

(a) (b)

Figure 6.1 – (a) Neutron diffractometer schematics for texture experiments. The samples (orange) are mounted with the corresponding orientations: tube, 1=X; 2=Z; 3=Y, and rod, 3=Z, X and Y at random in the (1,2) plane. (b) corresponding set of measured (bottom) and refined (top) diffraction diagrams showing the quality of the Rietveld fit. 2θ: horizontal axis, each (χ, φ) diagram is superposed along the vertical axis.

6.3 Results and discussions

The refinements converge with reasonable reliability factors and goodness of fit values (Rwp = 10.98; GoF = 1.47; Figure 6.1b), and result in unit-cell parameters of a=5.38614(5)Å, b=5.40580(5)Å, and c=30.8946(3)Åfor the tube and a=5.3716(1)Å, b=5.39440(9)Å, and c=30.7374(3)Åfor the rod. The deviation of a, b, and c from their initial values indicate some non-stoichiometric composition of the Bi-2212 phase in our bulks. The average elemental ratio for the Bi-2212 phase as obtained from EDX measurements is close to $\mathrm{Bi_{2.26}Sr_{2.25}Ca_{0.71}Cu_{1.78}O_{8+\delta}}$. We also observed $\mathrm{(Ba_{0.13}Sr_{0.87})SO_4}$ and $\mathrm{(Sr_{0.6}Ca_{0.4})CuO_2}$ as second phases. The larger c cell parameter of the tube compared to the rod indicates a difference in oxygen content of the Bi-2212 phase. Some authors observed a c decrease with an increase in δ [95, 139, 140]. This phenomenon is explained by a contraction of the two BiO layers with oxygen incorporation in the structure. The $\mathrm{Bi^{3+}}$ cations with the electronic configuration $5d^{10}6s^2$ exhibit a lone pair located between both BiO layers [58]. Oxygen uptake leads to a variation of lone pair orientations accompanied by a contraction of the BiO layers and a c decrease. Consequently our rod sample with a larger oxygen content shows a relatively smaller c unit-cell parameter. The larger oxygen content in the rod is in agreement with the lower critical temperature (82 K for the rod, 91 K for the tube, see later).

Figures 6.2 and 6.4 show pole figures for the main Bi-2212 crystallographic directions, respectively for the tube and the rod. Note that tube and rod pole figures do not have the same reference frame due to experimental considerations. Both samples exhibit weak textures characterized by maxima of orientation distribution densities not larger than few multiples of random distribution (7 m.r.d. at maximum for the {200} pole figure of the tube, and 2.7 m.r.d. at maximum for the $\{00\underline{10}\}$ pole figure for the rod). The {200} and $\{00\underline{10}\}$ pole figures of the tube (Figure 6.2) show a reinforcement of their equators, a- and c-axes are in a major way preferentially oriented in the XOZ plane of the sample. This results in a reinforcement of the center of the {020} pole figure. These texture components indicate that most of the crystallographic ab planes, containing the $\mathrm{CuO_2}$ conductive planes, are parallel to and randomly distributed around the Y-axis of the tube (Figure 6.3). Such an orientation should favor current conduction along the Y direction, and we expect to measure smaller resistivities along this latter direction. Another minor component is shown in the center of the $\{00\underline{10}\}$ pole figure of the tube, corresponding to ab-planes aligned perpendicular to Y, which will provide some conductivity along this axis. The {200} and $\{00\underline{10}\}$ pole figures of the rod (Figure 6.4) exhibit a- and c-axes preferentially aligned with the Z rod axis, and the {020} pole figure b-axes on the equator. These components result in a- and b-axes aligned with Z and radially, i.e. contributing to similar conduction paths along these directions. Consequently we expect to observe a reduced anisotropy of the resistivity between radial and longitudinal directions of the rod.

Using the two ODFs of these samples, we can now predict their macroscopic resistive behavior and compare them to measured resistivities.

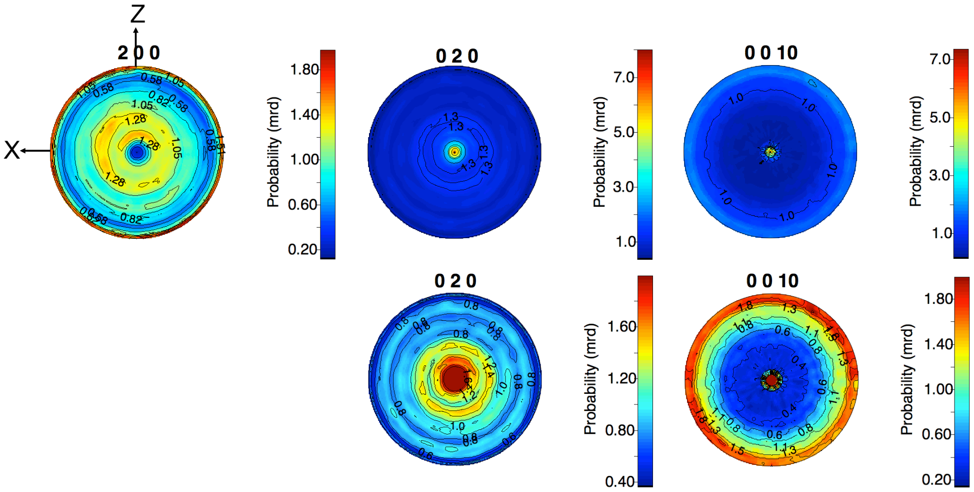

Figure 6.2 – {200}, {020}, and {00$\underline{10}$} normalized pole figures of the main crystallographic directions of Bi-2212 phase from the tube.

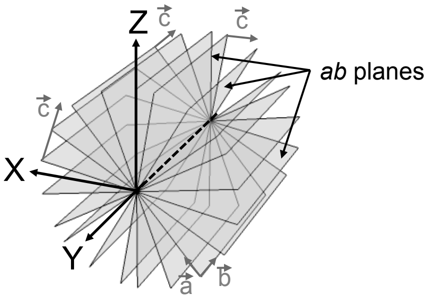

Figure 6.3 – Representation of the orientation of c-axes and CuO_2 planes in the XYZ samples reference frame for the tube.

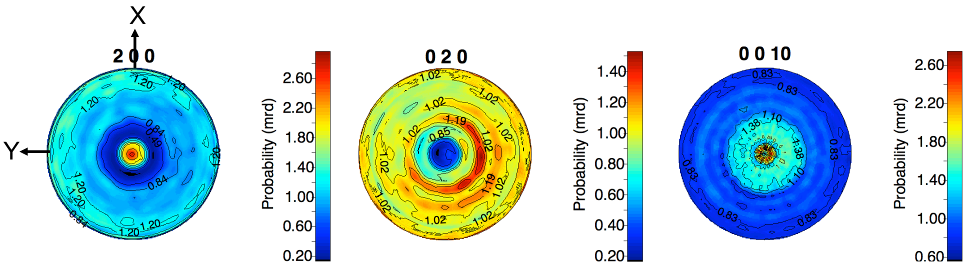

Figure 6.4 – {200}, {020}, and {00$\underline{10}$} normalized pole figures of the main crystallographic directions of Bi-2212 phase in rod.

Figure 6.5 shows the temperature dependence of the resistivity for the tube and rod specimens cut along the X, Y, and Z directions (X-, Y-, and Z-resistivities).

The metallic behavior is clearly exhibited in all samples down to the superconducting transition at $T_c = 92K$ and 82K for the tube and rod respectively. It is well known that largest T_c values are observed for an optimal oxygen content value (δ) in $Bi_2Sr_2CaCu_2O_{8+\delta}$ [18,64]. Under the same synthesis conditions, the tube exhibits a more optimized oxygenation state than the rod, this latter being in an overdoped state (δ_{tube}=0.190 and δ_{rod}=0.225). Resistivity curves along X and Z are superimposed on the entire temperature range for the tube (Figure 6.5(a)) while resistivity along Y is markedly smaller in the normal state, with an anisotropic resistivity ratio ρ^M_{ZZ}/ρ^M_{YY} around 2.3 and roughly constant from 100K to 300K (Figure 6.6). These measurements are in good agreement with texture results from which we were expecting smaller resistivity along Y and similar resistivities along X and Z, due to ab-plane alignments. We also calculated that above the superconducting transition, the anisotropic resistive ratio increases with temperature decreases.

ODF-weighted resistivities (Figure 6.7) calculated assuming homogeneous crystallites, perfect grain boundaries (GBs) and pure Bi-2212 phase, are 10 times larger than the observed ones. This result is opposite to what can be anticipated, as in our assumptions we have neglected scattering by crystal defects. It is not possible that the observed less than 20% second phases (if even excellently conducting, which is not the case) can provide an order of magnitude drop in resistivity. We speculate that the inconsistency between the measured and calculated resistivities may imply that the *c*-axis current plays only a minor role in the overall current flow, which is predominantly within the well conducting *ab* planes though the overall path could be longer. This can be related to the special structure of high-angle grain boundaries in Bi2212 [142]. Further work is needed to say how relevant are these considerations. The calculated normal state macroscopic resistivity ratios $\rho^{M,ODF}_{ZZ}/\rho^{M,ODF}_{YY}$ are 3.5-5 (depending on temperature), which compares relatively well to the measured ratio of 2.3 indicating that 80% of the resistive anisotropy is due to textural effects. Within the model of current flow only within the *ab* planes, the effect of texture on resistivity consists in controlling the length of conduction path.

Since resistivity can vary with oxygen content and single crystal data are available for different values of oxygen content, the $\rho^{M,ODF}_{XX}$, $\rho^{M,ODF}_{YY}$, and $\rho^{M,ODF}_{ZZ}$ values were calculated in the range 100K-300K for oxygen content in the range 8.214 to 8.220. It resulted that, for a given direction, simulated macroscopic values increase for lower oxygen contents and larger temperatures whatever the oxygen content. More importantly, for a given normal-state temperature, $\rho^{M,ODF}_{ZZ}/\rho^{M,ODF}_{YY}$ is not significantly modified whatever the single crystal resistive data for this oxygen content range.

Proceeding identically with the rod sample a similar metallic behavior is observed along the Y and Z directions. However, due to the lower texture strength and the presence of more texture components in this sample, Y- and Z-resistivities measured in the rod are exhibiting much less anisotropy than in the tube specimen, with a ρ^M_{ZZ}/ρ^M_{YY} ratio of 1.11 only at 300K. This anisotropy ratio is also roughly constant in the probed normal-state temperature range. Normal state ODF-weighted macroscopic resistivities are still larger than effective measured values (for the same reasons), but the deviation of $\rho^{M,ODF}_{ZZ}/\rho^{M,ODF}_{YY}$ is half the one for the tube sample. This again points for the influence of grain boundaries effects (neglected in the calculations), which have been averaged out for the weaker texture strength of the rod.

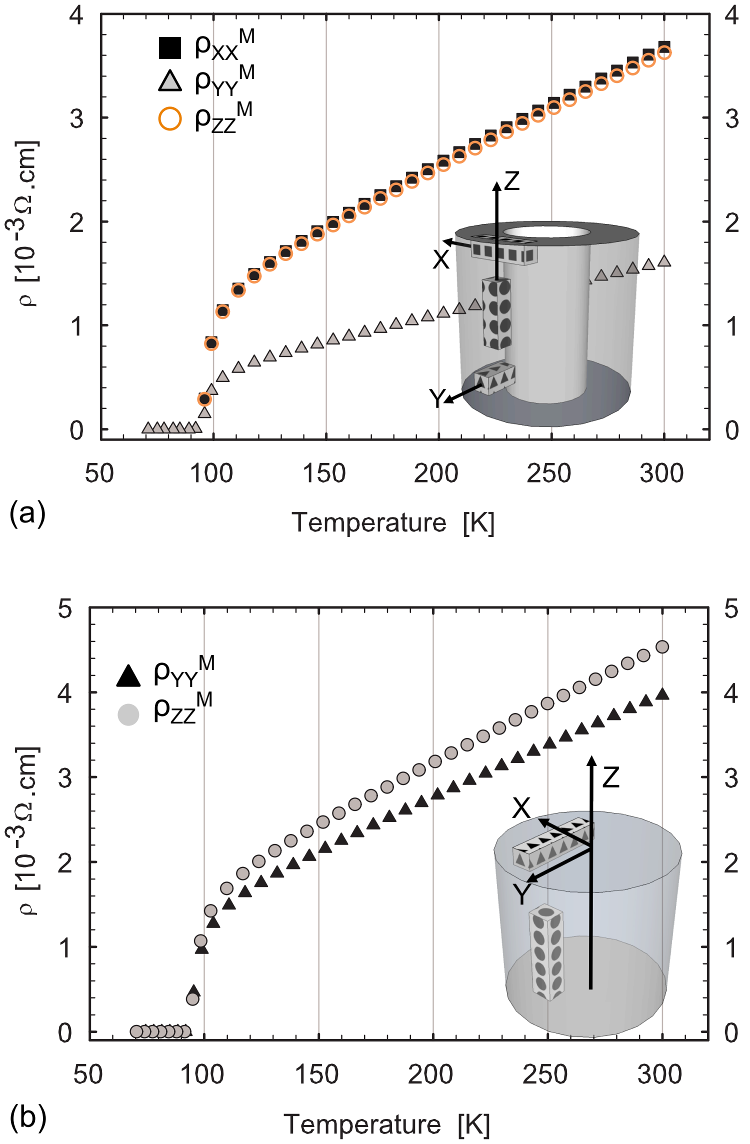

Figure 6.5 – Temperature dependence of resistivity measured on bars cut from (a) tube and (b) rod from 70K to 300K. Insets represent bar orientations in raw materials.

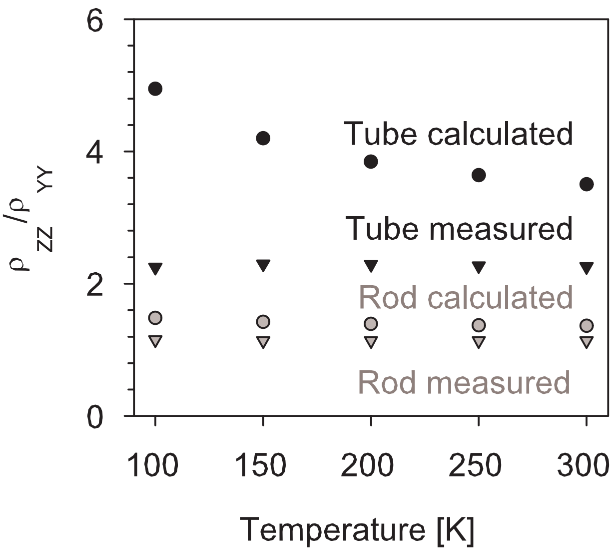

Figure 6.6 – Macroscopic resistivities ratio for the tube and the rod at different temperatures.

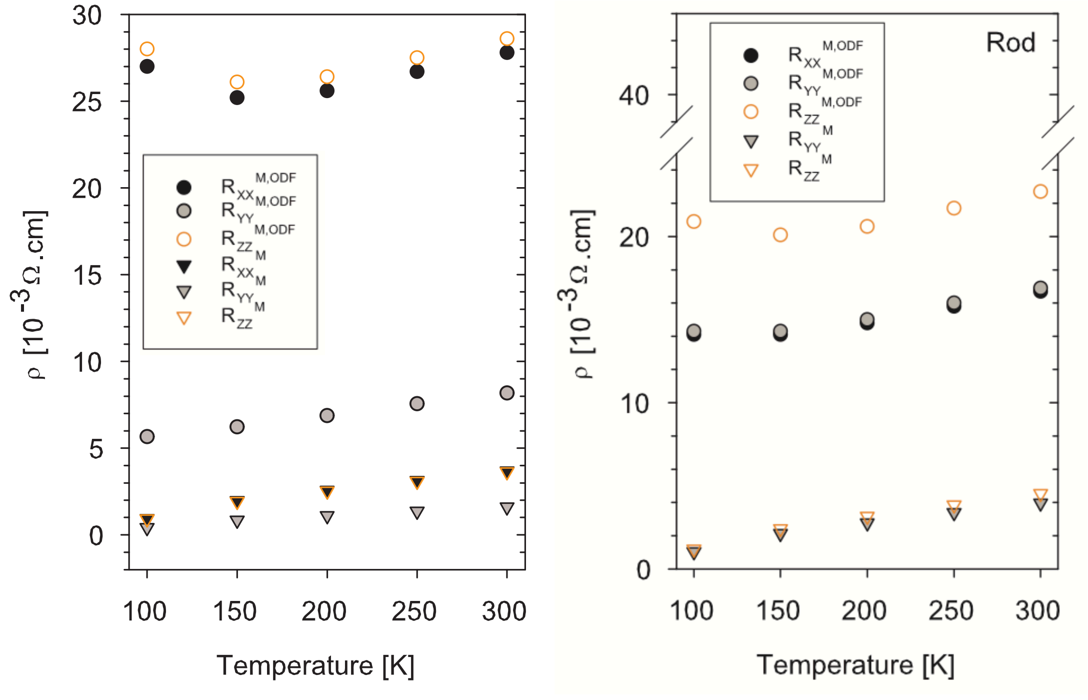

Figure 6.7 – Macroscopic resistivities calculated in X, Y and Z directions, and measured resistivities for tube and rod samples at different temperatures for single crystal oxygen content 8+0.22.

These two case samples help appreciating the effect of crystallographic orientation strengths on the resulting conductive properties of the Bi-2212 phase. In strongly oriented samples, even a weak intrinsic, single crystal resistivity anisotropy, is able to provide the sample usable properties in some given directions. However in such melt-cast processed samples the orientation densities cannot be larger than typically 10 m.r.d.. Hopefully, Bi-2212 exhibits intrinsically anisotropies as large as 10^4, which compensate for the low texture strength, even close to randomly oriented samples (which would exhibit orientation densities of 1 m.r.d.). In order to better estimate this combination between texture strength and tensor anisotropy, we have simulated a single <001>-fiber texture component for the Bi-2212 phase, i.e. with *c*-axes aligned along Z, using a Gaussian distribution component in the orientation space. The corresponding $\{00\underline{10}\}$ pole figures for increasing full widths of the Gaussian (Figure 6.8) display a strong decrease of the maximum orientation density from 350 m.r.d. to 1.35 m.r.d. For each texture simulation, we calculated the resulting resistivity tensor calculation. Figure 6.8 illustrates the decrease in anisotropic resistivity ratio with temperature and Gaussian's FWHM. The large single crystal anisotropic ratio (10^4-10^5) decreases by a factor of 10 with only a 10° of dispersion. Larger dispersions up to 140° reduce this anisotropic ratio to 2, close to values observed in the tube and rod samples. However, for smaller texture strengths, the anisotropy decrease is less sensitive to the FWHM, since at low orientation levels, further randomization of conducting planes does not modify significantly carrier paths. Consequently, thanks to very high resistive anisotropy of Bi-2212 single crystals, melt-cast bulks are still exhibiting comparatively strong anisotropies of their resistivity, favorable to good current transport in the normal state.

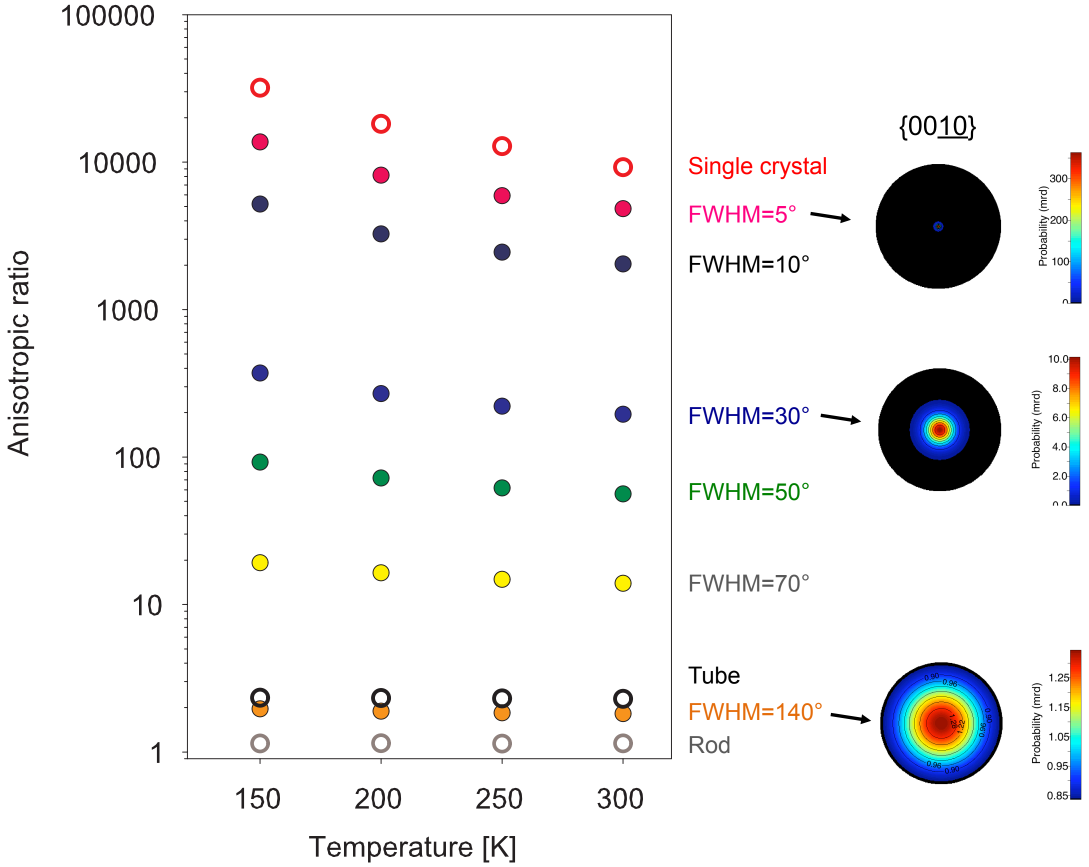

Figure 6.8 – Temperature dependence of the anisotropic resistivity ratio of the Bi-2212 phase for simulated fiber textures with varying Gaussian full-widths and their comparison to melt-cast samples.

6.4 Conclusion

We studied the correlation between crystallographic orientation strength and macroscopic anisotropic resistivity ratio in Bi-2212 melt-casted bulk materials with various textures. Quantitative texture analysis provides the way for the calculation of ODF-weighted tensor homogenization using the geometric mean approach from single crystal resistivity data. We showed that small anisotropy ratio in melt-cast Bi-2212 bulks are the consequence of the weak textures achieved in such compounds, with maxima of orientation distributions not higher than 10 m.r.d.. Calculated anisotropic resistivity ratio and measured values compare well. Larger texture strengths would benefit more optimized properties, but the very large single crystal anisotropy partly compensates the low texture strengths and results in melt-cast samples with reasonably good conductive paths compared to other Bi-2212 bulk elaboration ways.

General conclusion and perspectives

Conclusion sections have been included in Chapters 3 to 6 and the experimental results are summarized there. In this general conclusion, we want to provide an overview of our most important results in the context of both previous and future work.

This thesis was part of the international program IDS FunMAT and results from a collaboration between University of Caen, University of Liege and Nexans SuperConductors Gmbh. The superconducting Bi-2212 bulk samples manufactured at Nexans Superconductors are known to achieve excellent performances despite a synthesis process which does not result in strongly textured materials: tubes and rods reach self-field current densities J_c ~ 1-2 kA/cm^2 at 77 K (~100 kA/cm^2 at 5 K). Although these J_c values are three orders of magnitude smaller than in coated conductors, the engineering current densities are only a factor of 5 to 10 smaller.

Investigating these bulk samples is not an easy task because the melt-cast processing procedure results in the presence of several second phases with a range of inclusion sizes (up to 100μm), the probable existence of Bi-2201 intergrowths in the Bi-2212 phase, a significant porosity in some parts of the samples,etc. Besides, the temperature gradient during cooling means that the oxygenation, microstructure and texture of the final material are expected to vary across the sample thickness. Over the years, researchers at Nexans Superconductors have gathered a lot of knowledge about the properties of these Bi-2212 bulk materials. However, a full characterization of texture had never been done since texture had always been studied using a preferred orientation index deduced from a single X-ray diffraction pattern with the March-Dollase approach. It was therefore decided that the first aim of this thesis should be to carry out a complete characterization of the texture to confirm the preferential orientation studies made at Nexans.

During this thesis, quantitative texture analysis of Bi-2212 bulks has been performed at different scales, using X-ray diffraction to probe surface layers and neutron diffraction to probe the bulk volume of the samples. The principal samples investigated in the thesis were a tube with outer/inner diameter of 50/35mm and a few rods with 8mm diameter. The X-ray diffraction data were collected with a dedicated X-ray texture diffractometer at CRISMAT (Caen). The neutron diffraction data were obtained during two sessions at Institut Laue Langevin (Grenoble): the first, exploratory session of 2 days on the D19 beamline took place two months after the beginning the thesis project; we were awarded a second session to characterize a small selection of samples on the D1B beamline at the beginning of the second year of the thesis (before the long shut-down of ILL in 2013-2014). In both cases, we had to find a compromise between the acquisition time (and signal to noise ratio) and the number of samples we could characterize during the allocated beamtime.

The texture experiments prove that all samples are weakly textured with maxima below 10 m.r.d. whatever the instrument employed. The main component of texture in the tube and rods are compatible with the ones proposed by M.O. Rikel at Nexans Superconductors, with *ab*-planes parallel to the radial direction. Nevertheless, we were able to evidence other minor texture components, such as a <001>-fiber texture in the tube that seems to occur mainly close to the outer and inner surfaces of the tube instead of at the center of the tube wall. Generally speaking, some differences in texture between X-ray and neutron experiments suggest that local texture differs from macroscopic texture. We conclude that the preferred orientation index determined at Nexans Superconductors using single $\theta-2\theta$ patterns gives only a partial view of the texture but, fortunately, the main texture components in the tube and rods correspond to favourable cases where it can be detected by this approach. This is obviously good news since neither the X-ray texture diffractometer (due to limitations in (χ, φ) range as a consequence of defocussing) nor the neutron beamlines (due to beamtime allocation limitations) qualify as a routine characterization method. However, verification by full texture characterization would be essential in case of significant modifications to the synthesis procedure.

As explained above, the texture results reported in the thesis provide the answer to the question that was at the origin of the project. However, if future work is engaged into along these lines, it might be worth trying to further improve the quality of the structural model used for the Rietveld refinements during the full texture analysis. It should be stressed beforehand that attempting to solve the issues discussed hereafter would represent a very considerable work, very likely resulting in comparatively minor modifications of the conclusions. The initial structural model used during this thesis was built from structural data available in crystallographic databases; this means that the cationic ratios do not fit exactly with the experimental ones (which might even vary inside the probed volume of the sample). Besides, not all second phases could be identified and/or included in the refinements (in some cases due to limits in computing capabilities). Another point is the possible presence of Bi-2201 intergrowths, which we could not detect but are known to cause broadening of the diffracting reflections. The occurrence of modulations in the Bi-2212 phase was considered at the beginning of the thesis but no evidence was found from the available diffraction data. Considering the coexistence of several phases, the resolution and the signal-to-noise ratio of the experimental data, refining parameters such as cationic occupations is not a valid possibility and would result in widely unreliable refined parameters. Information would need to be obtained from other sources, such as high resolution EDX mapping. However, due to the inhomogeneity and various gradients in the samples, the microscopic characterizations would need to be performed on extended zones from different parts of the samples.

Having demonstrated that the Bi-2212 melt-cast processed samples are textured, even if texture strength is weak, it was logical to investigate how the physical properties might be affected by texture. Resistivity and magnetization as a function of temperature were measured along the three main directions of the tube. Magnetization is not much affected by the direction of measurement, contrary to the normal state electrical resistivity which displays a ratio of 2.3 between the resistivity along the tube axis and the resistivity along the radial direction. These observations are qualitatively consistent with the texture results and a quantitative study based on the geometric mean approach of the anisotropic resistivity tensor was carried out to compare the experimental data with values calculated from the measured orientation function combined with literature single crystal data. It turns out that, despite the weak texture, a large fraction of the observed resistivity anisotropy in the tube is explained by texture effects, because of the very strong anisotropy between the resistivity along the *c*-axis and the resistivity in the *ab* planes. However, the fact that the measured resistivities are lower than the calculated ones suggests that one or several of the necessary assumptions adopted for the calculation (Bi-2212 pure phase, no seconds phases, perfect grain boundaries) are not fulfilled; since one of these assumptions is that of perfect grain boundaries, this points to possible effects linked to conduction mechanisms at grain boundaries. Again, extensive microscopic investigations are clearly called for but our attempts to study texture and orientation relationships at the microscopic scale by Electron Back-Scattering Diffraction (EBSD) were impeded by our inability to obtain adequately polished samples, although other groups seem to have been more successful.

Another point investigated in this thesis concerns the inhomogeneity that exists across the tube wall or rod radius due to the temperature gradient during the cooling of the samples. This inhomogeneity was detected in the texture results, with different minor texture components in the outer, center and inner samples cut at different depths in the tube wall. The difference in resistivities (measured along the direction parallel to the tube axis) were smaller than the ones observed between the measurements along different tube directions. In order to obtain a more precise view of the evolution of texture across the tube wall, we submitted a proposal to ESRF to determine the texture profile by collecting data every 250 μm with the ID15A beamline. The proposal was not selected but could be resubmitted in the future.

Texture is not the only parameter that can influence the physical properties of the superconducting samples. Another important parameter is the oxygen content and it seemed important to study samples with similar texture but different oxygen content. The control of the oxygenation process was indeed one of the ongoing projects at Nexans Superconductors R&D center at the time this thesis started. They succeeded in producing optimal 5mm diameter rod samples with a wide range of oxygen content during the last year of this thesis. Due to the long closure of ILL and the delay involved in the proposal system, the texture of these samples was not characterized with neutrons, but the resistivity vs. temperature and magnetization vs. magnetic field were collected for a series of 13 samples. The dependence of T_c as a function of oxygen content follows a bell-shaped curve, confirming literature results for other superconducting samples. The critical current density is also influenced by the oxygen content; interestingly, the maximum J_c is not obtained for the same oxygen content as the maximum T_c.

At the end of this 3-year project, the original basic questions regarding the full texture vs. March-Dollase controversy have been answered but the topic of texture at different scales is obviously far from exhausted. The next priority should probably be set on studies at a more microscopic level, whose results might allow to go deeper in the analysis of the results in this thesis, and guide further investigations within a truly "Combined Analysis" approach.

Annexe 1 | COD-2212

COD data 1000285

chemical name systematic	Dibismuth distrontium calcium dicopper oxide
chemical formula structural	'Bi2 Sr2 Ca Cu2 O8'
chemical formula sum	'Bi2 Ca Cu2 O8 Sr2'
publ section title	Electron microscopy study of the superconductor "$\mathrm{Bi_2\ Sr_2\ Ca\ Cu_2\ O_8}$"
publ author name	Hervieu, M, Michel, C, Domenges, B, Laligant, Y, Lebail, A, Ferey, G, Raveau, B
journal name full	'Modern Physics Letters B'
journal coden ASTM	MPLBET
journal volume	2
journal year	1988
journal page first	491
journal page last	500
cell length a	5.4054
cell length b	5.4016
cell length c	30.7152
cell angle alpha	90
cell angle beta	90
cell angle gamma	90
cell volume	896.8
cell formula units Z	4
symmetry space group name H-M	'A m a a'
symmetry Int Tables number	66
symmetry cell setting	orthorhombic

symmetry equiv pos as x,y,z 'x,y,z'
'x,-y,-z'
'1/2-x,y,-z'
'1/2-x,-y,z'
'-x,-y,-z'
'-x,y,z'
'1/2+x,-y,z'
'1/2+x,y,-z'
'x,1/2+y,1/2+z'
'x,1/2-y,1/2-z'
'1/2-x,1/2+y,1/2-z'
'1/2-x,1/2-y,1/2+z'
'-x,1/2-y,1/2-z'
'-x,1/2+y,1/2+z'
'1/2+x,1/2-y,1/2+z'
'1/2+x,1/2+y,1/2-z'

atom type symbol	atom type oxidation number
Bi3+	3.000
Sr2+	2.000
Cu2+	2.000
Ca2+	2.000
O2-	-2.000

site label	site type symbol	site multiplicity	Wyckoff symbol	site fract x	site fract y	site fract z	site occupancy
Bi1	Bi3+	16	m	0.052(3)	0.2745(7)	0.0524(2)	0.5
Sr1	Sr2+	8	l	0	0.75	0.3597(4)	1
Cu1	Cu2+	8	l	0.5	0.75	0.3033(6)	1
Ca1	Ca2+	4	f	0.5	0.25	0.25	1
O1	O2-	8	h	0.75	0	0.201(5)	1
O2	O2-	8	h	0.25	0.5	0.201(5)	1
O3	O2-	8	l	0	0.25	0.385(2)	1
O4	O2-	8	l	0.5	0.27	0.0524	1

atom site label	U 11	U 12	U 13	U 22	U 23	U 33
Bi1	0.054	0	0	0.008	0	0.033
Sr1	0.095	0	0	0.01	0	0.068
Cu1	0	0	0	0	0	0.096
Ca1	0.099	0	0	0.03	0	0.158

Annexe 2 | List of Bi-2212 reflections

h	k	l	d	2θ position (λ_{Cu}=1.5406Å)	2θ position (λ_{D1B}=2.5249Å)	2θ position (λ_{D19}=1.4510Å)
0	0	2	15.36	5.75	9.43	5.41
0	0	4	7.68	11.51	18.92	10.84
0	1	1	5.32	16.64	27.44	15.67
0	0	6	5.12	17.30	28.54	16.29
0	1	3	4.78	18.55	30.63	17.46
0	1	5	4.06	21.88	36.25	20.60
0	0	8	3.84	23.14	38.38	21.78
1	1	1	3.79	23.43	38.88	22.05
1	1	3	3.58	24.84	41.28	23.38
0	1	7	3.41	26.13	43.50	24.59
1	1	5	3.24	27.46	45.78	25.83
0	0	10	3.07	29.04	48.52	27.31
0	1	9	2.89	30.96	51.88	29.12
1	1	7	2.88	31.00	51.95	29.15
2	0	0	2.70	33.11	55.67	31.13
0	2	0	2.70	33.13	55.71	31.15
2	0	2	2.66	33.63	56.60	31.62
0	2	2	2.66	33.65	56.64	31.64
0	0	12	2.56	35.01	59.08	32.92
2	0	4	2.55	35.16	59.34	33.05
0	2	4	2.55	35.18	59.38	33.08
1	1	9	2.55	35.22	59.45	33.11
0	1	11	2.48	36.17	61.16	34.00

h	k	l	d	2θ position (λ_{Cu}=1.5406Å)	2θ position (λ_{D1B}=2.5249Å)	2θ position (λ_{D19}=1.4510Å)
2	1	1	2.41	37.27	63.17	35.03
2	0	6	2.39	37.59	63.74	35.33
0	2	6	2.39	37.61	63.78	35.35
1	2	2	2.39	37.64	63.84	35.38
2	1	3	2.35	38.21	64.89	35.91
1	2	4	2.30	39.04	66.40	36.68
1	1	11	2.25	39.94	68.08	37.53
2	1	5	2.25	40.04	68.26	37.62
2	0	8	2.21	40.78	69.64	38.31
0	2	8	2.21	40.80	69.68	38.33
0	0	14	2.19	41.09	70.23	38.61
1	2	6	2.18	41.27	70.56	38.77
0	1	13	2.16	41.67	71.32	39.15
2	1	7	2.12	42.66	73.18	40.07
1	2	8	2.04	44.24	76.22	41.55
2	0	10	2.03	44.60	76.92	41.88
0	2	10	2.03	44.62	76.95	41.90
1	1	13	2.01	45.06	77.80	42.31
2	1	9	1.97	45.96	79.55	43.14
0	0	16	1.92	47.29	82.20	44.39
0	1	15	1.91	47.43	82.46	44.51
2	2	0	1.91	47.54	82.69	44.62
1	2	10	1.90	47.84	83.30	44.90
2	2	2	1.90	47.93	83.47	44.98
2	0	12	1.86	48.95	85.54	45.94
0	2	12	1.86	48.97	85.57	45.95
2	2	4	1.85	49.08	85.80	46.06
2	1	11	1.83	49.84	87.35	46.76

Table 6.1 – List of some Bi-2212 reflections and their 2θ angular positions for the Cu, D1B, and D19 wavelengths

Bibliographie

[1] H. Kamerlingh Onnes. Further experiments with liquid helium. In *KNAW, Proceedings*, volume 13, pages 1910–1911, 1911.

[2] J. G. Bednorz and K. A. Müller. Possible High T_c superconductivity in the Ba-La-Cu-O system. *Zeitschrift für Physik B Condensed Matter*, 64(2) :189–193, 1986.

[3] M. K. Wu, J. R. Ashburn, C. J. Torng, P. H. Hor, R. L. Meng, L. Gao, Z. J. Huang, Y. Q. Wang, and C. W. Chu. Superconductivity at 93 k in a new mixed-phase Y-Ba-Cu-O compound system at ambient pressure. *Physical Review Letters*, 58(9) :908–910, 1987.

[4] H. Maeda, Y. Tanaka, M. Fukutomi, and T. Asano. A new high-T_c oxide superconductor without a rare earth element. *Japanese Journal of Applied Physics*, 27(Part 2, No. 2) :L209–L210, 1988.

[5] J. M. Tarascon, W. R. McKinnon, P. Barboux, D. M. Hwang, B. G. Bagley, L. H. Greene, G. W. Hull, Y. LePage, N. Stoffel, and M. Giroud. Preparation, structure, and properties of the superconducting compound series $Bi_2Sr_2Ca_{n-1}Cu_nO_y$ with n=1,2, and 3. *Physical Review B*, 38(13) :8885–8892, 1988.

[6] A. Schilling, M. Cantoni, J. D. Guo, and H. R. Ott. Superconductivity above 130 K in the Hg–Ba–Ca–Cu–O system. *Nature*, 363(6424) :5658, 1993.

[7] Y. Kamihara, T. Watanabe, M. Hirano, and H. Hosono. Iron-based layered superconductor $La[O_{1-x}F_x]FeAs$ (x=0.05-0.12) with T_c=26K. *Journal of the American Chemical Society*, 130(11) :3296–3297, 2008.

[8] J. Nagamatsu, N. Nakagawa, T. Muranaka, and J. Zenitani, Y.and Akimitsu. Superconductivity at 39K in magnesium diboride. *Nature*, 410(6824) :63–64, 2001.

[9] A. F. Hebard, M. J. Rosseinsky, R. C. Haddon, D. W. Murphy, S. H. Glarum, T. T. M. Palstra, A. P. Ramirez, and A. R. Kortan. Superconductivity at 18 K in potassium-doped C60. *Nature*, 350(6319) :600–601, 1991.

[10] I. A. Parinov. Superconductors and superconductivity : General issues. In *Microstructure and Properties of High-Temperature Superconductors*, pages 1–72. Springer Berlin Heidelberg, 2012.

[11] W. Meissner and R. Ochsenfeld. Ein neuer effekt bei eintritt der supraleitfähigkeit. *Naturwissenschaften*, 21(44) :787–788, 1933.

[12] J. N. Rjabinin and L. V. Shubnikov. *Phys. Z. Sowjetunion*, 7 :122, 1935.

[13] A.A. Abrikosov. On the magnetic properties of superconductors of the second group. *Sov. Phys. JETP*, 5(6) :1174, 1957.

[14] F. London and H. London. The electromagnetic equations of the supraconductor. *Proceedings of the Royal Society A : Mathematical, Physical and Engineering Sciences*, 149(866) :71–88, 1935.

[15] A. B. Pippard. An experimental and theoretical study of the relation between magnetic field and current in a superconductor. *Proceedings of the Royal Society of London. Series A. Mathematical and Physical Sciences*, 216(1127) :547–568, 1953.

[16] A. K. Saxena. *High-Temperature Superconductors*, volume 125 of *Springer Series in Materials Science.* Springer, 2009.

[17] Y. Brunet. *Supraconducteurs.* Ed. Techniques Ingénieur, 1992.

[18] P. Majewski. Materials aspects of the high-temperature superconductors in the system Bi_2O_3–SrO–CaO–CuO. *J. Mater. Res.*, 15(04) :854–870, 2000.

[19] H. Zhang and H. Sato. Structural stability of bi-based cuprates. *Physica C : Superconductivity*, 214(3-4) :265–271, 1993.

[20] C. Michel, M. Hervieu, MM Borel, A. Grandin, F. Deslandes, J. Provost, and B. Raveau. Superconductivity in the Bi-Sr-Cu-O system. *Zeitschrift für Physik B Condensed Matter*, 68(4) :421–423, 1987.

[21] M Babaei pour, D.K Ross, P.A Gorgiev, B Khoshnevisan, and A Yazdani. Oxygen non-stoichiometry of bismuth-based $Bi_2Sr_2CaCu_2O_{8+x}$ (bi-2212) high-temperature superconductor. *Physica C : Superconductivity*, 391(3) :289–297, 2003.

[22] N. Jakubowicz, O. Pérez, D. Grebille, and H. Leligny. Bi^{3+} electronic lone pair configuration in the modulated Bi-2212 type oxides. *Journal of Solid State Chemistry*, 139(1) :194–199, 1998.

[23] H. Budin, O. Eibl, P. Pongratz, and P. Skalicky. Disorder in the BiO sublattice of $Bi_2Sr_2Ca_{n-1}Cu_nO_{2n+4+z}$ phases. *Physica C : Superconductivity*, 207(3-4) :208–224, 1993.

[24] H. G. von Schnering, L. Walz, M. Schwarz, W. Becker, M. Hartweg, T. Popp, B. Hettich, P. Müller, and G. Kämpf. *Angewandte Chemie International Edition in English*, 27(4) :574–576, 1988.

[25] D. Shi, M. Tang, K. Vandervoort, and H. Claus. Formation of the 110-K superconducting phase via the amorphous state in the Bi-Sr-Ca-Cu-O system. *Physical Review B*, 39(13) :9091–9098, 1989.

[26] E. Takayama-Muromachi, Y. Uchida, Y. Matsui, M. Onoda, and K. Kato. On the 110 K superconductor in the Bi-Ca-Sr-Cu-O system. *Japanese Journal of Applied Physics*, 27(4A) :L556, 1988.

[27] Y. Matsui, H. Maeda, Y. Tanaka, and S. Horiuchi. High-resolution electron microscopy of modulated structure in the new High-T_c superconductors of the Bi-Sr-Ca-Cu-O system. *Japanese Journal of Applied Physics*, 27(3A) :L361, 1988.

[28] S. H. Pan, E. W. Hudson, J. Ma, and J. C. Davis. Imaging and identification of atomic planes of cleaved $Bi_2Sr_2CaCu_2O_{8+\delta}$ by high resolution scanning tunneling microscopy. *Applied Physics Letters*, 73(1) :58–60, 1998.

[29] R. Gladyshevskii and R. Flukiger. Modulated structure of $Bi_2Sr_2CaCu_2O_{8+\delta}$, a high-$T_c$ superconductor with monoclinic symmetry. *Acta Crystallographica Section B : Structural Science*, 52(1) :38–53, 1996.

[30] A. Yamamoto, M. Onoda, E. Takayama-Muromachi, F. Izumi, T. Ishigaki, and H. Asano. Rietveld analysis of the modulated structure in the superconducting oxide $Bi_2(Sr,Ca)_3Cu_2O_{8+x}$. *Physical Review B*, 42(7) :4228, 1990.

[31] H.W. Zandbergen, W.A. Groen, F.C. Mijlhoff, G. van Tendeloo, and S. Amelinckx. Models for the modulation in $A_2B_2Ca_nCu_{1+n}O_{6+2n}$, A, B=Bi, Sr or Tl, Ba and n=0, 1, 2. *Physica C : Superconductivity*, 156(3) :325–354, 1988.

[32] Y. Gao, P. Lee, P. Coppens, M. A. Subramania, and A. W. Sleight. The incommensurate modulation of the 2212 Bi-Sr-Ca-Cu-O superconductor. *Science*, 241(4868) :954–956, 1988.

[33] V. Petricek, Y. Gao, P. Lee, and P. Coppens. X-ray analysis of the incommensurate modulation in the 2 :2 :1 :2 Bi-Sr-Ca-Cu-O superconductor including the oxygen atoms. *Physical Review B*, 42(1) :387, 1990.

[34] G. Calestani, C. Rizzoli, M.G. Francesconi, and G.D. Andreetti. The modulated structure of $Bi_2Sr_{3-x}Ca_xCu_2O_8$: A commensurate model from single crystal x-ray diffraction data. *Physica C : Superconductivity*, 161(5-6) :598–606, 1989.

[35] X. B. Kan and S. C. Moss. Four-dimensional crystallographic analysis of the incommensurate modulation in a $Bi_2Sr_2CaCu_2O_8$ single crystal. *Acta Crystallographica Section B Structural Science*, 48(2) :122–134, 1992.

[36] J. Castellan, B. Gaulin, H. Dabkowska, A. Nabialek, G. Gu, X. Liu, and Z. Islam. Two- and three-dimensional incommensurate modulation in optimally-doped $Bi_2Sr_2CaCu_2O_{8+\delta}$. *Physical Review B*, 73(17), 2006.

[37] A. Bianconi, M. Lusignoli, NL Saini, P. Bordet, \AA. Kvick, and PG Radaelli. Stripe structure of the CuO_2 plane in $Bi_2Sr_2CaCu_2O_{8+y}$ by anomalous x-ray diffraction. *Physical Review B*, 54(6) :4310, 1996.

[38] V Sedykh, V. Sh Shekhtman, I. S Smirnova, B. Sh Bagautdinov, E. V Suvorov, and A. V Dubovitskii. About specific features of the structure modulation in the Bi-ferrate compounds isostructural with $Bi_2Sr_2CaCu_2O_8$. *Physica C : Superconductivity*, 390(4) :311–320, 2003.

[39] E.A. Hewat, J.J. Capponi, and M. Marezio. A model for the superstructure of $Bi_2Sr_2CaCu_2O_{8.2}$. *Physica C : Superconductivity*, 157(3) :502–508, 1989.

[40] Y. Le Page, W. R. McKinnon, J. M. Tarascon, and P. Barboux. Origin of the incommensurate modulation of the 80-k superconductor $Bi_2Sr_2CaCu_2O_{8.21}$ derived from isostructural commensurate $Bi_{10}Sr_{15}Fe_{10}O_{46}$. *Physical Review B*, 40(10) :6810, 1989.

[41] Y. D. Mo, T. Z. Cheng, H. F. Fan, J. Q. Li, B. D. Sha, C. D. Zheng, F. H. Li, and Z. X. Zhao. Structural features of the incommensurate modulation in the Pb-doped Bi-2223 high-T_c phase revealed by direct-method electron diffraction analysis. *Superconductor Science and Technology*, 5(2) :69, 1992.

[42] N. Fukushima, H. Niu, S. Nakamura, S. Takeno, M. Hayashi, and K. Ando. Structural modulation and superconducting properties in $Bi_{2-x}Pb_xSr_2CaCu_2O_{8+d}$ and $Bi_{2-y}Pb_ySr_2YCu_2O_{8+d}$. *Physica C : Superconductivity*, 159(6) :777–783, 1989.

[43] P. Bordet, JJ Capponi, C. Chaillout, J. Chenavas, AW Hewat, EA Hewat, JL Hodeau, M. Marezio, JL Tholence, and D. Tranqui. Powder x-ray and neutron diffraction study of the superconductor $Bi_2Sr_2CaCu_2O_8$. *Physica C : Superconductivity*, 153 :623–624, 1988.

[44] P. Bordet, J. J. Capponi, C. Chaillout, J. Chenavas, B. Giordanengo, M. Godinho, A. W. Hewat, E. A. Hewat, J. L. Hodeau, P. Lejay, M. Marezio, P. De Rango, A. M. Spieser, A. Sulpice, J. L. Tholence, R. Tournier, and D. Tranqui. New superconducting oxides in the Bi-Sr-Ca-Cu-O system : magnetic measurements and structural determination. *Le Journal de Physique Colloques*, 49(C8) :C8–2111–C8–2112, 1988.

[45] M. A. Subramanian, C. C. Torardi, J. C. Calabrese, J. Gopalakrishnan, K. J. Morrissey, T. R. Askew, R. B. Flippen, U. Chowdhry, and A. W. Sleight. A new high-temperature superconductor : $Bi_2Sr_{3-x}Ca_xCu_2O_{8+y}$. *Science*, 239(4843) :1015–1017, 1988.

[46] M. Hervieu, B. Domenges, C. Michel, and B. Raveau. High resolution microscopy of the high T_c superconductor $Bi_2Sr_2CaCu_2O_{8+\delta}$. *Modern Physics Letters B*, 02(06) :835–839, 1988.

[47] S. A. Sunshine, T. Siegrist, L. F. Schneemeyer, D. W. Murphy, R. J. Cava, B. Batlogg, R. B. Van Dover, R. M. Fleming, S. H. Glarum, S. Nakahara, et al. Structure and physical properties of single crystals of the 84-K superconductor $Bi_{2.2}Sr_2Ca_{0.8}Cu_2O_{8+\delta}$. *Physical Review B*, 38(1) :893, 1988.

[48] A. I. Beskrovnyi, M. Dlouhá, Z. Jirák, S. Vratislav, and E. Pollert. Neutron diffraction study of the modulated structure of $Bi_2Sr,Ca_3Cu_2O_{8+y}$. *Physica C : Superconductivity*, 166(1–2) :79–86, 1990.

[49] S. C. Bhargava, A. Sequeira, J. S. Chakrabarty, H. Rajagopal, S. K. Sinha, and S. K. Malik. Characterization of lead free 2212 phase of bismuth superconductor with T_c of 93 K. *Solid State Communications*, 83(11) :905–913, 1992.

[50] L.A. Novomlinsky, B.Zh. Narymbetov, and V.Sh. Shekhtman. X-ray diffraction studies of high-T_c $Bi_2Sr_2CaCu_2O_{8-x}$ superconductor. *Physica C : Superconductivity*, 204(3–4) :322–324, 1993.

[51] T. Watanabe, T. Fujii, and A. Matsuda. Anisotropic resistivities of precisely oxygen controlled single-crystal $Bi_2Sr_2CaCu_2O_{8+\delta}$: Systematic study on "Spin gap" effect. *Phys. Rev. Lett.*, 79(11) :2113–2116, 1997.

[52] P. Schmitt, L. Schultz, and G. Saemann-Ischenko. Electrical properties of $Bi_2Sr_2CaCu_2O_x$ thin films prepared in situ by pulsed laser deposition. *Physica C : Superconductivity*, 168(5–6) :475–478, 1990.

[53] M.O. Rikel and E.E. Hellstrom. Development of 2201 intergrowths during melt processing Bi2212/Ag conductors. *Physica C : Superconductivity*, 357-360, Part 2 :1081–1090, 2001.

[54] Th. Schweizer, R. Müller, P. Bohac, and L.J. Gauckler. Oxygen nonstoichiometry of Bi-2212 high-T_c superconductors. In *Third Euro-Ceramics*, volume 2, pages 611–616. Faenza Editrice Iberica, 1993.

[55] X. Sun, W. Wu, L. Zheng, X. Zhao, L. Shi, G. Zhou, X. Li, and Y. Zhang. Effects of oxygen doping and structural distortion on the superconductivity of single crystals. *J. Phys. : Condens. Matter*, 9(30) :6391–6399, 1997.

[56] W.A. Groen and D.M. de Leeuw. Oxygen content, lattice constants and T_c of $Bi_2Sr_2CaCu_2O_{8+x}$. *Physica C : Superconductivity*, 159(4) :417–421, 1989.

[57] R.G. Buckley, J.L. Tallon, I.W.M. Brown, M.R. Presland, N.E. Flower, P.W. Gilberd, M. Bowden, and N.B. Milestone. The influence of oxygen on the

physical properties of the superconducting series $Bi_{2.1}(Ca_xSr_{1-x})_{n+1}Cu_{n+4+\delta}$. *Physica C : Superconductivity*, 156(4) :629–634, 1988.

[58] Ajay Kumar Saxena. Superconductivity in cuprates. In *High-Temperature Superconductors*, volume 125, pages 129–162. Springer Berlin Heidelberg, Berlin, Heidelberg, 2012.

[59] J. Bock and E. Preisler. High-temperature superconductors : Materials aspects. In *High-temperature Superconductors : Materials Aspects ; Proceedings of the ICMC '90 Topical-Conference on Materials Aspects of High-Temperature Superconductors*, volume 1, page 215. DGM-Informationsges.-Verlag, 1991.

[60] P. Majewski, H. Su, and F. Aldinger. The oxygen content of the high-temperature superconducting compound $Bi_{2+x}Sr_{3-y}Ca_yCu_2O_{8+d}$ as a function of the cation concentration. *Physica C : Superconductivity*, 229(1–2) :12–16, 1994.

[61] V. F. Shamray, A. B. Mikhailova, and A. V. Mitin. Crystal structure and superconductivity of Bi-2223. *Crystallography Reports*, 54(4) :584–590, 2009.

[62] H. Hobou, S. Ishida, K. Fujita, M. Ishikado, K. Kojima, H. Eisaki, and S. Uchida. Enhancement of the superconducting critical temperature in $Bi_2Sr_2CaCu_2O_{8+\delta}$ by controlling disorder outside CuO_2 planes. *Physical Review B*, 79(6), 2009.

[63] D. R. Harshman, A. T. Fiory, and J. D. Dow. Theory of high-T_c superconductivity : transition temperature. *Journal of Physics : Condensed Matter*, 23(34) :349501, 2010.

[64] S. Yamashita, T. Kasai, T. Fujii, T. Watanabe, and A. Matsuda. Control of carrier concentration in Bi-2212. *Physica C : Superconductivity*, 470, Supplement 1(0) :S170–S172, 2010.

[65] P Majewski, Huang-Lung Su, Huang-Lung, and M Quilitz. Relationships between the chemical composition and properties of the high-temperature superconductor $Bi_{2+x}Sr_{2-y}Ca_{1+y}Cu_2O_{8+d}$. *Journal of Materials Science*, 32(19) :5137–5141, 1997.

[66] C. Autret-Lambert, B. Pignon, M. Gervais, I. Monot-Laffez, A. Ruyter, L. Ammor, F. Gervais, J.M. Bassat, and R. Decourt. Microstructural and transport properties in substituted $Bi_2Sr_2CaCu_2O_{8+\delta}$ modulated compounds. *Journal of Solid State Chemistry*, 179(6) :1698–1706, 2006.

[67] H. Deng, P. Hua, W. Wang, C. Dong, H. Chen, F. Wu, X. Wang, Y. Zhou, and G. Yuan. Influence of low temperature–low oxygen pressure post-annealing on critical current density of Bi(Pb)2223/Ag superconductors. *Physica C : Superconductivity*, 339(3) :181–194, 2000.

[68] Yu. I. Gorina, G. A. Kalyuzhnaya, M. V. Golubkov, V. V. Rodin, N. N. Sentyurina, V. A. Stepanov, and S. G. Chernook. Evolution of the structural and superconducting properties of Bi-HTSC monocrystals when stored in air. *Journal of Surface Investigation. X-ray, Synchrotron and Neutron Techniques*, 6(1) :73–78, 2012.

[69] K.T. Kim, S.H. Jang, E.C. Park, J. Joo, H. Kim, G.-W. Hong, C.-J. Kim, H.-R. Kim, and O.-B. Hyun. Fabrication and characterization of bulk BSCCO(2212)-$SrSO_4$ composites by melt casting process. *Physica C : Superconductivity*, 445–448(0) :447–450, 2006.

[70] J. Bock, S. Elschner, and P. Herrmann. Melt cast processed (MCP)-BSCCO 2212 tubes for power applications up to 10 kA. *IEEE Transactions on Applied Superconductivity*, 5(2) :1409–1412, 1995.

[71] K.T. Kim, J.H. Lim, S.H. Jang, E.C. Park, J. Joo, G.-W. Hong, C.-J. Kim, H.-R. Kim, and O.-B. Hyun. Fabrication and characterization of BSCCO-2212 tube prepared by centrifugal casting. *Physica C : Superconductivity*, 463–465(0) :460–463, 2007.

[72] S. Elschner, J. Bock, and H. Bestgen. Influence of granularity on the critical current density in melt-cast processed $Bi_2Sr_2CaCu_2O_x$. *Superconductor Science and Technology*, 6(6) :413, 1999.

[73] A Morandi. State of the art of superconducting fault current limiters and their application to the electric power system. *Physica C : Superconductivity*, 484 :242–247, 2013.

[74] J.F. Maguire and J. Yuan. Status of high temperature superconductor cable and fault current limiter projects at american superconductor. *Physica C : Superconductivity*, 469(15-20) :874–880, 2009.

[75] M. Noe, K.P. Juengst, FN Werfel, S. Elschner, J. Bock, A. Wolf, and F. Breuer. Measurements and tests of HTS bulk material in resistive fault current limiters. *Physica C : Superconductivity*, 372 :1626–1630, 2002.

[76] W. Paul, M. Chen, M. Lakner, J. Rhyner, D. Braun, and W. Lanz. Fault current limiter based on high temperature superconductors – different concepts, test results, simulations, applications. *Physica C : Superconductivity*, 354(1-4) :27–33, 2001.

[77] M. Noe and M. Steurer. High-temperature superconductor fault current limiters : concepts, applications, and development status. *Superconductor Science and Technology*, 20 :R15, 2007.

[78] Mario Birkholz. *Thin Film Analysis by X-Ray Scattering.* Wiley VCH, Weinheim, 2005.

[79] V. V. Chernyshev. Structure determination from powder diffraction. *Russian Chemical Bulletin*, 50(12) :2273–2292, 2001.

[80] N. Popa. Texture in rietveld refinement. *Journal of Applied Crystallography*, 25(5) :611–616, 1992.

[81] R. B. Von Dreele. Quantitative texture analysis by rietveld refinement. *Journal of Applied Crystallography*, 30(4) :517–525, 1997.

[82] Y. D Wang, L. Zuo, Z. D Liang, C. Laruelle, A. Vadon, and J. J Heizmann. Quantitative texture analysis from x-ray diffraction spectra. *Journal of Applied Crystallography*, 30(4) :443–448, 1997.

[83] Olaf Engler and V. Randle. *Introduction to Texture Analysis : Macrotexture, Microtexture and Orientation Mapping.* CRC Press, 2000.

[84] L. Lutterotti, D. Chateigner, S. Ferrari, and J. Ricote. Texture, residual stress and structural analysis of thin films using a combined x-ray analysis. *Thin Solid Films*, 450(1) :34–41, 2004.

[85] H-R Wenk and P Van Houtte. Texture and anisotropy. *Reports on Progress in Physics*, 67(8) :1367–1428, 2004.

[86] J. V. Bernier, M. P. Miller, and D. E. Boyce. A novel optimization-based pole-figure inversion method : comparison with WIMV and maximum entropy methods. *Journal of applied crystallography*, 39(5) :697–713, 2006.

[87] G. Will. *Powder diffraction : the Rietveld method and the two-stage method to determine and refine crystal structures from powder diffraction data.* Springer Verlag, 2006.

[88] Luca Lutterotti. Total pattern fitting for the combined size–strain–stress–texture determination in thin film diffraction. *Nuclear Instruments and Methods in Physics Research Section B : Beam Interactions with Materials and Atoms*, 268(3–4) :334–340, 2010.

[89] Daniel Chateigner. *Combined Analysis.* Wiley-ISTE, June 2010.

[90] http ://www.ccp14.ac.uk/tutorial/lmgp/scatfac.htm.

[91] http ://www.ill.eu/en/.

[92] http ://www.frm2.tum.de/en/index.html, July 2013.

[93] http ://neutrons.ornl.gov.

[94] http ://www.psi.ch/sinq/sinq.

[95] H. J. Bunge, H. R. Wenk, and J. Pannetier. Neutron diffraction texture analysis using a 2θ-position sensitive detector. *Textures and Microstructures*, 5(3) :153–170, 1982.

[96] H. M. Rietveld. A profile refinement method for nuclear and magnetic structures. *Journal of Applied Crystallography*, 2(2) :65–71, 1969.

[97] Kenneth D. M. Harris and Maryjane Tremayne. Crystal structure determination from powder diffraction data. *Chemistry of Materials*, 8(11) :2554–2570, 1996.

[98] L. B. McCusker, R. B. Von Dreele, D. E. Cox, D. Louer, and P. Scardi. Rietveld refinement guidelines. *J. Appl. Cryst.*, 32(1) :36–50, 1999.

[99] R Young. *The Rietveld Method.* Oxford University Press, 1995.

[100] Christopher J. Gilmore, Gordon Barr, and Jonathan Paisley. High-throughput powder diffraction. I. A new approach to qualitative and quantitative powder diffraction pattern analysis using full pattern profiles. *Journal of Applied Crystallography*, 37(2) :231–242, 2004.

[101] L. B. McCusker and Ch Baerlocher. *Structure Determination from Powder Diffraction Data.* Oxford University Press, 2006.

[102] Robert E. Dinnebier. *Powder Diffraction : Theory and Practice.* Royal Society of Chemistry, 2008.

[103] René Guinebretière. *X-ray Diffraction by Polycrystalline Materials.* Wiley-ISTE, 2010.

[104] D. Rémiens, L. Yang, F. Ponchel, J. F. Légier, D. Chateigner, G. Wang, and X. Dong. X-ray combined analysis of fiber-textured and epitaxial Ba(Sr,Ti)O_3 thin films deposited by radio frequency sputtering. *Journal of Applied Physics*, 109(11) :114106–114106, 2011.

[105] L. Cont, D. Chateigner, L. Lutterotti, J. Ricote, M. L. Calzada, and J. Mendiola. Combined X-ray texture-structure-microstructure analysis applied to ferroelectric ultrastructures : A case study on $Pb_{0.76}Ca_{0.24}TiO_3$. *Ferroelectrics*, 267(1) :323–328, 2002.

[106] E. Pantos, W. Kockelmann, L. C. Chapon, L. Lutterotti, S. L. Bennet, M. J. Tobin, J. F. W. Mosselmans, T. Pradell, N. Salvado, S. Butí, R. Garner, and A. J. N. W. Prag. Neutron and x-ray characterisation of the metallurgical properties of a 7th century BC corinthian-type bronze helmet. *Nuclear Instruments and Methods in Physics Research Section B : Beam Interactions with Materials and Atoms*, 239(1–2) :16–26, 2005.

[107] J. Pehl and H. R. Wenk. Evidence for regional dauphiné twinning in quartz from the santa rosa mylonite zone in southern california. a neutron diffraction study. *Journal of Structural Geology*, 27(10) :1741–1749, 2005.

[108] H. Amorín, D. Chateigner, J. Holc, M. Kosec, M. Algueró, and J. Ricote. Combined structural and quantitative texture analysis of morphotropic phase boundary $Pb(Mg_{1/3}Nb_{2/3})O_3$-$PbTiO_3$ ceramics. *Journal of the American Ceramic Society*, 95(9) :2965–2971, 2012.

[109] D. Kenfaui, M. Gomina, D. Chateigner, and J. G. Noudem. Mechanical properties of $Ca_3Co_4O_9$ bulk oxides intended to be used in thermoelectric generators. *Ceramics International*, 40(7, Part B) :10237–10246, 2014.

[110] G. Caglioti, A. Paoletti, and F. P. Ricci. Choice of collimators for a crystal spectrometer for neutron diffraction. *Nuclear Instruments*, 3(4) :223–228, 1958.

[111] N. C. Popa. Diffraction-line shift caused by residual stress in polycrystal for all laue groups in classical approximations. *Journal of Applied Crystallography*, 33(1) :103–107, 2000.

[112] N. C. Popa and D. Balzar. Elastic strain and stress determination by rietveld refinement : generalized treatment for textured polycrystals for all laue classes. *Journal of Applied Crystallography*, 34(2) :187–195, 2001.

[113] N. C. Popa and D. Balzar. An analytical approximation for a sizeâbroadened profile given by the lognormal and gamma distributions. *Journal of Applied Crystallography*, 35(3) :338–346, 2004.

[114] L. Lutterotti and P. Scardi. Simultaneous structure and size–strain refinement by the rietveld method. *Journal of Applied Crystallography*, 23(4) :246–252, 1990.

[115] J. Bock, M. Bludau, R. Dommerque, A. Hobl, S. Kraemer, M. O. Rikel, and S. Elschner. HTS fault current limiters-first commercial devices for distribution level grids in europe. 21(3) :1202–1205, June 2011.

[116] M.O. Rikel, D. Wesolowski, Y. Yuan, and E.E. Hellstrom. Competitiveness of porosity and phase purity in melt processed Bi2212/Ag conductors. 354(1-4) :321–326, 2001.

[117] K.T. Kim, J.H. Lim, S.H. Jang, S.H. Park, J. Joo, G.-W. Hong, C.-J. Kim, H.-R. Kim, and O.-B. Hyun. Effects of annealing time and size of BSCCO-2212 rods and tubes prepared by a casting process. *Physica C : Superconductivity*, 468(15–20) :1439–1442, 2008.

[118] B. Heeb, L.J. Gauckler, H. Heinrich, and G. Kostorz. From imperfect to perfect $Bi_2Sr_2CaCu_2O_x$ (Bi-2212) grains. *Journal of Materials Research*, 8(09) :2170–2176, 1993.

[119] D. Chateigner, P. Germi, and M. Pernet. X-ray texture analysis in films by the reflection method : Principal aspects and applications. *Materials Science Forum*, 157-162 :1379–1386, 1994.

[120] J Ian Langford and D. Louer. Powder diffraction. *Rep. Prog. Phys.*, (59) :131–234, 1996.

[121] WW Schmahl, M. Lehmann, S. Räth, M. Gerards, and R. Riddle. An improved method to determine the weight fraction of 2212 and 2201 phase impurities in BSCCO-2223 powders from x-ray powder diffraction peaks. *Superconductor Science and Technology*, 11 :1269, 1998.

[122] E. Martinez, L.A. Angurel, J.C. Diez, A. Larrea, M. Aguilo, and R. Navarro. Grain texture and bulk magnetic anisotropy correlation in polycrystalline $Bi_2Sr_2CaCu_2O_{8+\delta}$ thin rods. *Physica C : Superconductivity*, 333(1–2) :93–103, 2000.

[123] G. Triscone, J.-Y. Genoud, T. Graf, A. Junod, and J. Muller. Variation of the superconducting properties of $Bi_2Sr_2CaCu_2O_{8+\delta}$ with oxygen content. *Physica C : Superconductivity*, 176(1–3) :247–256, 1991.

[124] T. Shen, J. Jiang, A. Yamamoto, U. P. Trociewitz, J. Schwartz, E. E. Hellstrom, and D. C. Larbalestier. Development of high critical current density in multifilamentary round-wire $Bi_2Sr_2CaCu_2O_{8+\delta}$ by strong overdoping. *Applied Physics Letters*, 95(15) :152516, 2009.

[125] A. Sanchez and C. Navau. Critical-current density from magnetization loops of finite high-T_c superconductors. *Superconductor Science and Technology*, 14(7) :444–447, 2001.

[126] A. Nabiałek, M. Niewczas, H. Dabkowska, A. Dabkowski, J. P. Castellan, and B. D. Gaulin. Magnetic flux jumps in textured $Bi_2Sr_2CaCu_2O_{8+\delta}$. *Physical Review B*, 67(2) :024518, 2003.

[127] Philippe Mangin. *Supraconductivité*. EDP Sciences, Les Ulis, 2013.

[128] E Cecchetti, P.J Ferreira, and J.B Vander Sande. The influence of elevated magnetic fields on the texture formation of melt-processed bi-2212. *Physica C : Superconductivity*, 336(3-4) :192–198, 2000.

[129] H. Miao, J. C. Diez, L. A. Angurel, and G. F. de la Fuente. Precursor powder influence on melt processing of high critical current BSCCO rods. *Superconductor Science and Technology*, 13(8) :1135, 2000.

[130] S. Hayashi, K. Shibutani, I. Shigaki, R. Ogawa, Y. Kawate, V. Maret, K. Kitahama, and S. Kawai. Anisotropy of the magnetic properties in $Bi_2Sr_2CaCu_2O_x$ single crystal. *Physica C : Superconductivity*, 174(4–6) :329–334, 1991.

[131] X. H. Chen, M. Yu, K. Q. Ruan, S. Y. Li, Z. Gui, G. C. Zhang, and L. Z. Cao. Anisotropic resistivities of single-crystal $Bi_2Sr_2CaCu_2O_{8+\delta}$ with different oxygen content. *Physical Review B*, 58(21) :14219, 1998.

[132] T. Makise, S. Uchida, S. Horii, J. Shimoyama, and K. Kishio. Magnetic properties of Bi2212 single crystals with Bi :Sr :Ca :Cu = 2 :2 :1 :2. *Physica C : Superconductivity*, 460–462, Part 2 :772–773, 2007.

[133] Y. Nakayama, S. Kawai, M. Kiuchi, E. S. Otabe, T. Matsushita, J. Shimoyama, and K. Kishio. Evaluation of anisotropy of critical current density in stoichiometric Bi-2212 single crystals. *Physica C : Superconductivity*, 469(15–20) :1221–1223, 2009.

[134] T. Matsushita, K. Okamura, M. Kiuchi, E. S. Otabe, T. Yasuda, and S. Okayasu. In *AIP Conference Proceedings*, volume 711, pages 627–636. AIP Publishing, 2004.

[135] Z. Mori, T. Doi, D. Kawabata, K. Ogata, K. Takahashi, A. Matsumoto, H. Kitaguchi, and Y. Hakuraku. Growth of bi-axially textured $Bi_2Sr_2CaCu_2O_{8+\delta}$ (2212) thin films on $SrTiO_3$ substrate by sputtering method. *Physica C : Superconductivity*, 468(14) :1060–1063, 2008.

[136] D. Dimos, P. Chaudhari, J. Mannhart, and F. K. LeGoues. Orientation dependence of grain-boundary critical currents in $YBa_2Cu_3O_{7-\delta}$ bicrystals. *Physical Review Letters*, 61(2) :219–222, 1988.

[137] Woldemar Voigt. *Lehrbuch der kristallphysik (mit ausschluss der kristalloptik).* B. G. Teubner, 1928.

[138] A. Reuss. Berechnung der fließgrenze von mischkristallen auf grund der plastizitätsbedingung für einkristalle . *ZAMM - Journal of Applied Mathematics and Mechanics / Zeitschrift für Angewandte Mathematik und Mechanik*, 9(1) :49–58, 1929.

[139] S. Matthies and M. Humbert. On the principle of a geometric mean of even-rank symmetric tensors for textured polycrystals. *Journal of applied crystallography*, 28(3) :254–266, 1995.

[140] U. F. Kocks. *Texture and Anisotropy : Preferred Orientations in Polycrystals and Their Effect on Materials Properties.* Cambridge University Press, 2000.

[141] S. Gražulis, D. Chateigner, R. T. Downs, A. F. T. Yokochi, M. Quirós, L. Lutterotti, E. Manakova, J. Butkus, P. Moeck, and A. Le Bail. Crystallography open database – an open-access collection of crystal structures. *Journal of Applied Crystallography*, 42(4) :726–729, 2009.

[142] F. Kametani, P. Li, D. Abraimov, A. A. Polyanskii, A. Yamamoto, J. Jiang, E. E. Hellstrom, A. Gurevich, D. C. Larbalestier, Z. A. Ren, J. Yang, X. L. Dong, W. Lu, and Z. X. Zhao. Intergrain current flow in a randomly oriented polycrystalline $SmFeAsO_{0.85}$ oxypnictide. *Applied Physics Letters*, 95(14) :142502, 2009.